

Otto-von-Guericke-University Magdeburg  
Faculty of Electrical Engineering and Information Technology  
Chair for Catheter Technologies and Image Guided Therapies

## Master's Thesis



Characterization and Automated Alignment Detection of  
an Additively Manufactured Z-frame Marker to Process  
Signals for Robotic Control in Interventional MRI

by

Parisa Parsanejad

Supervisors:

Prof. Michael Friebe

M.Sc. Robert Odenbach

October 01, 2018

# Abstract

Magnetic resonance Imaging (MRI) is an ideal imaging modality for guiding minimally invasive procedures due to its ability to perform the non-ionizing and high quality imaging. A common approach for registration and tracking of the interventional device in the MRI-space is the use of a passive MRI frame. The Z-frame is a widely used tracking frame found in the literatures, which provides a full six-degree-of-freedom estimate of the device's pose using a 2D MR-image. Despite the unique design of this frame, it is vulnerable to the MR-image distortions (due to the lack in the fiducial characteristics and the manufacturing process) which lead to the errors in the device's pose calculation.

This thesis characterizes an additively manufactured Z-frame marker and develops a nearly real-time tracking and registration algorithm for its automated alignment detection in iMRI. The algorithm consists of several image processing stages for the segmentation and localization of the fiducial markers within the MRI coordinate system, which are implemented in the form of a Graphical User Interface (GUI) in Matlab. Each stage of the processing in the GUI has an automatic and a manual processing option, where convolutional neural network is tested for the automatic segmentation of the fiducials. Therefore, the alignment of the marker is calculated using the estimated center of the fiducial markers.

The MR-images of the marker are obtained in a nearly real-time image acquisition setup using a HD-capture device which is placed between the MR-workstation monitor and the image processing laptop. For the evaluation of the accuracy and the performance of the proposed methods, several experiments are designed and conducted in a 3T MRI-system and their results are compared with a gold-standard-CAD image test. The results of the experiments show that the registration error of the proposed method is 1.5 mm within the phantom volume.

This novel automated alignment detection of the interventional instruments can contribute to a faster handling of the MRI-guided interventions, which benefits both the patient and the clinician by reducing the time and increasing the accuracy of the procedures.

# Acknowledgments:

First and foremost, I would like to thank my thesis supervisors. Firstly, to thank Prof. Michael Friebe for providing me the opportunity to work at the “chair of Catheter Technologies and Image Guided Therapies” and for his guidance and assistance throughout this work. I am also deeply grateful to M.Sc. Robert Odenbach, for his assistance, time, kindness, and most of all, for his patience. I found the weekly meetings with him very interesting and constructive. His support and advice helped me to successfully complete my master thesis.

The most special thanks go to my beloved parents, sister and boyfriend Mohamadreza, who supported and encouraged me during the stressful moments. Their unconditional support throughout the entire period was invaluable and this is the reason for which I devote this thesis to them.

Parisa Parsanejad

Magdeburg, October, 2018

# Declaration by the candidate

I hereby declare that this thesis is my own work and effort and that it has not been submitted anywhere for any award. Where other sources of information have been used, they have been marked.

The work has not been presented in the same or a similar form to any other testing authority and has not been made public.

Magdeburg, October 01, 2018

# Content

|          |   |           |
|----------|---|-----------|
| <b>1</b> | <b>Introduction.....</b>                                | <b>1</b>  |
| 1.1      | Motivation.....   | 2         |
| 1.2      | Objectives.....   | 3         |
| <b>2</b> | <b>Literature survey.....</b>                           | <b>4</b>  |
| 2.1      | Magnetic resonance imaging (MRI) .....                  | 4         |
| 2.1.1    | Artifacts in MRI .....                                  | 5         |
| 2.1.1.1  | Chemical shift artifacts .....                          | 5         |
| 2.1.1.2  | Phase cancellation artifact .....                       | 7         |
| 2.1.1.3  | Noise .....   | 8         |
| 2.2      | Instrument tracking methods in interventional MRI ..... | 10        |
| 2.2.1    | General tracking approaches .....                       | 11        |
| 2.2.2    | Passive MRI marker tracking.....                        | 11        |
| 2.3      | Principal of the Z-frame marker .....                   | 15        |
| <b>3</b> | <b>Methodology .....</b>                                | <b>19</b> |
| 3.1      | Z-frame marker characterization .....                   | 19        |
| 3.1.1    | Z-frame physical structures .....                       | 19        |
| 3.1.1.1  | Center pointing triangles .....                         | 20        |
| 3.1.1.2  | Z-axis indication triangle.....                         | 20        |
| 3.1.1.3  | Square-shaped internal tunnel structure .....           | 21        |
| 3.1.2    | Z-frame marker spectroscopy.....                        | 24        |
| 3.1.2.1  | Determination of the resin relaxation times.....        | 24        |
| 3.1.2.2  | Experimental results .....                              | 26        |
| 3.1.2.3  | Future work .....                                       | 26        |
| 3.2      | Alignment detection algorithm .....                     | 28        |
| 3.2.1    | Data acquisition .....                                  | 30        |

|          |   |           |
|----------|---|-----------|
| 3.2.2    | Image segmentation and pre-processing .....                         | 33        |
| 3.2.2.1  | Z-frame marker cropping.....  | 33        |
| 3.2.2.2  | Automatic detection of the Z-frame using Faster R-CNN.....          | 34        |
| 3.2.2.3  | Noise removal of the MR-images .....                                | 39        |
| 3.2.2.4  | Image contrast enhancement .....                                    | 45        |
| 3.2.2.5  | Image binarization .....  | 46        |
| 3.2.2.6  | Binary image mask.....  | 47        |
| 3.2.3    | Localization and registration.....                                  | 49        |
| 3.2.3.1  | Center detection of the fiducial ellipses.....                      | 49        |
| 3.2.3.2  | Image rotation estimation using automated feature matching .....    | 50        |
| 3.2.3.3  | Image rotation using centroids coordinate system.....               | 52        |
| 3.2.3.4  | Distance calculation and calibration .....                          | 54        |
| 3.2.3.5  | Marker alignment calculation .....                                  | 56        |
| 3.2.3.6  | Angle calculation of the MR-image plane and the Z-frame marker..... | 56        |
| 3.3      | Graphical user interface implementation .....                       | 61        |
| <b>4</b> | <b>Testing and result .....</b>                                     | <b>69</b> |
| 4.1      | Z-frame marker positioning using an MR-compatible rotary frame..... | 69        |
| 4.1.1    | Rotary frame calibration inside the MRI space .....                 | 69        |
| 4.1.2    | Rotation of the Z-frame around the x-axis .....                     | 71        |
| 4.1.3    | Rotation of the Z- frame around the y-axis .....                    | 73        |
| 4.1.4    | Rotation of the Z-frame around both the x-and y-axes.....           | 74        |
| 4.2      | Phantom-targeting test.....   | 78        |
| <b>5</b> | <b>Conclusion and outlook.....</b>                                  | <b>82</b> |
| <b>6</b> | <b>Appendix .....</b>   | <b>85</b> |
| <b>7</b> | <b>References .....</b>   | <b>89</b> |

# List of figures

|  |    |
|--|----|
| FIGURE 2.1: SPECTRUM OF THE WATER AND FAT PROTONS.....   | 6  |
| FIGURE 2.2: PRECESSION OF THE FAT AND WATER PROTONS IN DIFFERENT POSITIONS .....   | 6  |
| FIGURE 2.3: CHEMICAL SHIFT ARTIFACT.....   | 7  |
| FIGURE 2.4: PHASE CANCELLATION ARTIFACT. ....  | 8  |
| FIGURE 2.5: SPIKES. THE ELECTRICAL DISCHARGE DURING THE IMAGE ACQUISITION<br>GENERATES THE SPIKES AS A BANDING PATTERN IN THE IMAGE..... | 9  |
| FIGURE 2.6: MR-IMAGES OF A LIVER BIOPSY PROCEDURE WITH THE CLINICIAN’S HAND .....  | 10 |
| FIGURE 2.7: CORONAL IMAGE OF A CATHETER FILLED WITH 4% GD-DTPA.....  | 12 |
| FIGURE 2.8: THE + FRAME. DESIGN PRINCIPLE OF THE + MARKER .....  | 13 |
| FIGURE 2.9: THE PASSIVE SPHERICAL FRAME.....   | 14 |
| FIGURE 2.10: DESIGN PRINCIPLE OF THE Z-FRAME MARKER WITH FOUR VERTICAL.....  | 15 |
| FIGURE 2.11: Z-FRAME CONCEPT WITH GD-BASED MARKER CAPSULES .....   | 16 |
| FIGURE 2.12: OVERVIEW ON POTENTIAL GEOMETRIC DEFECTS FOR FIDUCIAL MARKERS<br>USING GD-FILLED CAPSULES .....                              | 17 |
| FIGURE 3.1: A 3D CAD-VIEW OF THE Z-FRAME-MARKER STRUCTURES .....   | 19 |
| FIGURE 3.2: A CORONAL VIEW OF THE Z-FRAME .....  | 21 |
| FIGURE 3.3: THE CAD VIEW OF THE Z-FRAME MARKER WITH Z-AXIS INDICATION TRIANGLE<br>MARKER .....   | 22 |
| FIGURE 3.4: 3D-CAD VIEW OF THE SQUARE SHAPED Z-FRAME .....   | 23 |
| FIGURE 3.5: MEASURED IMAGE SLICE OF THE THREE CYLINDRICAL RESIN CONTAINERS.....  | 25 |
| FIGURE 3.6 : COMPARISON OF MEASURED AND ESTIMATED T1 AND T2 RELAXATION TIMES<br>FOR THREE DIFFERENT RESINS.....                          | 27 |

|  |    |
|--|----|
| FIGURE 3.7: THE SYSTEM CONFIGURATION AND DATA FLOW DURING TRACKING AND<br>REGISTRATION PROCEDURE. ....                                       | 28 |
| FIGURE 3.8: THE FLOWCHART OF THE TWO MAIN STAGES OF THE AUTOMATIC ALIGNMENT<br>DETECTION ALGORITHM.....                                      | 29 |
| FIGURE 3.9: SETUP CONFIGURATION OF THE IMAGE ACQUISITION PROCEDURE IN THE MRI<br>CONTROL ROOM.....   | 30 |
| FIGURE 3.10: CAPTURED-MR IMAGE (T1W IMAGE) OF THE Z-FRAME MARKER.....  | 31 |
| FIGURE 3.11: QUALITY TEST IMAGE WHICH IS CAPTURED FROM A MONITOR WITH<br>DIFFERENT METHODS .....   | 32 |
| FIGURE 3.12: CROPPING OPERATION FOR EXTRACTING THE Z-FRAME MARKER FROM THE<br>CAPTURED-IMAGE. ....   | 33 |
| FIGURE 3.13: FLOWCHART OF THE MAIN PRINCIPAL OF THE CONVOLUTIONAL NEURAL<br>NETWORK .....  | 34 |
| FIGURE 3.14: FLOWCHART OF THE FASTER-REGION CNN APPROACH.....  | 37 |
| FIGURE 3.15: PRECISION AND RECALL RATE OF THE DETECTOR.....  | 38 |
| FIGURE 3.16: THE DETECTED Z-FRAME STRUCTURES FROM AN MR-CAPTURED IMAGE. ....   | 39 |
| FIGURE 3.17: THE T1W IMAGE OF THE Z-FRAME MARKER WHICH IS ACQUIRED USING THE<br>CAPTURE DEVICE AND THE AV CONVERTER.....                     | 40 |
| FIGURE 3.18: THIS IMAGE REPRESENTS THE ORIGINAL CAPTURED-MR IMAGE (T1W) FROM<br>THE Z-FRAME MARKER WITHOUT DENOISING.....                    | 42 |
| FIGURE 3.19: THE CAPTURED-MR IMAGE (T1W) FROM THE Z-FRAME MARKER WITHOUT<br>DENOISING.....   | 45 |
| FIGURE 3.20: THE DENOISED CAPTURED-MR IMAGE.....   | 46 |
| FIGURE 3.21: THE BINARIZED IMAGE OF THE CAPTURED-MR IMAGE .....  | 47 |
| FIGURE 3.22: THE IMAGE SHOWS THE RESULT OF THE FIRST MASKING METHOD USING A<br>THRESHOLD TO WITHDRAW SMALL OBJECTS FROM THE BACKGROUND ..... | 48 |



|   |    |
|---|----|
| FIGURE 3.23: THIS IMAGE ILLUSTRATES THE BINARY IMAGE OF THE Z-FRAME MARKER AND ITS DETECTED CENTROIDS OF THE SEVEN FIDUCIAL MARKERS ..... | 49 |
| FIGURE 3.24: CAPTURED-MR IMAGE OF THE Z-FRAME MARKER.....   | 51 |
| FIGURE 3.25: UNSUCCESSFUL MATCHING MODEL OF THE POINT PAIRS IN TWO DIFFERENT CROSS-SECTIONAL IMAGES OF THE Z-FRAME .....                  | 52 |
| FIGURE 3.26: FOUR DIFFERENT POSSIBLE ROTATION OF THE Z-FRAME MARKER. EACH MODEL HAS A DIFFERENT ROTATION EQUATION. ....                   | 53 |
| FIGURE 3.27: THE COMPUTED CENTER OF THE Z-FRAME MARKER (RED START) .....  | 55 |
| FIGURE 3.28: THE THREE CORRESPONDING POINTS (P2, P4, AND P6) MAKE A PLANE.....  | 57 |
| FIGURE 3.29: THE Z-FRAME PLANE INCLUDING THE COORDINATES OF P2, P4 AND P6 COORDINATE SYSTEMS .....  | 58 |
| FIGURE 3.30: THE Z-FRAME PLANE INCLUDING P2, P4 AND P6 COORDINATE SYSTEMS IS PARALLEL TO THE MR- IMAGE PLANE. ....                        | 59 |
| FIGURE 3.31: THE PROCESSING FLOWCHART OF THE IMPLEMENTED ALGORITHM IN GUI ...   | 61 |
| FIGURE 3.32: A VIEW OF THE GUI FOR THE ALIGNMENT DETECTION PROCEDURE .....  | 62 |
| FIGURE 3.33: THE POPUPMENU FOR IMPORTING THE IMAGE TO THE WORKSTATION.....  | 63 |
| FIGURE 3.34: THE PANEL OF THE INPUT PARAMETERS.....   | 63 |
| FIGURE 3.35: THE Z-FRAME SEGMENTATION BUTTON PANEL .....  | 64 |
| FIGURE 3.36: THE IMAGE PRE-PROCESSING PANEL .....   | 65 |
| FIGURE 3.37: VISUALLIZATION OF THE THE THICKNESS OF THE BLACK AND WHITE PENS ON A CAPTURED-MR IMAGE FROM THE Z-FRAME .....                | 65 |
| FIGURE 3.38: CENTER DETECTION PANEL.....  | 66 |
| FIGURE 3.39: THE ALIGNMENT DETECTION PANEL .....  | 67 |
| FIGURE 3.40: THE ROBOTIC ROTATION ADJUSTMENT PANEL.....   | 68 |
| FIGURE 4.1: THE MR-COMPATIBLE ROTARY FRAME .....  | 70 |
| FIGURE 4.2: THE ROTARY FRAME IS FIXED ON THE PATIENT TABLE .....  | 71 |

|   |    |
|---|----|
| FIGURE 4.3: THE REGRESSION MODELS OF THE COMPUTED ROTATION ANGLES AROUND<br>THE X-AXIS.....   | 72 |
| FIGURE 4.4: THE REGRESSION MODELS OF THE COMPUTED ROTATION ANGLES AROUND<br>THE Y-AXIS IN THE MR AND THE GOLD-STANDARD CAD IMAGES.....              | 73 |
| FIGURE 4.5: THE REGRESSION MODELS OF THE COMPUTED ROTATION AROUND THE X- AND<br>Y-AXES .....  | 75 |
| FIGURE 4.6: THE REGRESSION MODELS OF THE COMPUTED ROTATION AROUND THE X- AND<br>Y-AXES WHEN THE FRAME IS ROTATED AROUND BOTH THE X- AND Y-AXES..... | 76 |
| FIGURE 4.7: THE SETUP OF THE PHANTOM TARGETING TEST IN A 3T SKYRA MRI SYSTEM ...  | 80 |
| FIGURE 4.8: 2-D IMAGE OF THE Z-FRAME MARKER .....   | 81 |
| FIGURE 4.9: THE CORONAL VIEW OF THE PHANTOM AND THE Z-FRAME .....   | 81 |

# List of tables

|   |    |
|---|----|
| TABLE 3.1: ESTIMATED MEAN $\pm$ STANDARD DEVIATION T1 AND T2 RELAXATION TIMES FOR<br>THREE DIFFERENT RESINS. .... | 26 |
| TABLE 4.1: THE CALCULATED RMSE VALUES FOR EACH EXPERIMENT.....  | 77 |

# 1 Introduction

In the past few years, the use of Magnetic Resonance Imaging (MRI) for guiding interventional or diagnostic procedures has evolved a growing interest, especially for percutaneous procedures (e.g. targeted biopsy, tumor ablation, and neurological interventions) as it offers the high soft tissue contrast and the absence of ionizing radiation. Recently, a variety of stereotactic frames and mechanical or robotic positioning devices for MRI-guided instrument placement were introduced [1, 2], for the objective to improve the accuracy and to reduce the time of the procedures. The successful implementation of such devices in MRI-guided procedures requires the precise calibration and tracking of them inside the MRI space, which is generally performed by establishing a transformation between the MRI and the device coordinate systems. This process enables mapping of the position and orientation of the surgical instruments' coordinate systems to the identified target for the device alignment [3, 4].

The most common approaches for the estimation of the transformation between the MRI and the device coordinate systems are joint encoders tracking, optical tracking, active coil tracking and passive marker tracking. In the joint encoding tracking method, the device must be fixed to the MRI scanner and be calibrated prior to each surgical procedure. This process is complex and time-consuming which makes this method clinically impractical. Moreover, optical tracking, which applies an optical tracking system for the localization of the interventional device, requires a free line-of-sight between the device and the optical camera. This technique also requires the attachment of the retroreflective spheres (or sterilizable LEDs) to the interventional device which is an expensive and time-consuming process. Active tracking provides an accurate real-time localization of the devices, but it requires the additional RF coil channels for tracking the embedded radiofrequency receive coils in the device. Furthermore, passive marker tracking involves the localization of the MR-visible markers in a known configuration arrangement. Therefore, a transformation between the MRI and the device coordinate systems can be estimated using the relation between the fiducial markers. The

main advantages in this approach are an uncomplicated calibration process of the markers within the MRI coordinate system, as well as the marker compatibility with the most MRI systems without additional instrumentations (e.g. RF coils or receiver spheres) [3, 5, 6].

These are the reasons for which passive tracking markers are advantageous techniques for localization and tracking of the interventional device in the MRI environment for the most clinical procedures. A general introduction to the calibration and tracking techniques is presented in section the 2.2.

A common passive localization frame for the instrument guidance in MRI procedures is known as Brown-Roberts-Wells frame also called Z-frame. The Z-frame marker has an ability to provide a six degree-of-freedom tracking of the interventional device pose using only a single 2D-image of the marker structures. However, any error in the localization of the fiducial markers in the MR-images leads to an unacceptable error in the targeting procedure. Therefore, the algorithm for an accurate identification of the fiducial markers should deal with the image distortion problems (e.g. MRI noise and artifacts) which are detailed in the section 2.1 [3].

## 1.1 Motivation

Currently, the Z-frame marker has been applied in several different MRI-guided procedures (e.g. prostate biopsy, brain surgery) for the registration and the alignment of the interventional devices in the MRI space [1]. However, the workflow of these approaches has several drawbacks. The most important one is the need for an MRI interface which connects the robotic control, the navigation workstation and the MRI scanner with each other. But each MRI system has a different interface, hence the defined workflow of the procedure has to be optimized separately for each different MRI system. Moreover, the proposed procedures in the navigation workstation for the image processing and registration are not a straightforward task which requires an IT specialist to overcome with the challenges during the image processing and navigation [7].

It has to be mentioned that the Z-frame markers employed in the literatures have an imperfect design concept which is based on using at least two materials: one for the solid body and another for the MR-visible fiducial liquid. This can affect the potential artifact (e.g. chemical shift artifact which emanates from the liquid material) in the MR-images which leads to an erroneous shift of the real center point of the fiducials [4, 8].

## 1.2 Objectives

This thesis presents a novel marker tracking approach to automatically visualize and track the interventional tools in the MRI coordinate system by employing an additively manufactured Z-frame marker as well as a standalone and accurate algorithm for the detection of the alignment of the marker in the MR-images.

The automated algorithm must be a straightforward application, to facilitate the segmentation and processing task for the user. For this reason a user-friendly graphical interface is designed which is presented in the section 3.3. Furthermore, a comparison study and evaluation of the different possible materials for manufacturing of the Z-frame marker is conducted, and several novel physical feature structures of the marker are introduced (section 3.1). In the sections 4, the comprehensive testing and analysis are conducted for the evaluation of the accuracy and the performance of the implemented algorithm and method.

The development of an automated approach for the instrument alignment along the interventional trajectory can contribute to a faster and more precise handling of the MRI-guided interventional process. Therefore, MRI can be the best alternative imaging method for the most image-guided interventions (e.g. ultrasound- and CT-based imaging surgeries) leading to the reduced interventional time and radiation exposure to the both patient and clinician.

## 2 Literature survey

### 2.1 Magnetic resonance imaging (MRI)

MRI is a non-invasive imaging technology that generates three dimensional anatomical and functional images of the body without the use of ionizing radiation. It is particularly useful for neurological, oncological, cardiovascular, muscular and skeletal imaging. MRI employs a powerful magnetic field that forces the hydrogen atoms in the tissue being imaged to align with its axis. The additional radiofrequency fields are then used to stimulate the protons and alter the alignment of the magnetization. When the radiofrequency fields are turned off, the protons realign with the magnetic field and release the detectable energy by the MRI scanner [9].

In order to acquire the MR-images in a desired manner such that the tissues of interest are optimally distinguishable from the background, multiple pulse sequences have to be chosen appropriately. Three general criteria are available in the MRI technique to modify the measurement parameters of a pulse sequence depending on the anatomical structure under observation, such as sufficient scan time, acceptable spatial resolution, and the adequate contrast between tissues. For example, the required imaging parameters for scanning of the brain tissues are different in comparison with the imaging setup for the bone structures. In spite of the non-ionizing radiation characteristics of the MR imaging, it generates several types of imaging artifacts which affect the accuracy of the MRI-based tracking and registration negatively [10]. The most common artifacts in MRI are investigated in the section 2.1.1.

### 2.1.1 Artifacts in MRI

In the magnetic resonance imaging, artifacts are defined as the pixels that do not truly represent the anatomy being analyzed. Commonly, the artifacts are divided into three groups based on the nature of the pixel distortion. The first group refers to the artifacts that are produced by the patient anatomy movements during the data acquisition process. The blood flow and the respiratory motion are the most common causes of the motion artifacts in MRI. The second group of the artifacts are the consequence of the suboptimal imaging parameters; hence, the source of the imaging artefacts is relatively constant during the measurement. The final group of the artifacts can be generated either from an external source (e.g. electrical noise from the patient monitoring system) or the MRI hardware system. A survey about the MRI artifacts are given in [9]. In this project only the relative artifacts to the image segmentation processing are discussed.

#### 2.1.1.1 Chemical shift artifacts

Chemical shift artifacts emanate from the 3.5 ppm resonance frequency difference between fat and water protons as it is shown in the Figure 2.1 and the Figure 2.2. One consequence of this frequency difference is the misregistration of the fat and water protons which are mapped into incorrect pixels. According to the Equation 2.1, the detected signal from a voxel is positioned in a specific location based on its frequency if all protons inside a voxel have the same resonate frequency:

$$B_i = B_0 + G_T \otimes r_i \quad (2.1)$$

In the Equation 2.1,  $B_0$  is the main magnetic field,  $B_i$  is the magnetic field at location  $r_i$  and  $G_T$  is the total gradient amplitude [9].



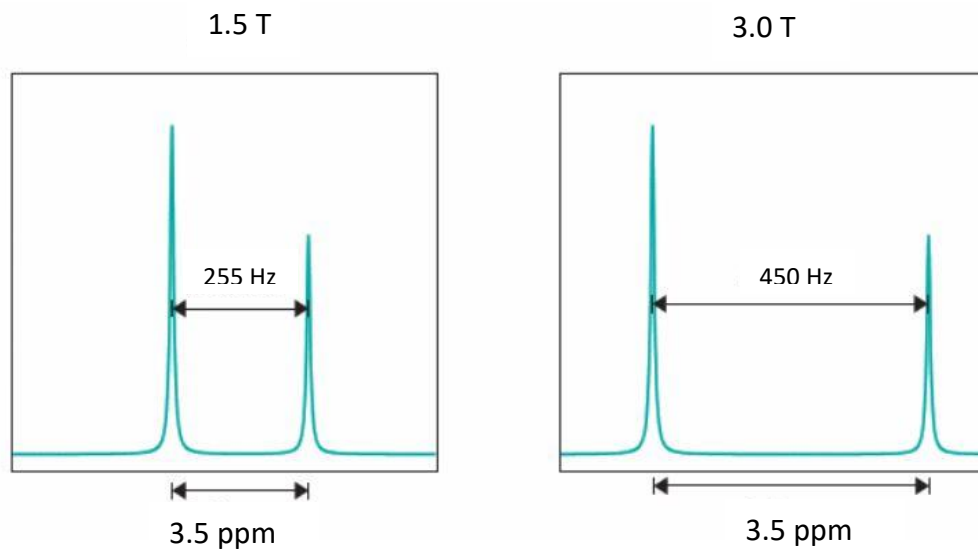


Figure 2.1: Spectrum of the water and fat protons. The frequency difference between water and fat is 3.5 ppm which is equal to 220 Hz and 450 Hz absolute frequency difference in the presence of 1.5T and 3.0T magnetic field. (a) 1.5T magnetic field. (b) 3.0T magnetic field [9].

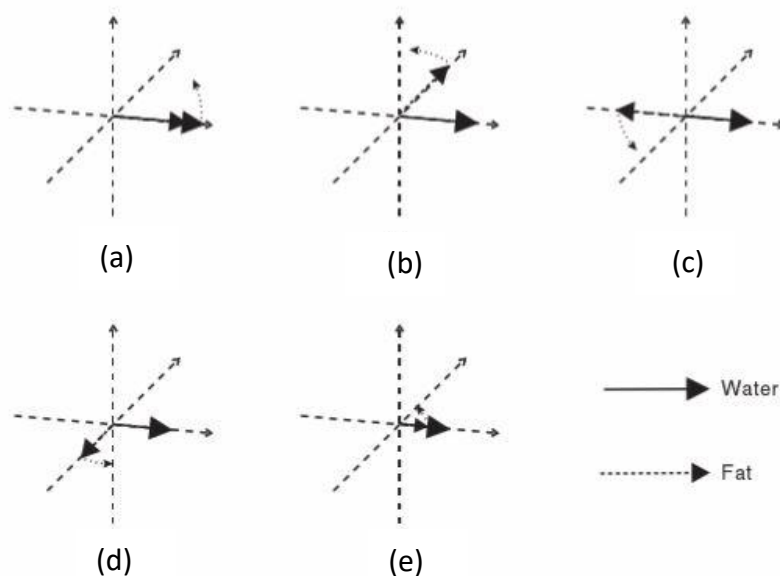
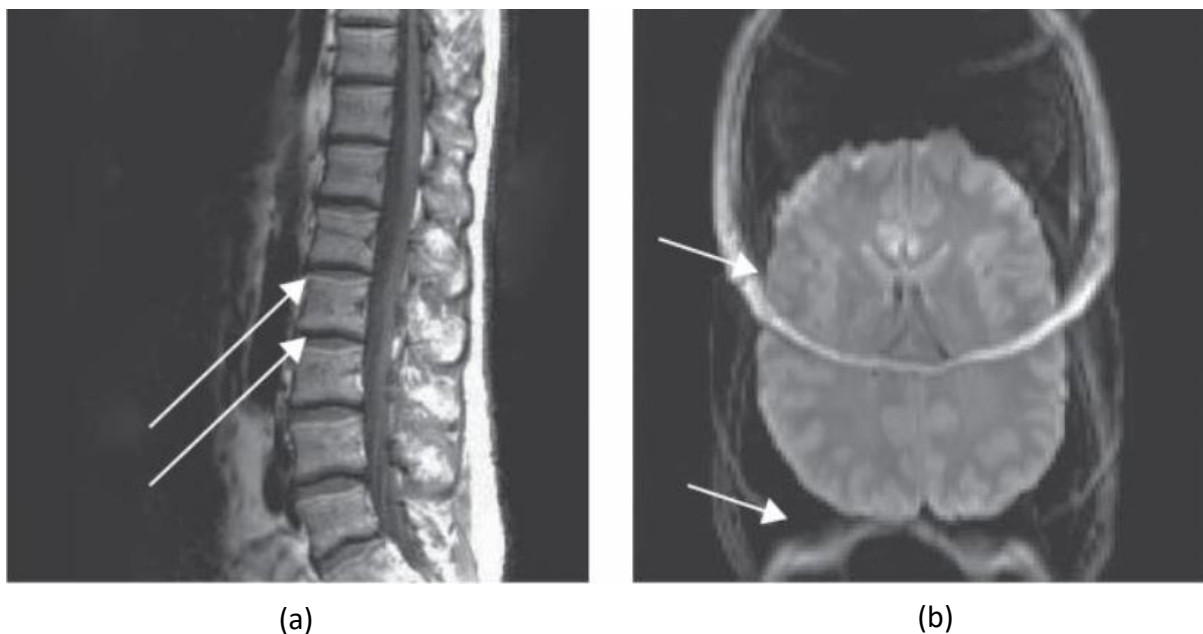


Figure 2.2: Precession of the fat and water protons in different positions. Due to the frequency difference between fat and water protons, water protons precesses faster than fat protons [9].

Although, due to the fact that the fat protons have a lower resonate frequency than the water protons, they will be transferred to the pixels with a lower frequency level in the readout direction. This misregistration is not perceivable in the consistent fat-water tissues. However, at the borders between tissues with an indicatively different fat-water content, the chemical shift artifact is significantly visible as it is shown in the Figure 2.3.



*Figure 2.3: Chemical shift artifact. (a) The light and dark lines at the boundary between the vertebrae and disk (arrows). The image is acquired using spin echo sequence and the receiver bandwidth of 20 Hz. (b) An intense chemical shift artifact in the skull (arrows). The image is acquired using spin echo pulse sequence in the phase-encoding direction [9].*

### 2.1.1.2 Phase cancellation artifact

Phase cancellation artifacts also arise from the precessional frequency difference of the fat and water protons. Exclusively, this kind of the chemical shift-based artifact occurs in the gradient echo images. As it is illustrated in the Figure 2.4, the artifact leads to a black line

around the boundary of the tissue because of the destructive interference of the signals from the pixels containing the fat and water protons [9].

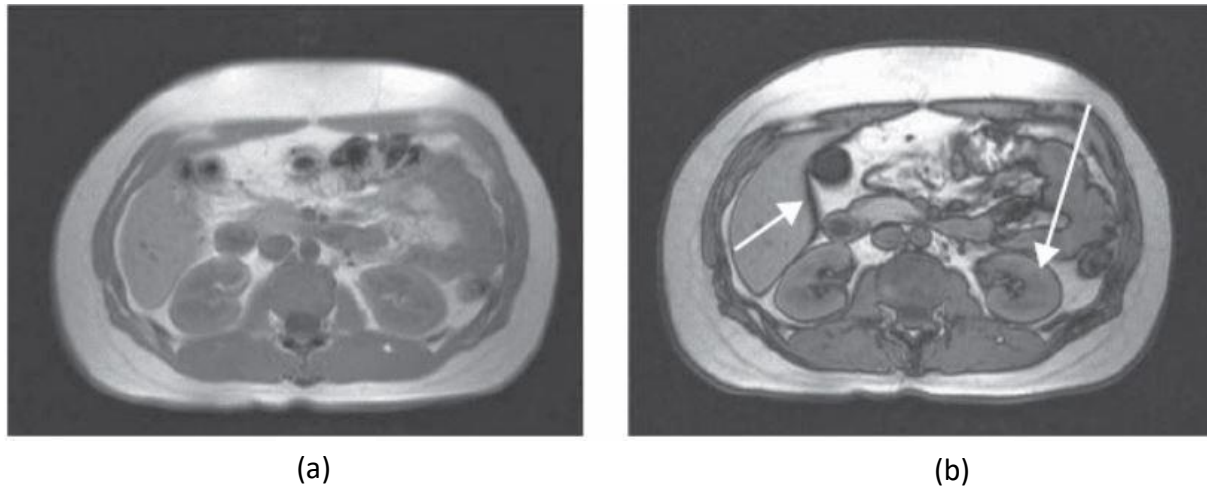


*Figure 2.4: Phase cancellation artifact. (a) In this image (TE, 4.5 ms) fat and water protons have the same phase; therefore, no significant phase cancellation artifact is visible. (b) In this image (TE, 2.2 ms), fat and water protons have the opposite phases; therefore, a dark band has been produced at the interference between liver and kidney (arrows) [9].*

### 2.1.1.3 Noise

This type of the artifacts results from the MRI hardware miscalibration or the electrical connections around the MRI scanner. However, the appearance and severity of the artifact in the image depends on the special source of the artifact as well as the imaging parameters [9]. One type of noise is known as spikes that occur randomly during the image acquisition. As it is shown in the Figure 2.5, spikes appear as waves in the image, and are mostly generated by the electrical components [9].

Another common noise in the MR-images sources from the human body and called thermal noise. This noise causes Gaussian noise and Rician-distributed noise in the both real and imaginary parts of the MR-signals. The noise is very signal-dependent which make extracting

signals from noise a very difficult task. Depending on the pixels intensity in the image, Rician-distributed noise can be estimated as Gaussian-distributed noise [11]. A destructive effect of this noise on the MR-images is the enhancement of the intensity value in the low intensity regions which decreases the total contrast in the image [12, 13].

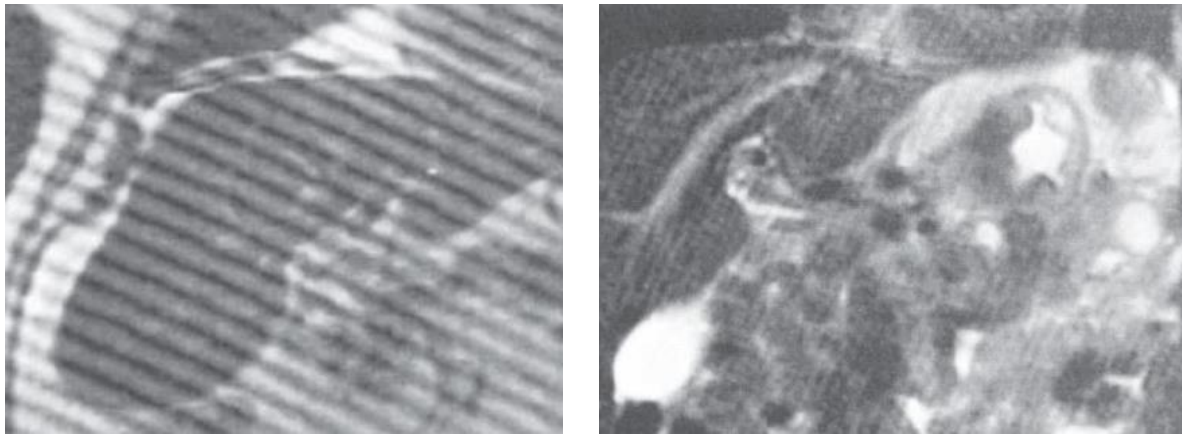


*Figure 2.5: Spikes. The electrical discharge during the image acquisition, generates the spikes as a banding pattern in the image. The distance between the bands depends on the discharge duration [2].*

## 2.2 Instrument tracking methods in interventional MRI

iMRI is an appropriate technique for many types of minimal invasive procedures mostly in the field of biopsies, catheter placement and ablations due to its mentioned advantageous in the section 2.1 [14, 15]. For the visualization of the instrument (e.g. biopsy needle or radio frequency ablation needle) during its progressive penetration to the target structure, the imaging signal is constantly being updated in iterative acquisition with a duration of several seconds each to approach real-time interventional MRI-guidance [16, 17]. Since all instruments must be MRI-safe, meaning that they are not attracted by the magnetic field [18], they do not provide a proton-based resonance signal but are either indirectly visible by the typical artifact that they are creating or completely invisible. In this case the orientation of the interventional instrument must be distinguished with alternative methods to acquire precise alignment information. For this purpose, there are multiple solutions used in interventional applications. The most established one is free-hand instrument guidance which the desired trajectory of the instrument is planned by the surgeon using her finger straight before the actual percutaneous puncture with the instrument [19] (Figure 2.6). However, this approach requires iterative movements either from the clinician or of the patient table in and out of the MRI-tunnel, which is cumbersome, time-consuming and expensive with respect to the costs of the intervention.

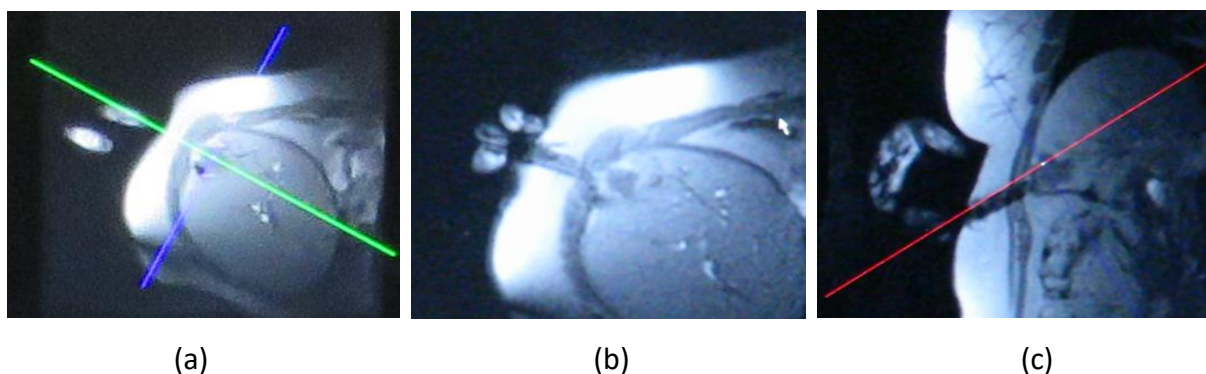


*Figure 2.6: MR-images of a liver biopsy procedure with the clinician's hand indicating the desired puncture point and needle alignment, which is demonstrated by pressing the finger-tip and the finger axis ((a) dent in the skin and green line placed above the finger axis), and guiding the needle during its penetration through the fat-layer (b) until the target area is reached (c).*

### 2.2.1 General tracking approaches

The common alternative tracking methods of the interventional device in the MR-image space are joint encoder tracking, optical tracking, and the use of markers that are visible in MRI. In the first method, the position and orientation of the device (such as mechanical, semi-autonomous- or robotic-devices) is estimated using the device's joint encoders. However, this approach requires the device be fixed to the MRI scanner by a rigid mechanical mounting system and accurately be calibrated according to the scanner coordinate system for each procedure, that is complicated and time-consuming [3, 20, 21]. The optical pose tracking approach requires an optical tracking system for the localization of the interventional device according to the scanner's coordinate system. But, this technique requires a free line-of-sight between the device and the optical camera. In addition, retroreflective spheres or sterilizable LEDs must be attached to the interventional instruments that installation and calibration of them is very costly, time consuming and mostly not appropriate to fit into the close schedule for many applications [22].

In contrast, the fixation of a marker on the interventional device provides the possibility for measuring the device alignment directly from the MR-signal. There are multiple types of markers which can be categorized into active or passive markers. Since the active markers (e.g. direct current coils, resonant rf-coils, gradient field measurement coils) provide signals by influencing or detecting the magnetic field of the MRI, they do mostly require special parameters during the acquisition of a scanning sequence. Furthermore, they consist of metallic components and also can create undesired imaging artifacts [23–25]. In contrast, passive fiducial MRI markers do not contain any metallic substances and can be seen directly in the MR-image [26].

### 2.2.2 Passive MRI marker tracking

Passive marker tracking of instruments in iMRI is defined as the fiducial markers which are embedded within the interventional device for the purpose of the device pose' tracking by

localizing the fiducial markers [27]. The known geometric configuration of the fiducial marker assists to relate the device and the MRI coordinate systems [3]. The main advantage in this approach is the straightforward calibration principal of the marker inside the MRI coordinate system, because both the interventional device and the patient's anatomy can be measured and examined in the same image space [28].

The passive localization markers can be designed either with an arrangement of the MR-visible cylinders or the spheres inside a frame (e.g. Z-frame, + frame, and spherical marker frame) or filling (or coating) the interventional instruments (e.g. catheter) with the MRI contrast agents (such as 4-6 vol % Gd-DTPA) (see Figure 2.7) [29].

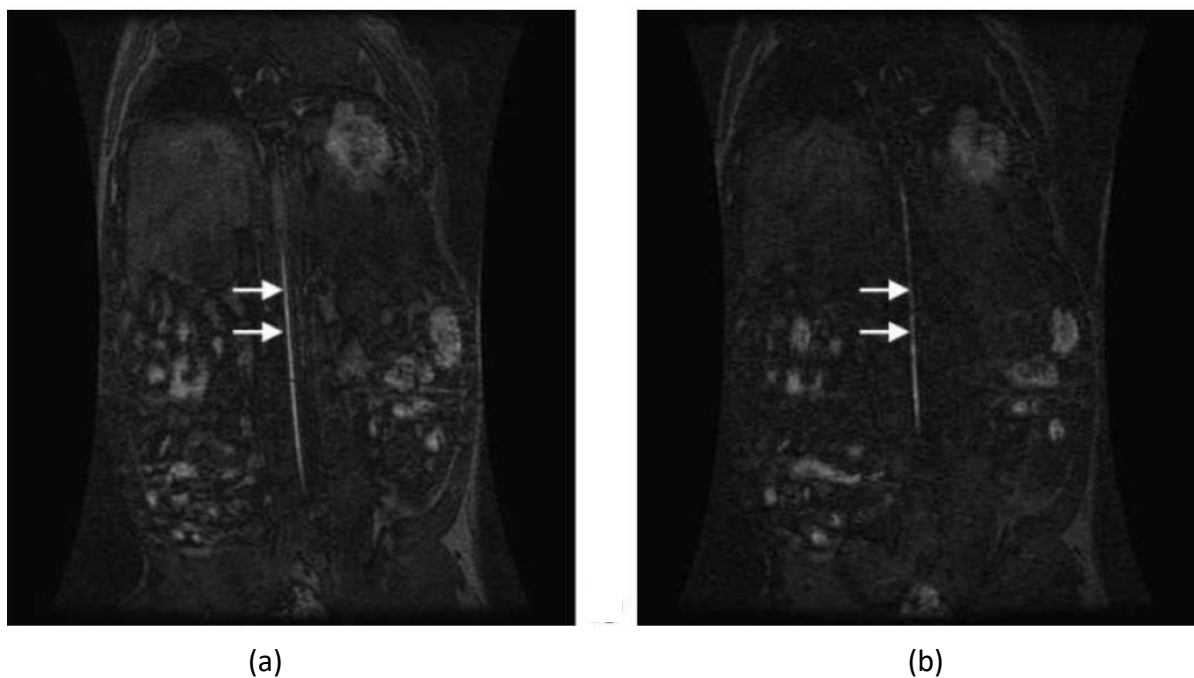


*Figure 2.7: (a) Coronal image of a catheter filled with 4% Gd-DTPA. (b) Coronal image of a catheter coated with  $T_1$ -shortened agent [29].*

The mentioned passive tracking frames have reliable features which enable the estimation of the position and orientation of the marker within the MRI space. Therefore, a rigid transformation matrix can be calculated in order to map any point in the frame coordinate

system to its corresponding point in the MRI coordinate system as it is formulated in the equation 2.2 [3].

$$\begin{bmatrix} \mathbf{P}_{MR} \\ 1 \end{bmatrix} = \mathbf{A} \begin{bmatrix} \mathbf{P}_f \\ 1 \end{bmatrix} ,$$

$$\mathbf{A} = \begin{bmatrix} \mathbf{R} & \mathbf{t} \\ \mathbf{0}^T & 1 \end{bmatrix} \quad (2.2)$$

Where  $\mathbf{P}_{MR}$  and  $\mathbf{P}_f$  are the points in the MRI and the frame coordinate system respectively,  $\mathbf{R}$  is a rotation matrix and  $\mathbf{t}$  is a translation vector.

The + frame is made of two perpendicular visible cylinders, so that the registration matrix can be estimated by localizing each of 4 points in the MR-image. This frame is illustrated in the Figure 2.8 [3].

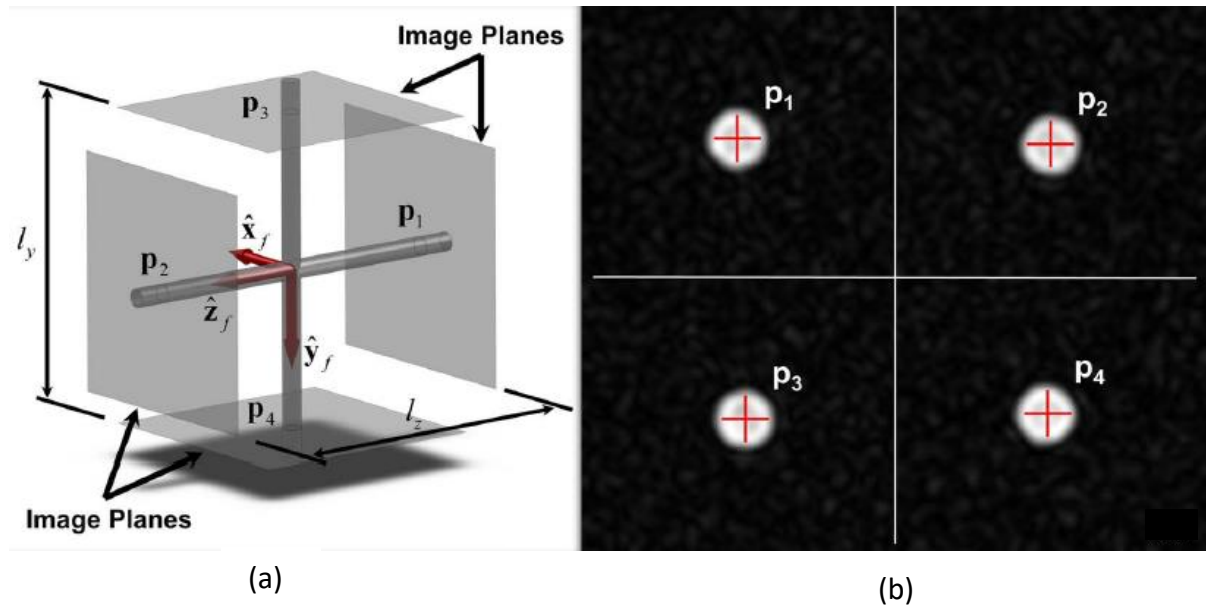


Figure 2.8: The + frame. (a) Design principle of the + marker. (b) The + frame in a 2D-MR-image with four calculated center points of the circular area for the localization [3].



The spherical marker frame consists of three MR-visible spheres as it is shown in the Figure 2.9. The localization of these three spherical markers yields an estimation of a registration matrix that minimizes the  $l^2$ -norm of the error between the points in the image coordinate system and the corresponding points in the MRI coordinate system [3].

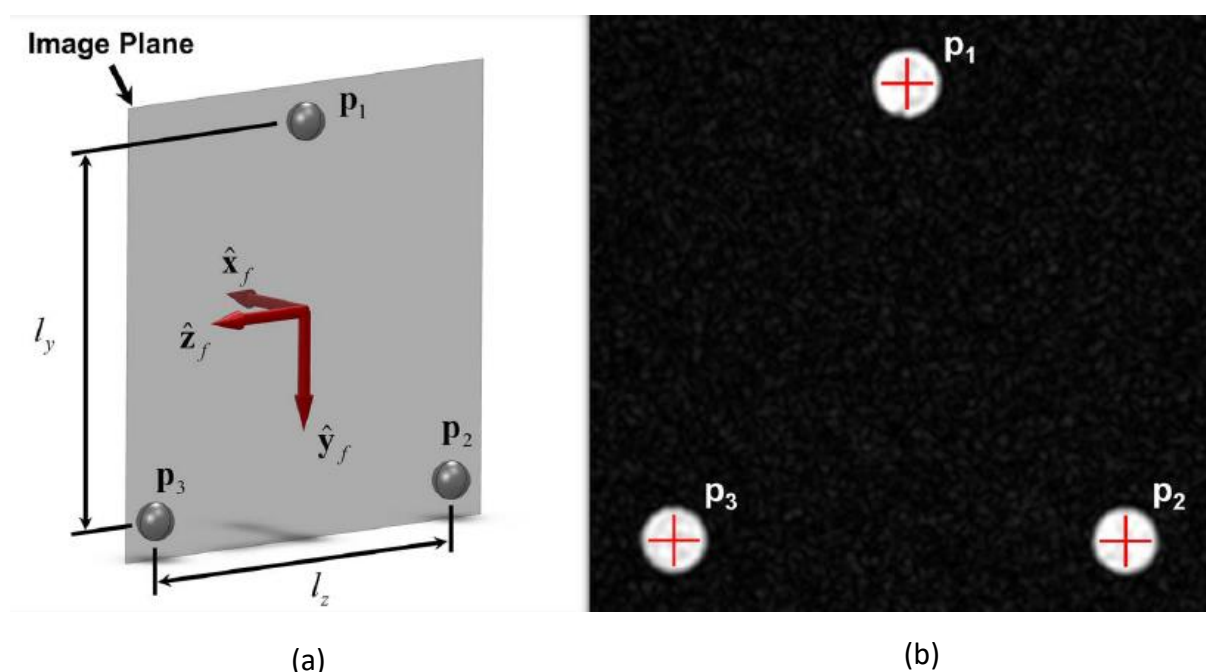


Figure 2.9: The passive spherical frame: (a) Design principle of the spherical frame. (b) The spherical frame in a 2D-MR-image with three center points of the circular areas for the localization [3].

The Z-frame marker is one of the well-known passive marker for the device and instrument tracking and registration in interventional MRI. The main principals of this marker are discussed in the section 2.3.

## 2.3 Principal of the Z-frame marker

For tracking the instrument's alignment in reference to its planned trajectory, the fiducial marker frame from Brown-Roberts-Wells, which is also called Z-frame based on its design of the fiducial marker structures, has been published many times as a concept for possible application in MRI-guided interventions. The marker is designed on the principle of a solid body that is crossed by a three-sided Z-shaped tunnel filled with liquid marker material. There are four vertical tunnels in every edge of the body and three 45° diagonal tunnels connecting all four vertical tunnels in three side faces of the body. Once the marker is measured in the MRI, the tunnel structures are visible in a 2D-image plane as a very distinct pattern of seven circular areas, as it is illustrated in the Figure 2.10.

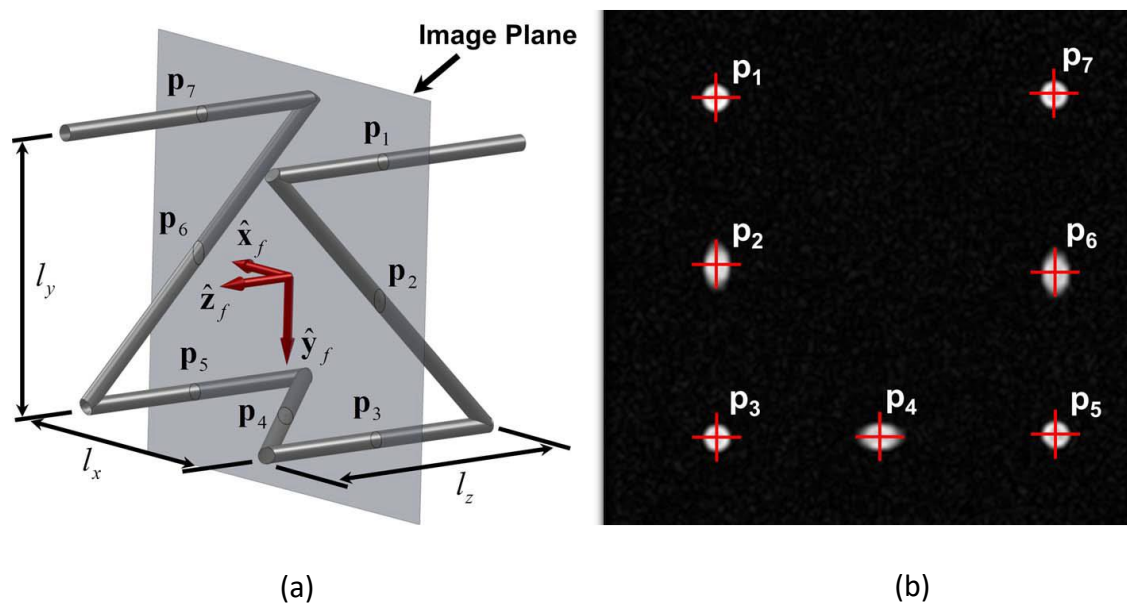
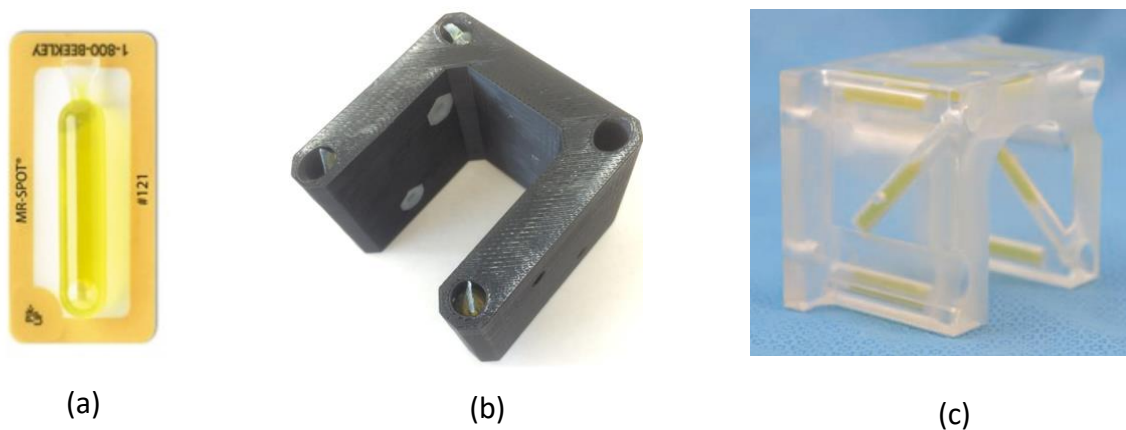


Figure 2.10: (a) Design principle of the Z-frame marker with four vertical (z-direction) and three 45°-diagonal tunnel structures filled with a marker fluid. The pointed image plane crosses all seven tunnels in perpendicular position to the Z-axis. (b) The Z-frame in a 2D-MR-image with view in +Z-direction and with all calculated center points of the circular areas [3].

With the measurement of all distances between the circular areas, the marker alignment can be fully calculated in six degrees of freedom (6-DOF) in reference to the image plane alignment in the MR-image [2, 4, 14, 15]. However, the published marker concepts lacked in their fiducial characteristics or the feasibility for clinical application. Most reasons for it are founded in the design that has always been based on using at least two materials: one for the solid body and one for the fiducial liquid which is enclosed by it. For instance, the Z-frame marker can be fabricated out of seven plastic capsules, which are filled with MRI-visible liquid (e.g. gadolinium: Gd, MR-SPOT® 121, Beekley Corp., Gd-capsule length: 32.0 mm, inner diameter: 6.2 mm) and that are placed inside the internal, z-shaped tunnel structures of the solid body, which is shown in the Figures 2.11 (a) and (b). Another method that has been applied for the Z-frame fabrication is the direct filling of a solid body with the internal Z-shaped tunnel structures. This is made by one bore-hole which needs to be sealed up after filling, see Figure 2.11 (c). That method owns the disadvantages for a complex and expensive fabrication process and a high risk for leakages.



*Figure 2.11: (a),(b) Z-frame concept with Gd-based marker capsules inserted into a solid body frame (a and b). (c) Design concept with marker liquid directly injected into tunnel structures of the marker body but requiring additional sealing [23].*

The mentioned method has the disadvantage that the plastic wall of the capsule, which is located between the body's wall and the beginning of the MRI-visible liquid, can affect the

precision of the marker detection negatively by shifting the center points of each tunnel due to geometric irregularities (Figure 2.12 (a) and (b)). Another issue that affects the marker precision in this design can be caused by the potential of certain artifacts. As it is discussed in the section 2.1, if the chemical shift artifact of a liquid marker material is too high, there is a relevant shift of the real center point to a virtual center point that results from the accumulation of the fat-based signal and the water-based signal. In worst case the geometric irregularities are superimposed with the chemical shift based irregularities leading to a significant inaccuracy of the precision of the marker (Figure 2.12 (c)) [30].

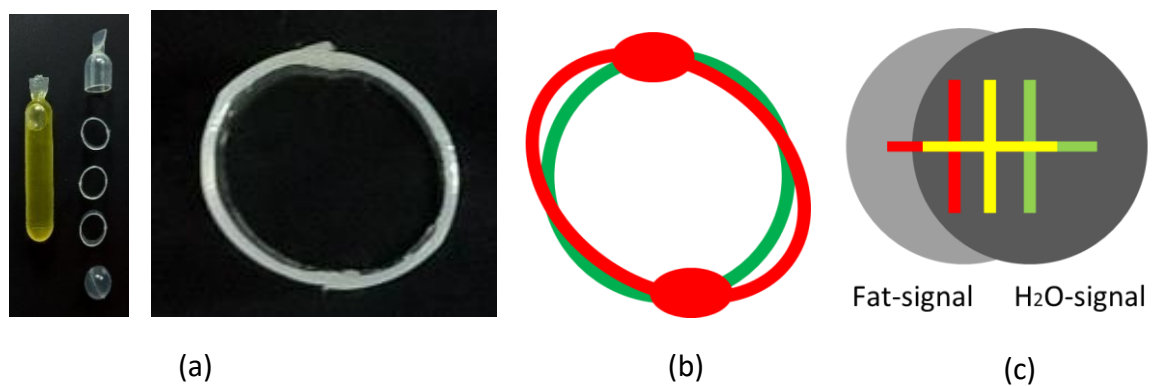


*Figure 2.12: Overview on potential geometric defects for fiducial markers using Gd-filled capsules (a and b) and effect from the interpolated center point between the fat- and water-based circular artifact areas (c).*

In this project, a new concept for a fiducial marker is implemented that is fully additively manufactured (commonly known as rapid-prototyping = RP) with only one polymer material. This one material is used for the fabrication of the solid Z-frame body and the internal marker liquid by using the method of stereolithography (SLA) technology. The fabrication material for the marker-model is a liquid and photosensitive polymer, which is locally hardened by a laser beam. The model is built up layer by layer with the laser beam hardening the model volume. The principle of the SLA-method allows the enclosure of defined geometrical structures filled with unhardened liquid resin. These structures are created inside the solid model body without any openings to the outside. For this reason, only the structure surrounding the desired marker-geometry is hardened by the laser. The marker-geometry itself remains a

liquid [30]. Since it is made entirely from polymeric material, this marker is passive and totally MRI-safe. The novel physical and chemical characteristics of this additively manufactured marker are detailed in the section 3.1.

# 3 Methodology

## 3.1 Z-frame marker characterization

### 3.1.1 Z-frame physical structures

In this project, the new physical feature structures of the Z-frame have been developed which are intended to improve the accuracy and speed of the registration procedure in the interventional MRI. Figure 3.1 illustrates two new features: center pointing triangles and the z-axis indication triangle.

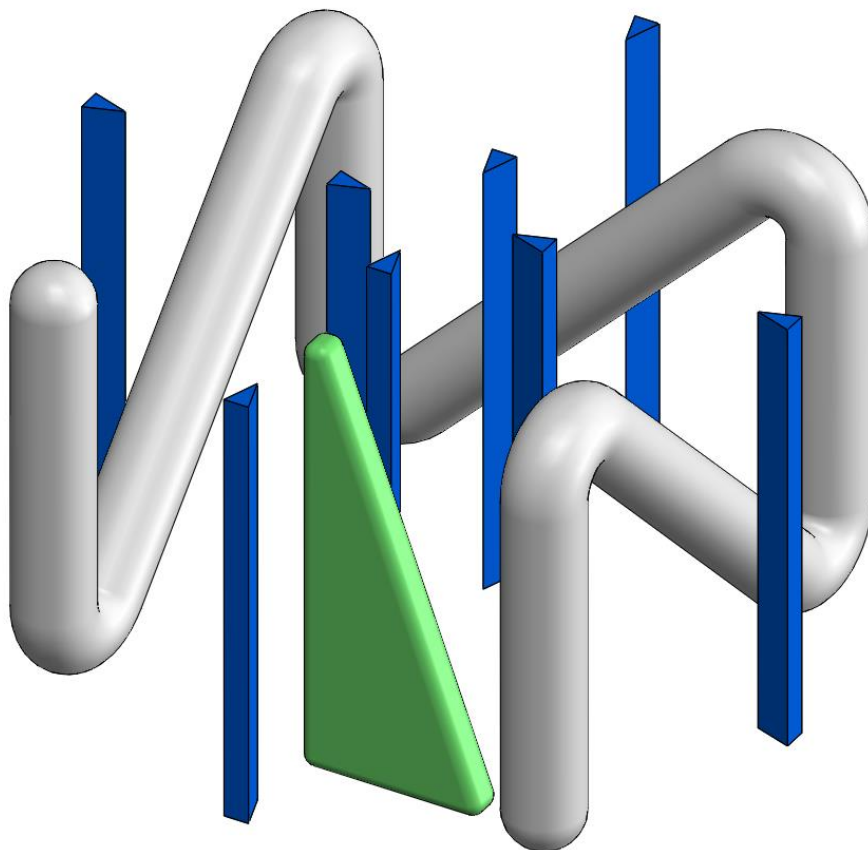


*Figure 3.1: A 3D CAD-view of the Z-frame-marker structures. The center pointing triangles (8 small blue triangles) and the z-axis indication triangle (the green triangle).*

### 3.1.1.1 Center pointing triangles

A successful intervention under MRI depends mostly on an accurate determination of the position of the needle insertion point based on the desired target area. As discussed in the literature survey (see section 2.2), generally, the needle entry point is indicated by the surgeon finger in the real-time image acquisition. However, the alignment of the image plane based on this method is time-consuming and cumbersome due to the iterative movements of the patient table.

In this work, the center pointing triangles allow an accurate alignment of the image planes according to the center of the marker. Figure 3.2 (a) shows a coronal view of the Z-frame in which the green line is the transversal imaging plane and the red line indicates the sagittal imaging plane. In order to align the two planes in the center of the Z-frame accurately, the cross-section point of the two planes should be aligned with the four inner triangle shapes.

It has to be mentioned that the center pointing triangles not only indicate the desired alignment of the two perpendicular planes but also of the surgical instrument (e.g. Needle) trajectory which enables the tracking of the needle pathway during the insertion.

### 3.1.1.2 Z-axis indication triangle

After localization and registration of the instrument, an accurate guidance of the instruments is required to reach the target. Consequently, the coordinate system of the Z-frame marker has to be determined in the imaging coordinate system. The correct orientation of the coordinate system can be detected based on the Z-axis indication triangle position (the green square in Figure 3.3). The role of this feature is the determination of the correct orientation of the Z-frame marker which will be discussed in the section 3.2 .

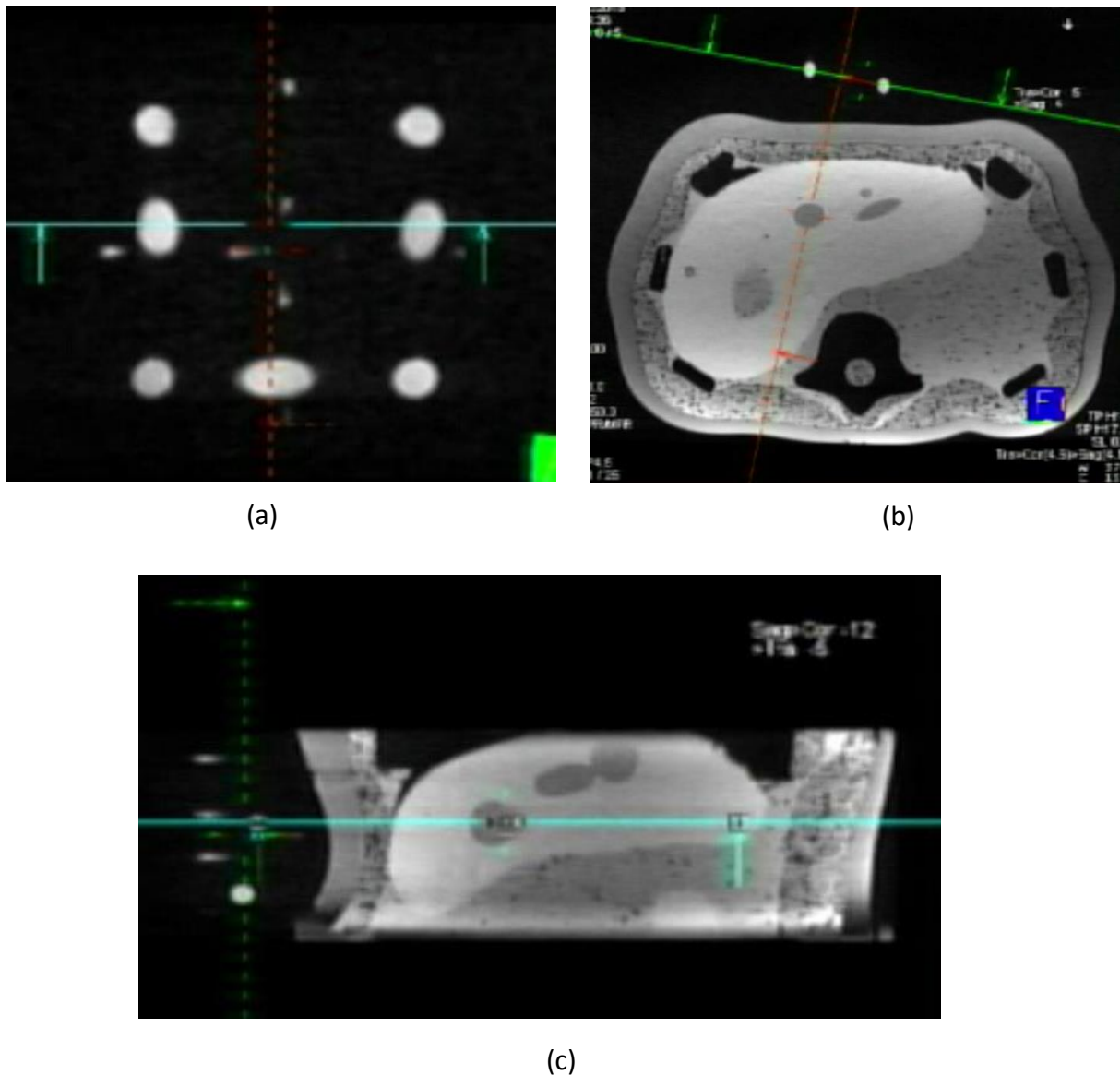


Figure 3.2: (a) A coronal view of the Z-frame representing the sagittal and axial imaging planes as projections (turquoise and the red line) close to the center of the Z-frame. (b) Transversal view of the Z-frame and the liver phantom (3D abdominal phantom #057A, CIRS Inc.). (c) Sagittal view of the Z-frame and a liver biopsy phantom.

### 3.1.1.3 Square-shaped internal tunnel structure

The automated alignment detection algorithm (section 3.2) depends on the accuracy of the detected centroids of the fiducial markers. However, the coordinates of the fiducial markers



may not be accurately estimated due to the suboptimal imaging techniques. The square shaped tunnels (Figure 3.4) provide the ability to estimate the pixel distortion at the edges which is easier for the retrieval of the related signals. According to the proposed method in the section 3.2, which identification of the center points in each fiducial marker is based on its pixel volumes, the signal retrieval at the fiducial edges helps an accurate calculation of the centroids coordinate systems.

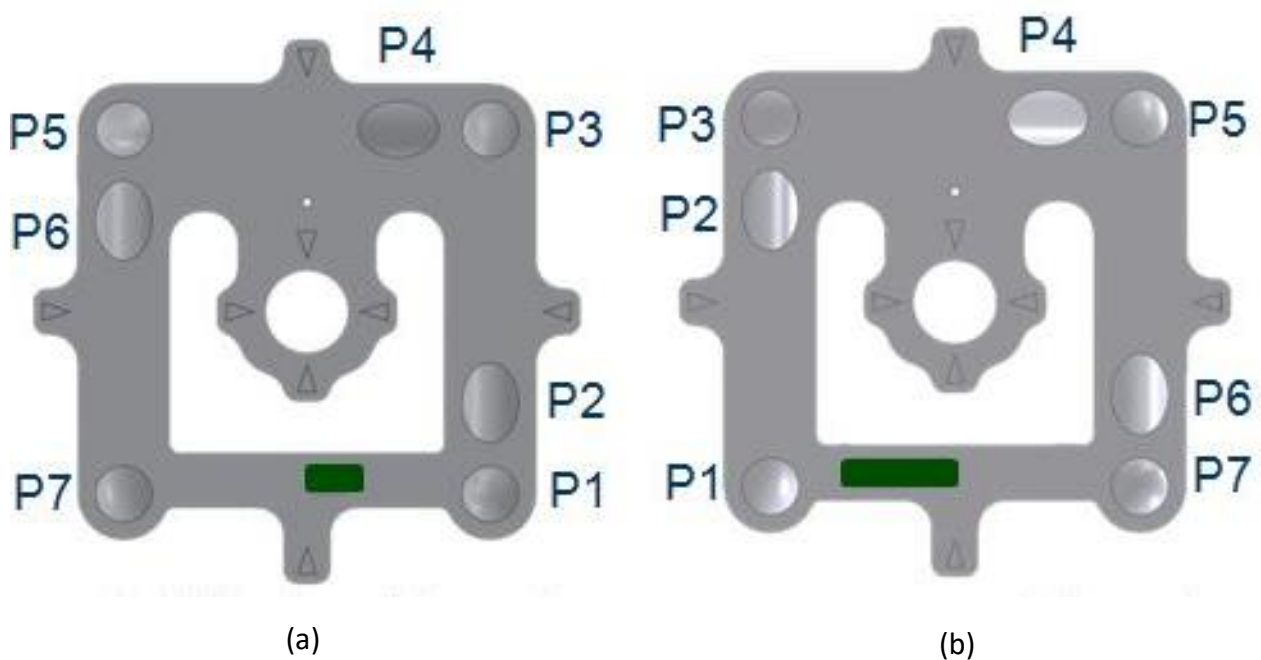


*Figure 3.3: The CAD view of the Z-frame marker with the Z-axis indication triangle (green square in the 2D view). (a) Top view of the marker with  $z=+10$  mm (the indication triangle (the green square) is in the right side of the marker). (b) Bottom view of the marker with  $z=-10$  mm (the indication triangle (the green square) is in the left side of the marker).*

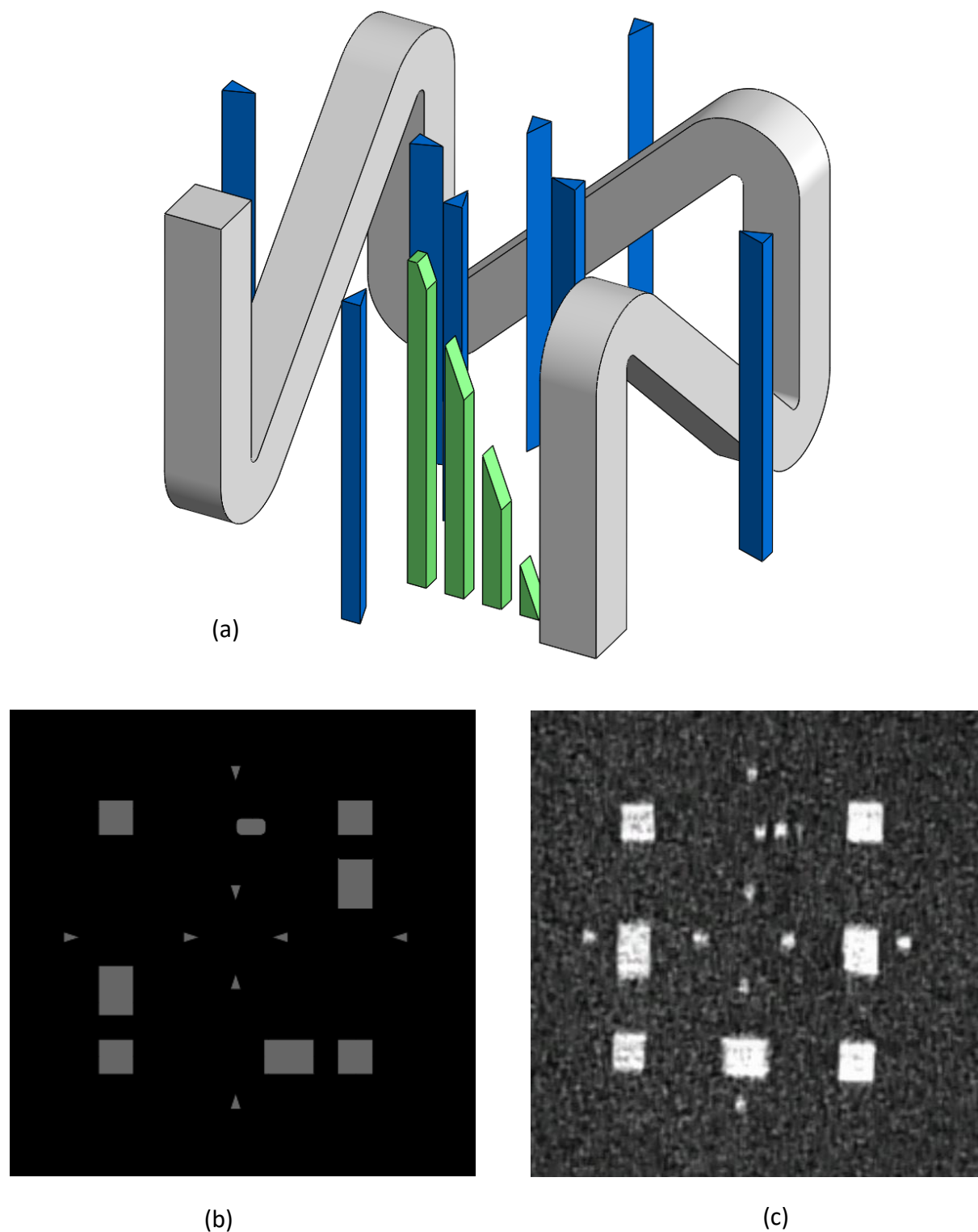


*Figure 3.4: (a) 3D-CAD view of the square shaped Z-frame. (b) 2D-CAD view of the square shaped Z-frame. (c) 2D-captured-MRI image of the Z-frame marker with square-shaped tunnel. The pixels at the edges of the fiducials in the left side of the marker are distorted by noise; however the known size and shape of the fiducials help retrieval of the pixels.*

### 3.1.2 Z-frame marker spectroscopy

For MRI guided minimal-invasive procedures the visualization of therapeutical instruments for biopsies, catheter placements, and tissue ablations, is absolutely essential. However, MR safe instruments usually are — depending on the material used — either not visible at all or only indirectly visible due to susceptibility artifacts generated by the device material.

With prior knowledge of the resin's relaxation times, the optimal resin for a given imaging protocol (e.g. liver biopsy) could be determined before marker fabrication. Each resin has a different, but unknown chemical composition and, thus, potentially different longitudinal (T1) and transversal (T2) relaxation times. The contrast in MRI is largely driven by these relaxation times [31]. Therefore, the visibility of the liquid resin within the marker depends on the used imaging protocol and relaxation properties of the resin.

As a first step to enable MRI markers personalized to a given imaging scenario, this section aims to establish a protocol to determine T1 and T2 relaxation times of the resins used in the stereolithography process.

#### 3.1.2.1 Determination of the resin relaxation times

T1 and T2 relaxation times are experimentally determined for the initially selected stereolithography resins: VisiJet SL Tough, VisiJet SL Clear both from 3D Systems, Inc., and Formlabs FLGPWH03 from Formlabs Inc. Each of the three resins have been stored in separate containers before placing them inside a transmit–receive birdcage head coil of a 3T Skyra MRI system (Siemens Healthineers, Germany).

Measurements are acquired with a spin echo (SE) sequence using a single 4 mm thick slice with 1 mm in-plane resolution. For T1 estimation an inversion recovery pulse is included and the inversion time (TI) is varied between measurements (five different TIs between 23 ms and 2,000 ms). For the T2 estimation the echo time (TE) of the SE is varied accordingly (five different TEs between 5.5 ms and 200 ms), Figure 3.5.

Relaxation times are then calculated for each resin within automatically computed region of interests (based on image thresholding). For each voxel within the region of interest a mono exponential decay is fitted to the signal evolution over TI/TE. The final relaxation time is computed as the mean  $\pm$  standard deviation over all voxel for a given resin. For the T1 relaxation the following signal equation is used [32]:

$$S(TI) = S_0(1 - 2e^{-\frac{TI}{T_1}}) \quad (3.1)$$

with  $S(TI)$  as the mean measured signal at TI and  $S_0$  capturing residual T2 weighting, proton density, and coil sensitivities. For the T2 relaxation time the following signal equation is used [32]:

$$S(TE) = S_0 e^{-\frac{TE}{T_2}} \quad (3.2)$$

with  $S(TE)$  as the mean measured signal at TE and  $S_0$  capturing proton density, and coil sensitivities. Goodness of fit is evaluated with the coefficient of determination ( $R^2$ ).

All processing is done in MATLAB 2015b (MathWorks, USA).

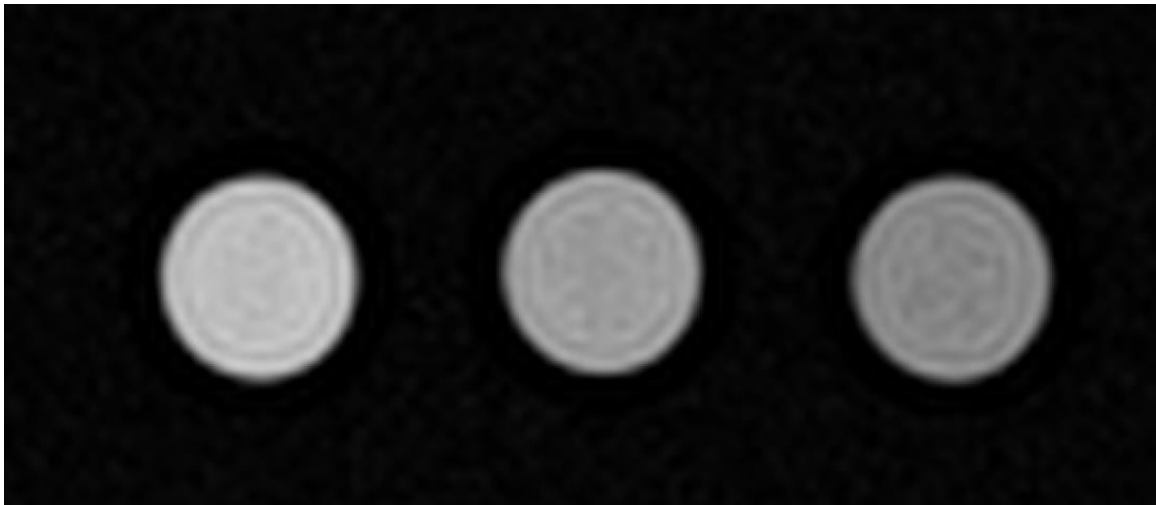


*Figure 3.5: Measured image slice of the three cylindrical resin containers (left: VisiJet SL Tough, middle: VisiJet SL Clear, right: Formlabs FLGPWH03).*

### 3.1.2.2 Experimental results

The T1 and T2 relaxation times (Table 3.1) of the tested resins are calculated based on the experimental results. Figure 3.6 shows the mean fitted relaxation time compared to the measured signal. The overall goodness of fit for all estimates is high ( $R^2 > 0.99$ ).

T1 estimates for all resins differed among each other by up to 9.97 % and has an average T1 relaxation time of 164.4 ms, which is considerably shorter than human tissue such as subcutaneous fat (382 ms), liver (809 ms), or the medulla of the kidney (1,545 ms) [33].

T2 estimates for all resins differed among each other by up to 10.74 % and had an average T2 relaxation time of 22.3 ms, which is shorter than human tissue such as subcutaneous fat (68 ms), liver (34 ms), or the medulla of the kidney (81 ms) [33].

| Resin             | T1 Relaxation Time [ms] | T2 Relaxation Time [ms] |
|-------------------|-------------------------|-------------------------|
| VisiJet SL Tough  | 156.7 $\pm$ 2.9         | 23.2 $\pm$ 0.8          |
| VisiJet SL Clear  | 174.0 $\pm$ 16.7        | 20.7 $\pm$ 1.0          |
| Formlabs FLGPWH03 | 162.6 $\pm$ 3.6         | 22.9 $\pm$ 1.2          |

*Table 3.1: Estimated mean  $\pm$  standard deviation T1 and T2 relaxation times for three different resins.*

### 3.1.2.3 Future work

This study determines the MRI T1 and T2 relaxation times for resins used to serve as MRI marker material for the first time. In the future, these results will enable to predict the marker visibility before scanning. Thus, for a given scenario in interventional MRI application (e.g. liver biopsy) the optimal marker can be fabricated with the optimal resin. However, relaxation times for more resins should be estimated in the future as the measured resins do not vary considerably among each other, limiting the potential for personalizing interventional

applications through T1 and T2 relaxation time matching. Furthermore, extending the signal equation and MR measurement to account for system imperfections (e.g. imperfect inversion pulses, or transmit and receive inhomogeneities) might improve the estimates.

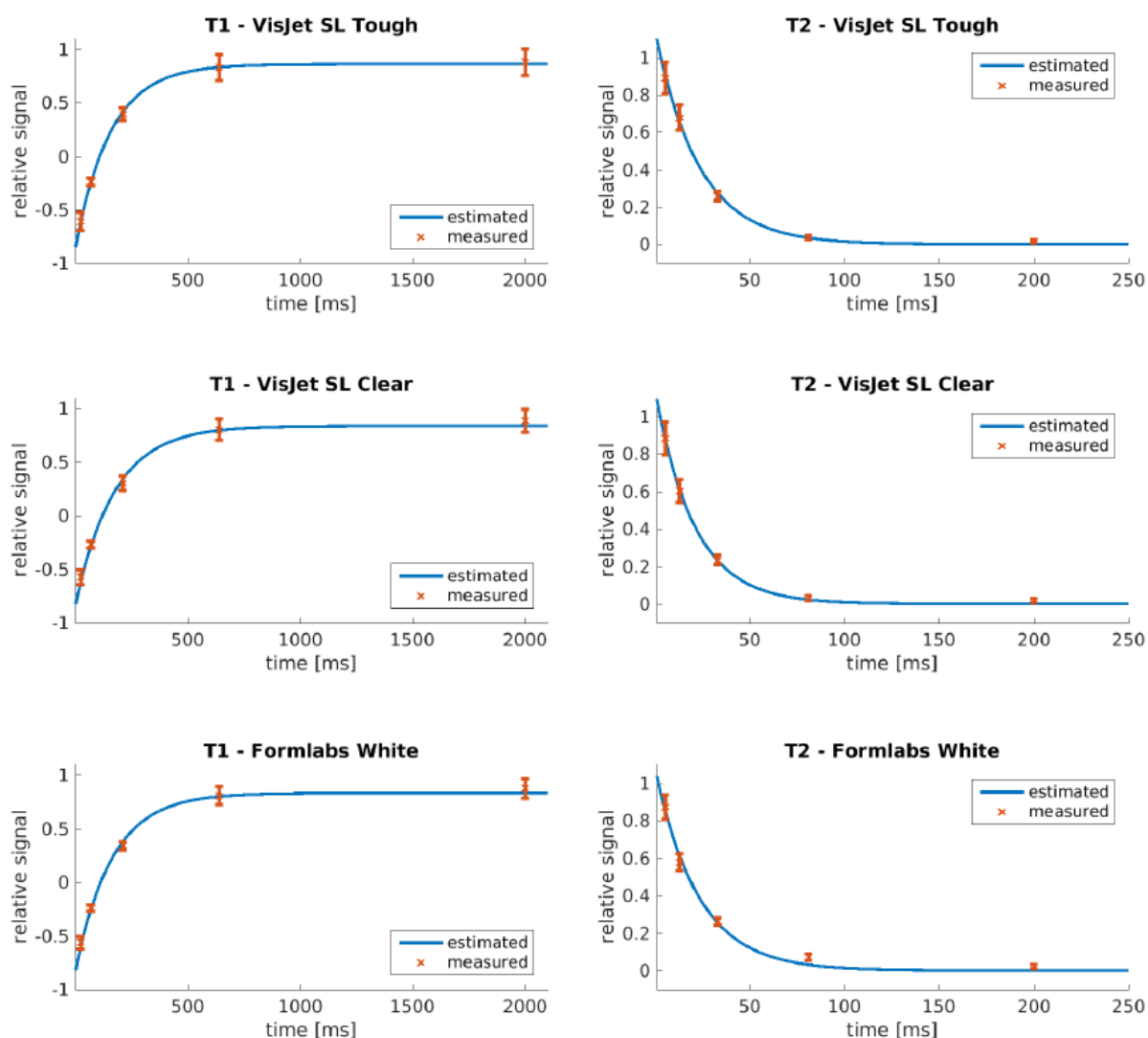
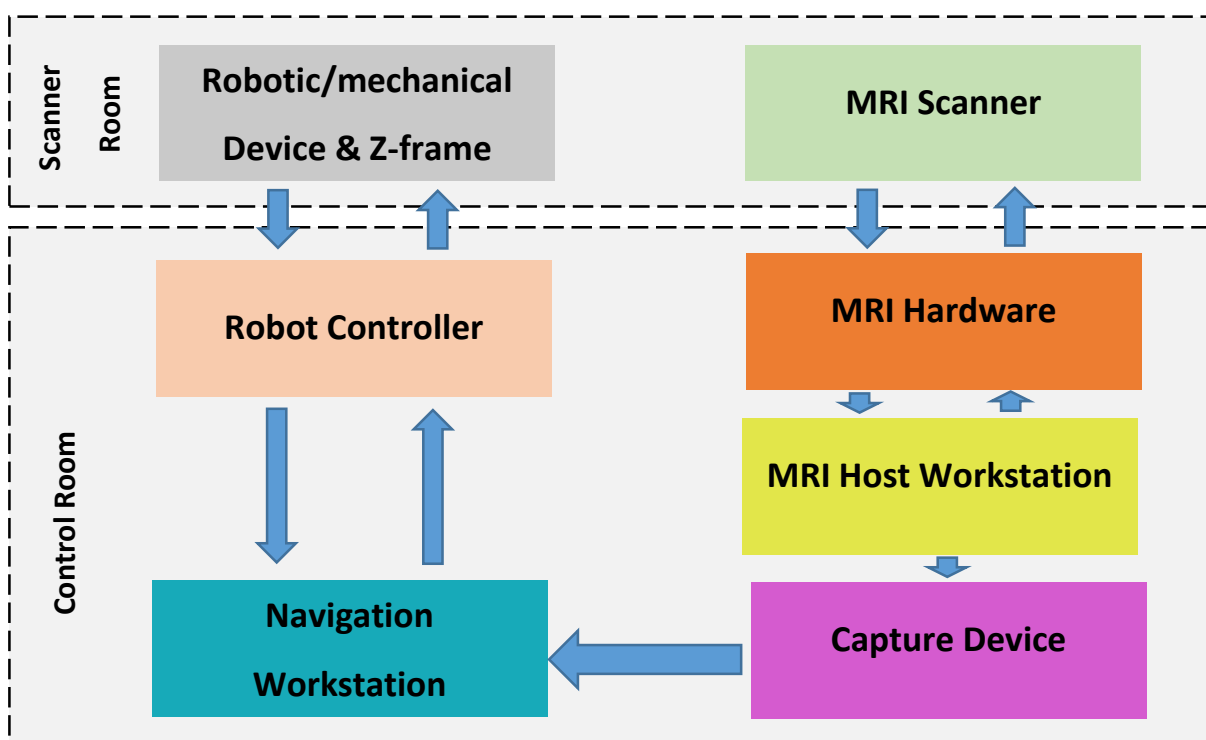


Figure 3.6 : Comparison of measured and estimated T1 and T2 relaxation times for three different resins. Measured data of the normalized signal intensity is shown as error bars (mean  $\pm$  standard deviation). After fitting the signal model (using the mean T1/T2 from Tab.3.1) the estimated relaxation curve is overlaid.

### 3.2 Alignment detection algorithm

The implemented algorithm for the automated alignment detection of the Z-frame marker consists of two main steps. At first, the Z-frame structures are extracted from the captured-MR-images, then the center point of each fiducial is computed. This stage is presented in the section 3.2.2, where different filtering methods for noise suppression and feature enhancement are introduced. The next stage is the localization and registration of the Z-frame marker in the MRI coordinate system that is discussed in the section 3.2.3. All the processing methods in this chapter are implemented in Matlab R2017a and R2018a. Figures 3.7 and 3.8 show the general system configuration and flowchart of the procedures.



*Figure 3.7: The system configuration and data flow during tracking and registration procedure. Once a single 2D image of the Z-frame is acquired by the MRI scanner and is transferred to the MRI host workstation, the capture device acquires a snapshot of the MRI workstation monitor for further processing in the navigation workstation. Therefore, the required motion of the robotic or mechanical device based on the alignment of the Z-frame is calculated which will be commanded to the robotic device via robot controller.*

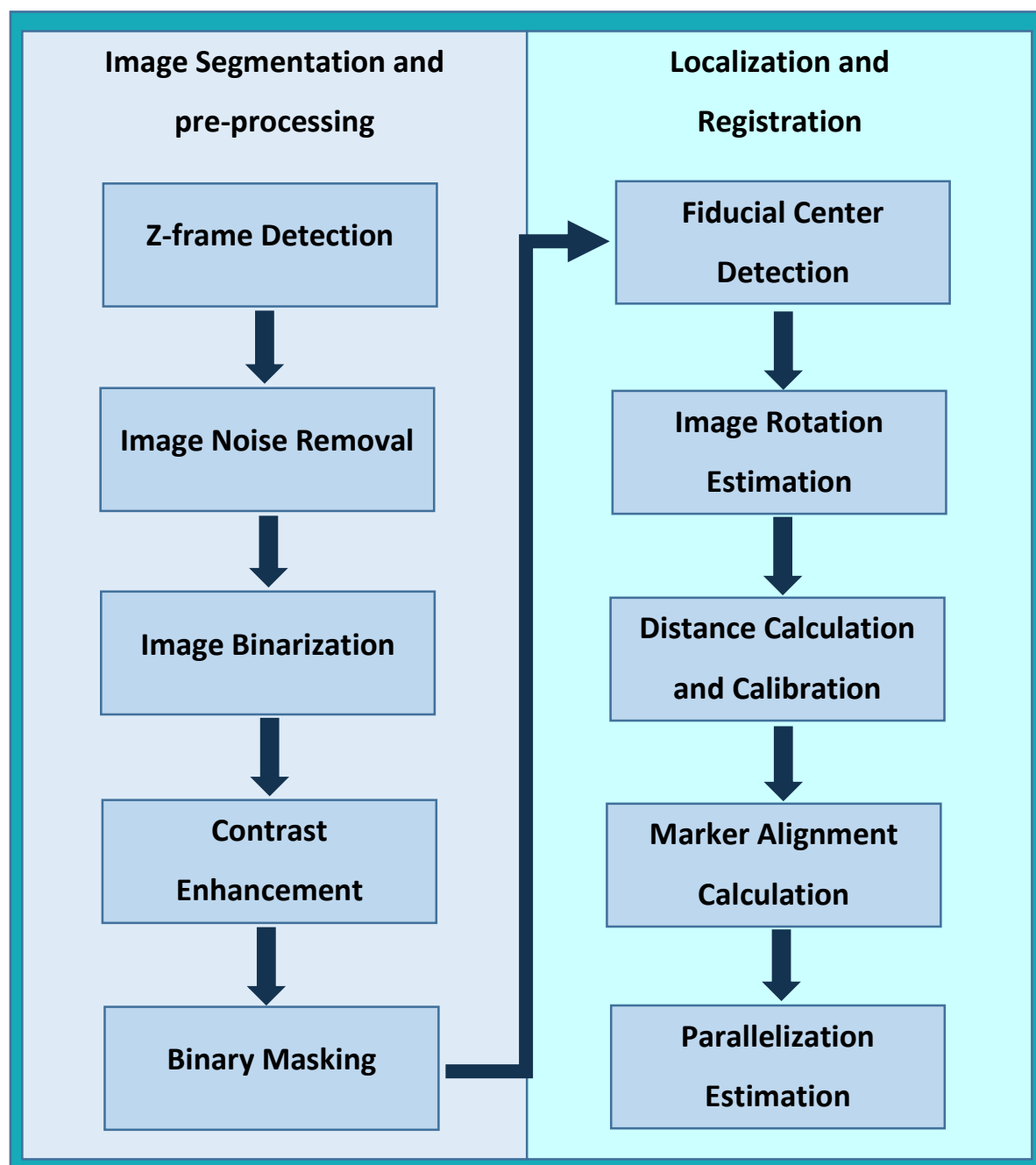


*Figure 3.8: The flowchart of the two main stages of the automatic alignment detection algorithm. This represents the procedures in each stage.*



### 3.2.1 Data acquisition

In this project a new image acquisition setup is proposed to facilitate the registration and tracking process in a nearly real-time workflow by eliminating the need for an additional interface which connect the MRI scanner, the navigation workstation and the robotic controller. The setup of the proposed approach is shown in the Figure 3.9, where a capture device (Hauppauge- HD PVR 2) is employed in a loop between the MRI monitor and the processing laptop. Therefore, each data on the monitor screen is shown and saved on the processing laptop.

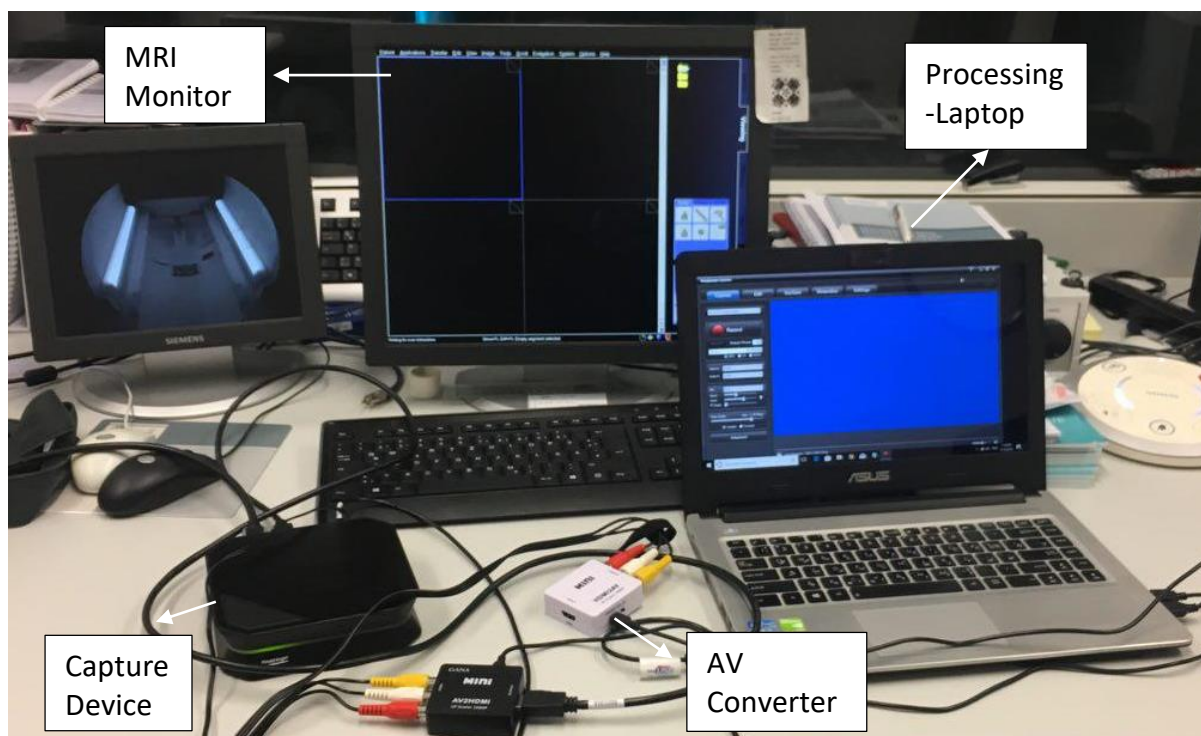


*Figure 3.9: Setup configuration of the image acquisition procedure in the MRI control room.*

In addition, decoding of the protected patient imaging data is needed to adapt the setup flexibly in different MRI-systems. Accordingly, two converters are used to decode the MRI data which pass through the capture device. However, the use of the converters affects the quality and resolution of the decoded images negatively.

Two different types of the decoders have been tested in this work to verify their applicability in the proposed setup: analog converter (AV converter) and VGA converter. Figure 3.11 shows a comparison of the quality performance of the capture device without data decoding (Figure 3.11 (c)), and with decoding using AV converter (Figure 3.11 (a)) and VGA converter (Figure 3.11 (b)). Even though the VGA converter provides the images with a higher resolution and contrast than the AV converter, it is not compatible with the MRI hardware system.

An alternative to the capture device and the converters is a camera which can be positioned in front of the MRI monitor to acquire the image directly from the screen. This approach is compatible with all MRI systems without the need for the decoding process, but it has several disadvantages such as providing the low-quality images (Figure 3.10 (a)) and calibration complexity.

In this project, the capture device and AV converter are employed, since this setup is compatible with the MRI hardware system which provides the adequate image quality for the image processing task. Figure 3.10 (b) shows a snapshot of the MRI screen from a T1W image of the Z-frame marker using the capture device and the AV converter.

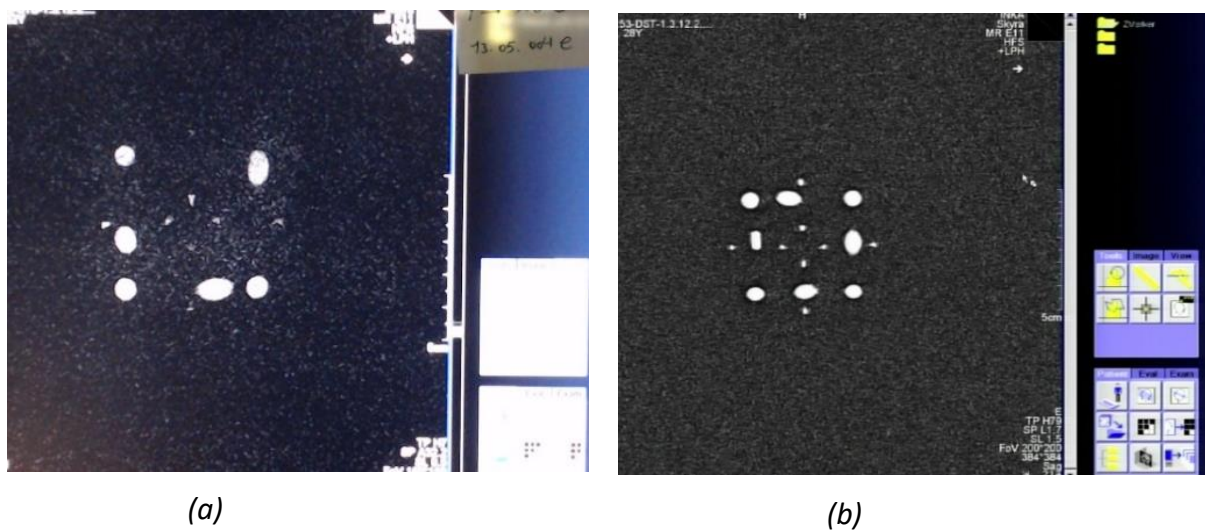


*Figure 3.10: Captured-MR image (T1W image) of the Z-frame marker. (a) Image is acquired using a camera in front of the MRI monitor. (b) Image is captured using the capture device and the AV converter (the setup is shown in Figure 3.9).*

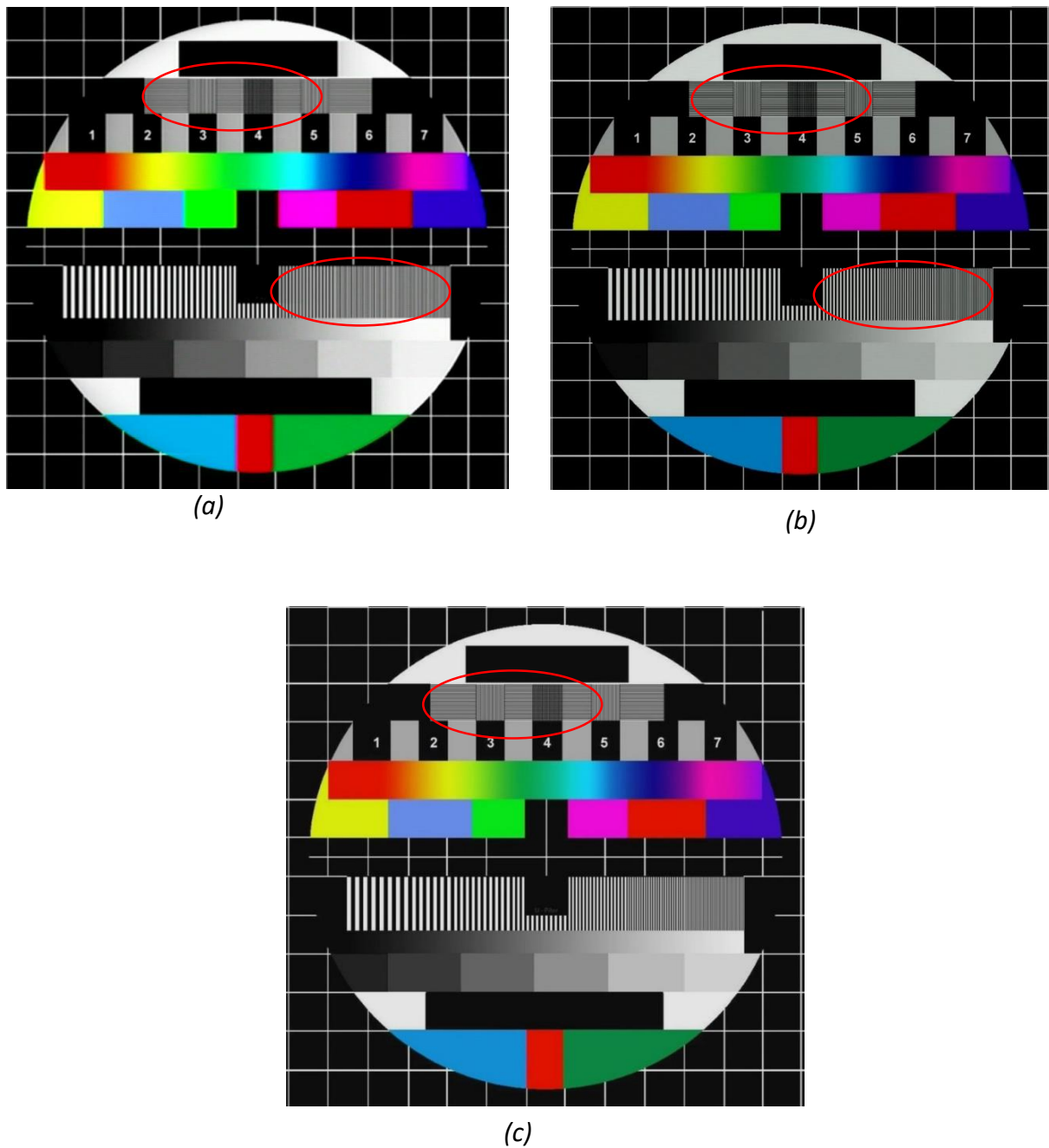
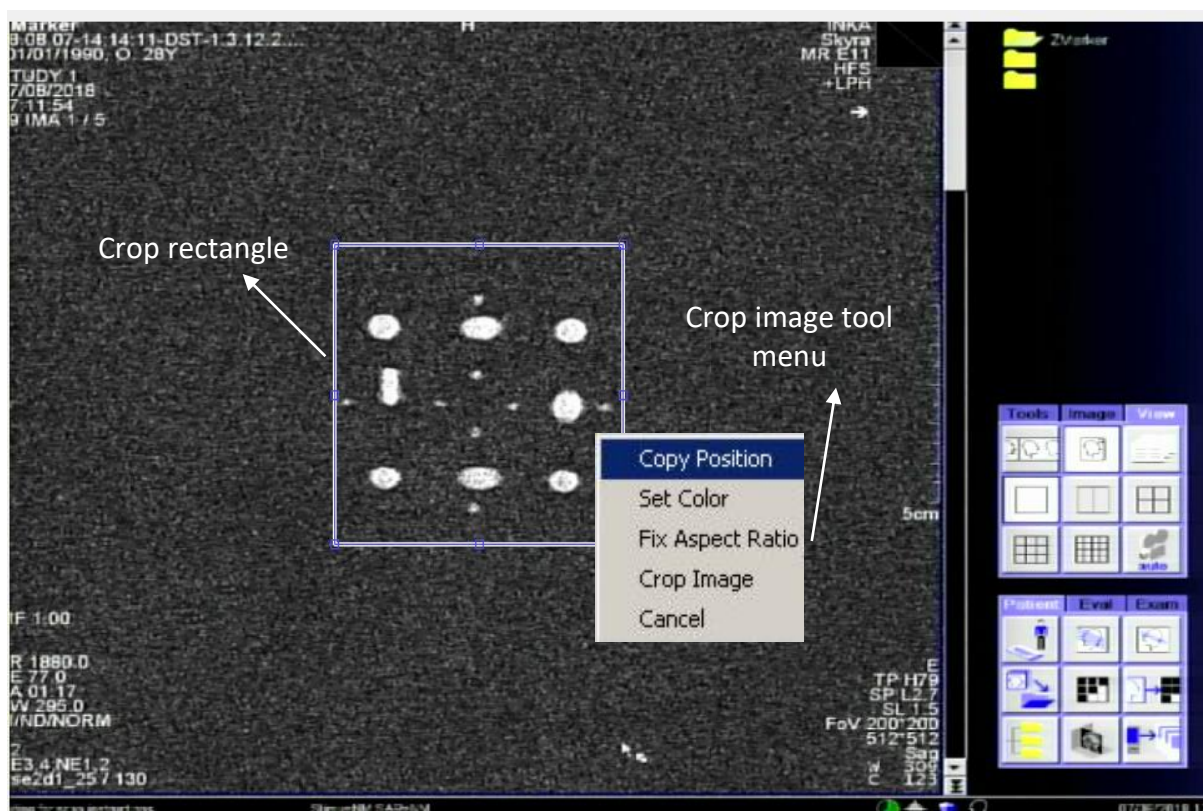


Figure 3.11: Quality test image which is captured from a monitor with different methods. Image is captured by using (a) the capture device and the AV converter, (b) the capture device and the VGA converter, (C) only the capture device with HDMI cable (HDMI resolution). The red ellipses show the regions which are distorted during the decoding process.

## 3.2.2 Image segmentation and pre-processing

### 3.2.2.1 Z-frame marker cropping

Detection of the Z-frame marker in different position, orientation and scaling from the captured-MR images is an important step to determine the marker alignment. One way to separate the Z-frame from the full-screen image is by using the mouse to perform the crop operation interactively by defining a movable and resizable bounding box over the region of interest as it is illustrated in the Figure 3.12. However, this technique requires the user to repeat the cropping process separately for each new image.



*Figure 3.12: Cropping operation for extracting the Z-frame marker from the captured-image.*

### 3.2.2.2 Automatic detection of the Z-frame using Faster R-CNN

In this study, a deep CNN framework is implemented with the non MRI-system-specific design which performs the detection process automatically. This algorithm is able to detect and segment the marker structures from the images which are acquired using different imaging properties or different MRI user interfaces.

Commonly, there are three main frameworks for object detection based on deep CNNs. Regions with CNN features (RCNN), Fast Region-based Convolutional Network (Fast RCNN), and Faster Region-based Convolutional Network (Faster RCNN) [34].

- Development and general principal of convolutional neural network

CNN is made of several layers, a convolution layer, a feature pooling layer, and a fully connected (FC) layer [34]. The flowchart of a CNN is provided in Figure 3.13.

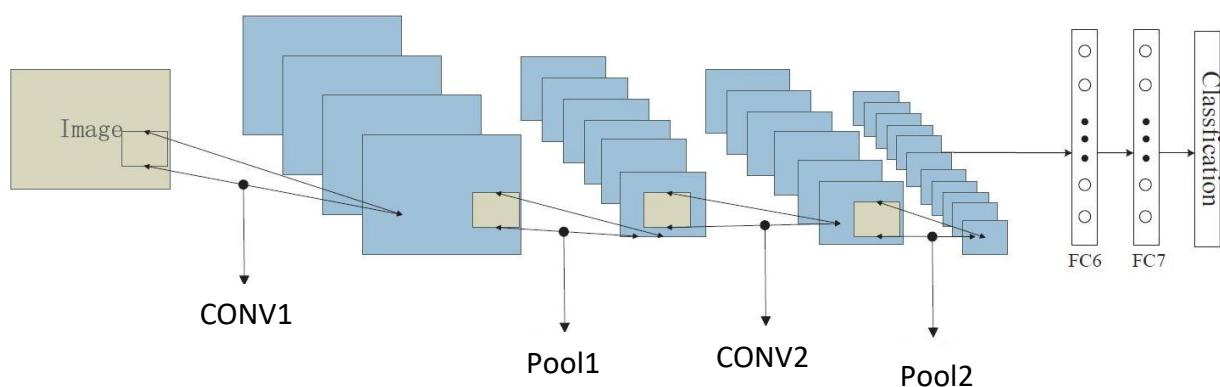


Figure 3.13: Flowchart of the main principal of the convolutional neural network [34]. This image represents the layers (convolution layer and pooling layer) of a CNN for the classification task.

At the *convolution layer*, an activation function determines the output of the neural network when the feature maps from previous layers are convolved with learnable kernels and are added with a trainable bias parameter. This process can be expressed as:

$$X_j^l = f(\sum_{i \in M_j} X_i^{l-1} * k_{ij}^l + b_j^l) \quad (3.3)$$

In which,  $X_i^{l-1}$  and  $k_{ij}^l$  are feature map and kernel respectively,  $b_j^l$  represents bias parameter,  $f(.)$  is the activation function and  $M_j$  shows a selection of the input maps [34, 35].

The activation function in the convolution layers has a significant effect on the training performance. Sigmoid, hyperbolic tangent, and rectified linear unit (ReLU) are three widely-used activation functions in CNN [35]. The activation function has to be selected based on the structure of the CNN. In this work, ReLU is applied as the activation function due to its better performance on the detection process of the marker in the captured-images than the other two functions.

The next layer in CNN is *Feature pooling layer* that aggregates the results of the convolutional layers and passes only the relevant and strong signals to the next layers. As it is shown in Figure 3.13, this layer selects the inputs from the small patches in the image where pooling window can have different sizes. In this project, maxPoolingLayer operation is applied in the pooling layer. Equation 3.4 represents the max pooling function where  $u(x,y)$  is a window function that can be applied to each input patch for computing a feature map [36].

$$a_j = \max_{N \times N} (a_i^{n \times n} u(n, n)) \quad (3.4)$$

The last layer in CNN is the *fully connected (FC) layer* that has a high-level neural network structure. Neurons in this layer are connected to the activations in the previous layer, and activations in this layer are computed via the matrix multiplication with a bias offset [37].



Training of all CNN layers is performed using the backpropagation algorithm to minimize the difference between the desired output and the actual output of the CNNs. Commonly, RCNN is considered as an outstanding method for the object detection process. This technique applies the CNNs and a support vector machine (SVM) as well as bounding boxes for object detection task. However, each training image should be cropped to a defined size based on the FC layers and repeatedly undergo CNN process which is time-consuming. Consequently, the Fast RCNN is introduced to address these issues. In this approach, a single stage training is performed via multi-task loss process that improves the accuracy and speed of the training. Moreover, with the use of Fast RCNN, the feature caching does not require disk storage as SVM approach. Alternatively, the Softmax layer is inserted directly into the network as a replacement for SVM. This technique exhibits significant improvements for finding reasonable parameters, but, it still is not enough powerful for real-time applications. Consequently, to improve the performance and speed in Fast RCNN, Faster RCNN approach is proposed. This model proposes regions using a deep fully convolutional network called Region Proposal Network (RPN) [34]. Figure 3.14 represents the configuration of the Faster RCNN.

In comparison with the mentioned frameworks, Faster RCNN (FRCNN) offers a higher accuracy for object detection task. Therefore, in this project, Faster RCNN is selected as the processing framework [34].

- Precision and recall analysis

Generally, there are two criteria in deep learning to evaluate the performance of the detector: average precision (AP) and recall. These parameters are defined as follows:

$$average - precision = \frac{True\ positive}{True\ positive + True\ negative} \quad (3.5)$$

$$recall = \frac{True\ positive}{True\ positive + False\ negative} \quad (3.6)$$

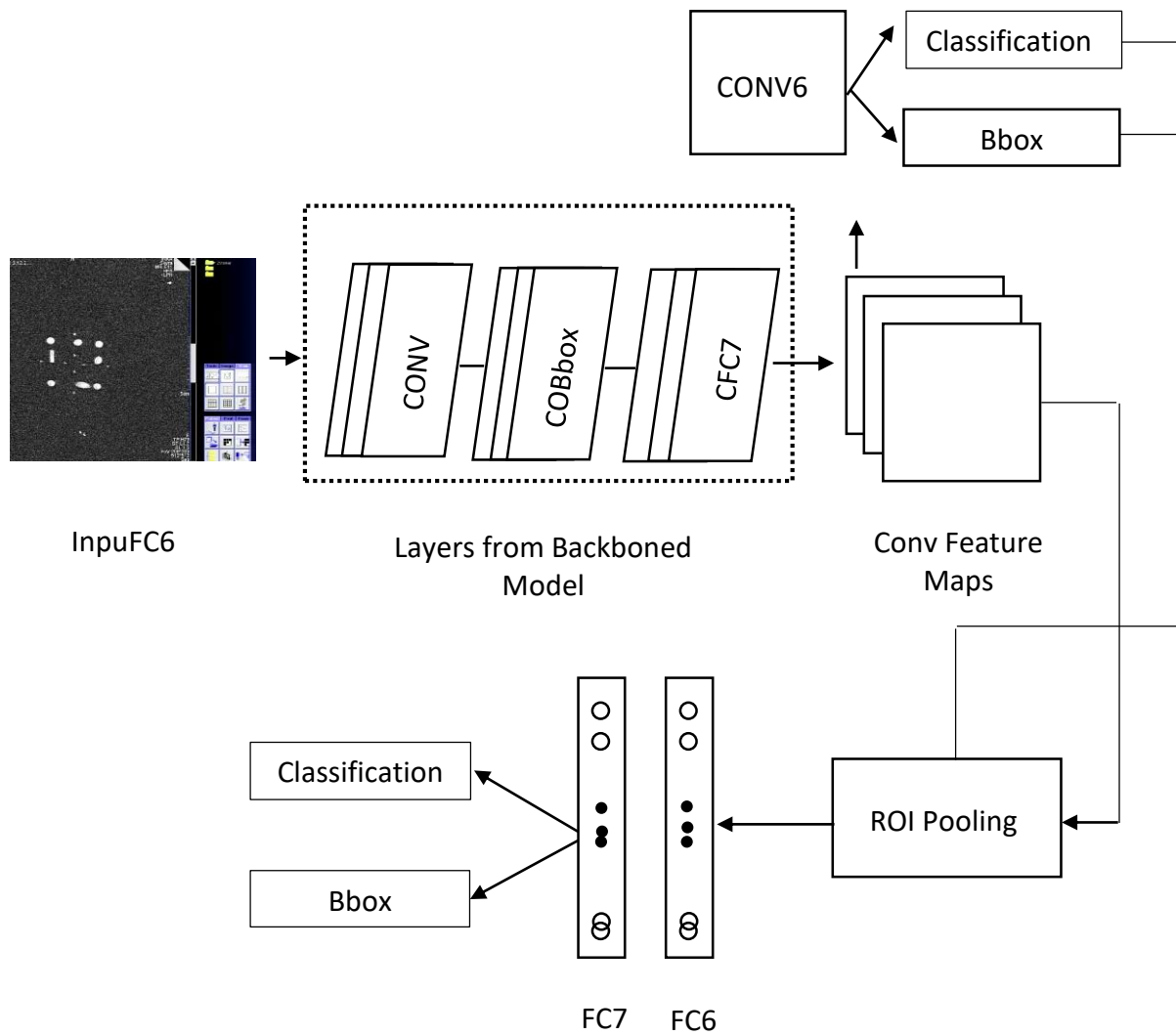


Figure 3.14: Flowchart of the Faster-region CNN approach. In this image, the required layers and the structures of the faster RCNN are represented which indicate the flow of data in the framework.

Where, “False negative” is a test result which wrongly indicates that a condition does not hold. “True negative” is a test result which correctly identifies that a condition does not hold. “True positive” is a result indicating that a given condition exists and it does exist [34, 38].



In this work, in order to evaluate the accuracy of the detector, the precision and recall rate of the detector is estimated on the test images. The average precision diagram of a detector trained with 88 images is shown in the Figure 3.15. Also, the Figure 3.16 represents the result of the automatic detection of the Z-frame marker employing the trained detector.

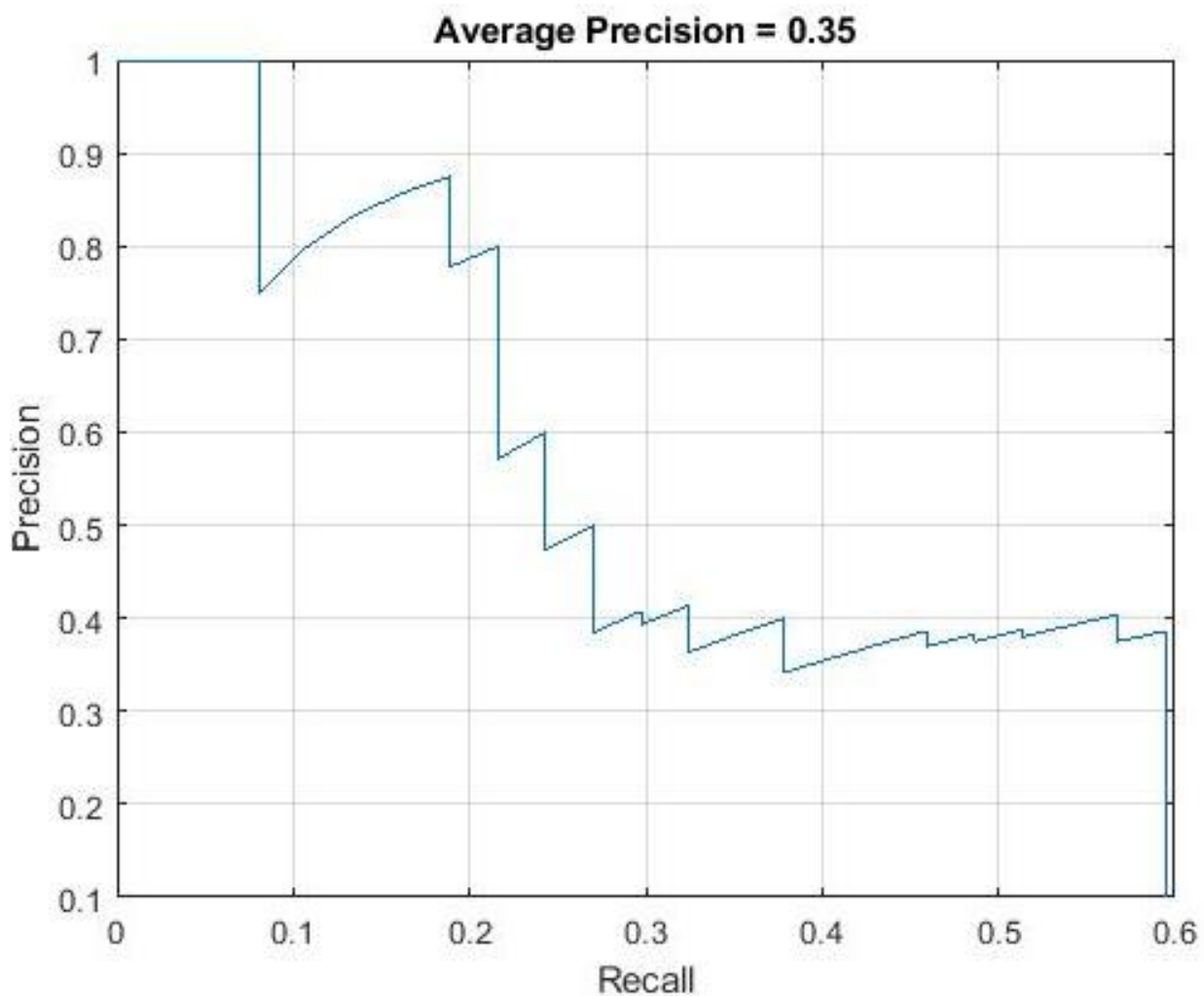


Figure 3.15: Precision and recall rate of the detector. The input data includes 88 images of the captured-MR images of the Z-frame, which 60 percent of the images are randomly selected for the training procedure and 40 percent for testing of the detector. The precision of the detector is 35 percent, which can be improved by adding more images to the dataset and increasing the layers of the convolutional network.

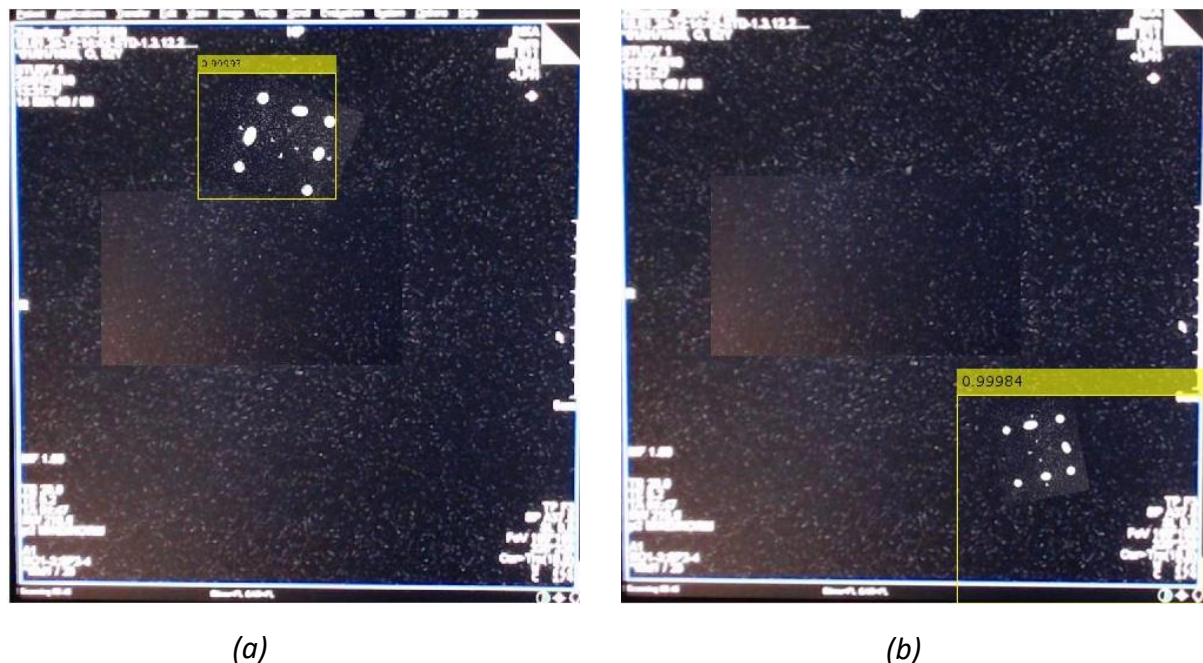


Figure 3.16: The detected Z-frame structures from an MR-captured image. (a) In this image, the Z-frame structures are detected correctly within the bounding box. (b) In this image, the bounding box is not positioned correctly and some other objects from the background are detected as the Z-frame structures.

### 3.2.2.3 Noise removal of the MR-images

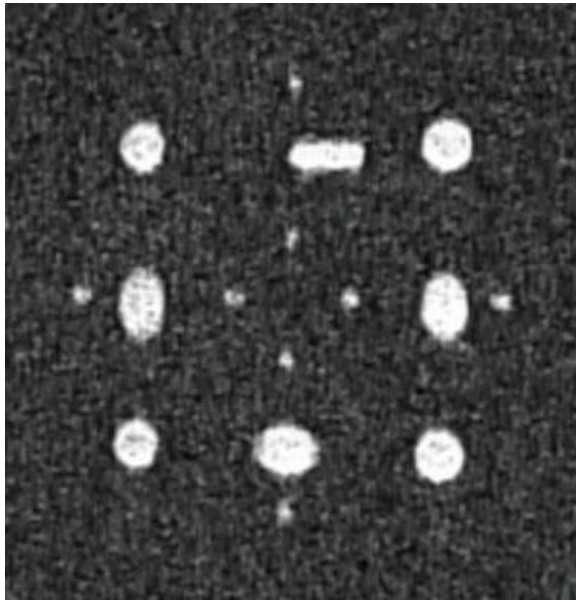
As it is explained in the literature survey (section 2.1), in magnetic resonance images, noise is commonly represented by the means of a Rician distribution, since it is assumed that a zero-mean uncorrelated Gaussian noise exists in both the real and imaginary parts of the k-space MR data. This noise affects the performance of the processing techniques applied on the MR-images, such as registration, segmentation, and localization [39]. During the noise removal process, a tradeoff between the noise reduction and the preservation of the relevant features in the image must be considered. Consequently, in this project, different noise removal methods have been investigated for the objective to assess their accuracy for suppressing the noise of the captured-MR images.

- Image denoising using Gaussian Smoothing Filter

The Gaussian filter is a type of the image-smoothing filter that reduces the noise by blurring the image. The Gaussian function that is defined in the equation 3.7, calculates a transformation for filtering the image based on the standard deviation  $\sigma$ , and the distances  $x$  and  $y$  of the points from the origin in the horizontal and vertical axes [40].

$$G(x, y) = \frac{1}{2\pi\sigma^2} e^{-\frac{x^2+y^2}{2\pi\sigma^2}} \quad (3.7)$$

The Gaussian smoothing filter based on the equation 3.7 is applied to the captured-MR images of the Z-frame to suppress the Gaussian distributed noise. Figure 3.17 shows the image before and after filtering operation.



(a)



(b)

Figure 3.17: (a) The T1W image of the Z-frame marker which is acquired using the capture device and the AV converter. (b) Image (a) after denoising using Gaussian smoothing operation.

- Image denoising using Wavelets

The nature characteristics of the wavelet transforms for preserving the edges in the image make this filter as one of the most applicable denoising technique. By applying the Discrete Wavelets Transform (DWT) to an image, the image is decomposed into a series of coefficients, such as: Scaling coefficients (approximation sub-band) and wavelet coefficients (detail sub-band) [41]. The DWT defines one coefficient for pixels with low SNR value (noise), and another coefficient for the pixels with the high SNR value (signal information). Therefore, the DWT noise reduction algorithm removes low SNR coefficients and keep the prominent ones, where the Inverse Discrete Wavelet Transform (IDWT) provides the denoised image [42, 43]. The core task of the wavelet denoising method is selecting a suitable threshold for wavelet coefficients which preserves the features of interest in the image while suppressing the noise.

One practical technique to find the most suitable threshold for denoising the MR-images has been proposed by Donoho [44]. In this method, the global threshold is estimated according to the equation 3.8, where  $N$  is the number of the wavelet coefficients and  $\sigma$  is the standard deviation [44].

$$\lambda = \sigma \sqrt{2 \log N} \quad (3.8)$$

In the next step, Hard or Soft thresholding technique is used to apply the computed optimal threshold from the equation 3.8 to the wavelet coefficients. The mathematical definition of both methods are given in the Equations 3.9 and 3.10 where  $c$  is the coefficient array [44].

$$\overline{c}_h(k) = \begin{cases} \text{sign}(c(k))(|c(k)|) & \text{if } |c(k)| > \lambda \\ 0 & \text{if } |c(k)| \leq \lambda \end{cases} \quad (3.9)$$

$$\overline{c}_s(k) = \begin{cases} \text{sign}(c(k))(|c(k)| - \lambda) & \text{if } |c(k)| > \lambda \\ 0 & \text{if } |c(k)| \leq \lambda \end{cases} \quad (3.10)$$

The proposed thresholding methods discard the coefficients which have a smaller value than the threshold and keep the rest ones. However, the soft thresholding has a stronger mathematical function which does not make discontinuities at  $|c(k)| = \pm\lambda$  [44].

Figure 3.18 shows a captured-MR image before noise removal and after filtering by the proposed method of the wavelet denoising.

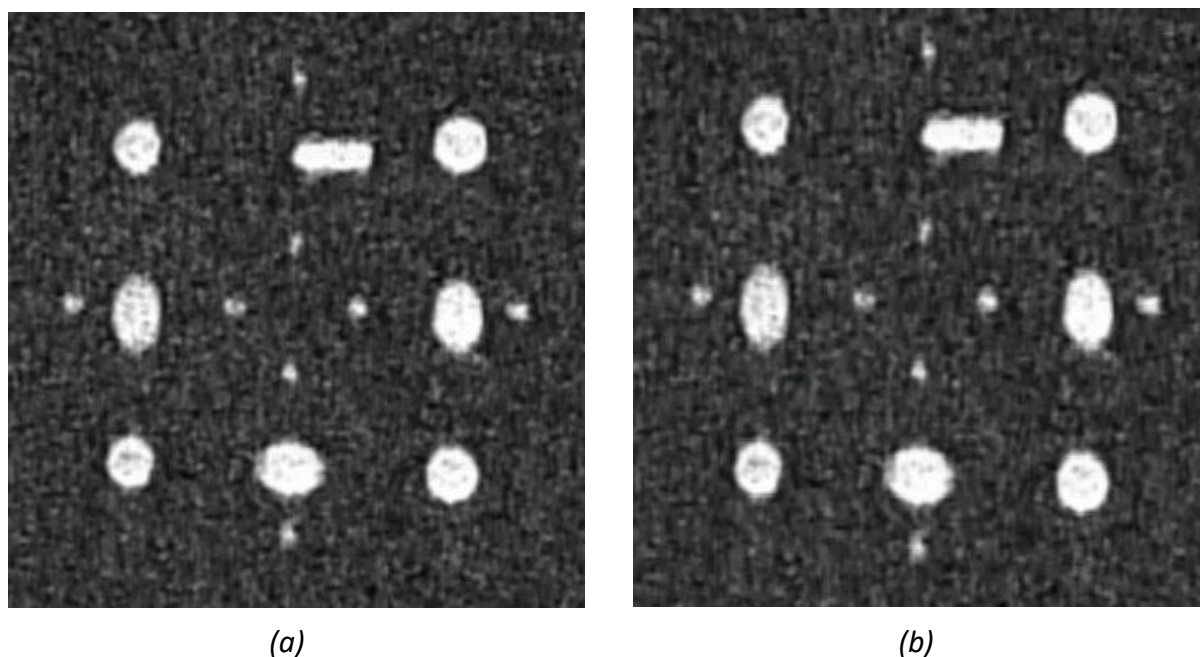


*Figure 3.18: (a) This image represents the original captured-MR image (T1W) from the Z-frame marker without denoising. (b) This image shows the filtered image using wavelet and soft thresholding method.*

- **Image denoising using Nonlinear Anisotropic Filtering**

The main drawback of the proposed linear filtering methods is that the details in the original image will be destroyed during reducing the noise [45]. Anisotropic diffusion filtering proposed by Perona and Malic [46] is a method which reduces the image noise while preserves important details such as edges in the image. This filter is defined as an anisotropic process which employs an adapted diffusion tensor for smoothing the images. Importantly,

the inhomogeneous diffusive procedure limits the smoothing in the areas of interest which have a large likelihood to be edges or boundaries [46].

The performance of the Perona-Malik filter is based on the mathematical formulation given in the equation 3.11, where the rate of the diffusion can be controlled with the diffusion coefficient  $c(x,y,t)$  [46].

$$\frac{\partial}{\partial t} I(x, y, t) = \text{div}(c(x, y, t) \nabla I(x, y, t)) \quad (3.11)$$

Furthermore,  $I(x, y, t)$  represents the image intensity,  $\text{div}$  and  $\nabla$  denote the divergence and the gradient operators respectively. Moreover,  $x$  and  $y$  represent the spatial coordinates in the two-dimensional image, and  $t$  corresponds to the iteration number.

An important step in this technique is the estimation of an appropriate diffusion coefficient according to the image gradient. Ideally, the coefficient should be 0 at the features of interest (edges and boundaries), and 1 at the interior of a region. Accordingly, Perona and Malik introduced two mathematical equations (3.12 and 3.13) for estimating the diffusion coefficient, where the first equation has a better performance on the high contrast edges, and the second one is more suitable for the wide areas rather than the narrow ones [46].

$$c_1(x, y, t) = \exp\left(-\left(\frac{|\nabla I(x, y, t)|}{k}\right)^2\right) \quad (3.12)$$

$$c_2(x, y, t) = \frac{1}{1 + \left(\frac{|\nabla I(x, y, t)|}{k}\right)^2} \quad (3.13)$$

In the Equations 3.12 and 3.13,  $k$  is the conductance parameter, which determines the difference between an edge and an intensity value which is destroyed by noise [46]. Usually it can be selected empirically.

In addition, the diffusive procedure that applies the equation 3.11 defines the intensity change in each iteration based on the summation of the contributed pixels at the neighborhoods of (x,y) which are weighted according to the equation 3.14. The result of the procedure is presented in the equation 3.15 [46].

$$\begin{aligned}
 \Phi_E(x, y, t) &= c \left( x + \frac{dx}{2}, y, t \right) [I(x + dx, y, t) - I(x, y, t)] \\
 \Phi_W(x, y, t) &= c \left( x - \frac{dx}{2}, y, t \right) [I(x, y, t) - I(x - dx, y, t)] \\
 \Phi_N(x, y, t) &= c \left( x, y + \frac{dy}{2}, t \right) [I(x, y + dy, t) - I(x, y, t)] \\
 \Phi_S(x, y, t) &= c \left( x, y - \frac{dy}{2}, t \right) [I(x, y, t) - I(x, y - dy, t)] \quad (3.14)
 \end{aligned}$$

$$I(x, y, t + dt) = I(x, y, t) + dt \left[ \frac{1}{dx^2} [\Phi_E(x, y, t) - \Phi_W(x, y, t)] + \frac{1}{dy^2} [\Phi_N(x, y, t) - \Phi_S(x, y, t)] \right] \quad (3.15)$$

In the equations 3.14 and 3.15, the pixel spacing in the image is represented by dx and dy. Furthermore, in the equation 3.15, dt corresponds to the integration constant and it has to be selected with respect to a stability criterion [46, 47].

Figure 3.19 illustrates the performance of the anisotropic filter on a captured-MR image of the Z-frame marker.

In conclusion, according to the results from the performance of the three mentioned filtering methods, the anisotropic diffusion approach has an acceptable performance on the captured-images for the preprocessing step (noise reduction and the edge enhancement). Moreover, due to the mentioned characteristics of the anisotropic diffusion, the processed image converges faster to the desired shape for the further processing.

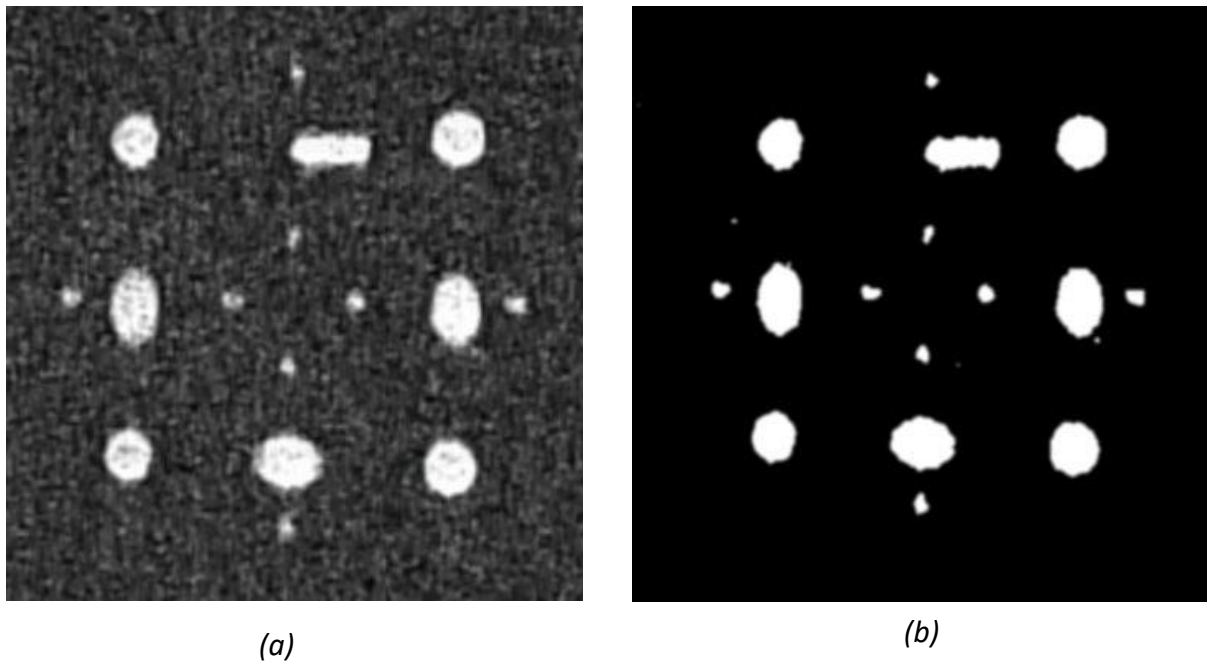


Figure 3.19: (a) The captured-MR image (T1W) from the Z-frame marker without denoising. (b) The denoised image using the anisotropic filter after binarization. The equation 3.12 was employed for the estimation of the diffusive coefficient.

#### 3.2.2.4 Image contrast enhancement

In order to adjust the intensity value in the denoised images, the *imadjust* function in Matlab is implemented. The range of the input and output values of the function are specified in two vectors. The first vector specifies the low- and high-intensity values that must be mapped, and the second vector specifies the scale over which the values of the first vector should be mapped to [48]. The result of this processing step is represented in the Figure 3.20.



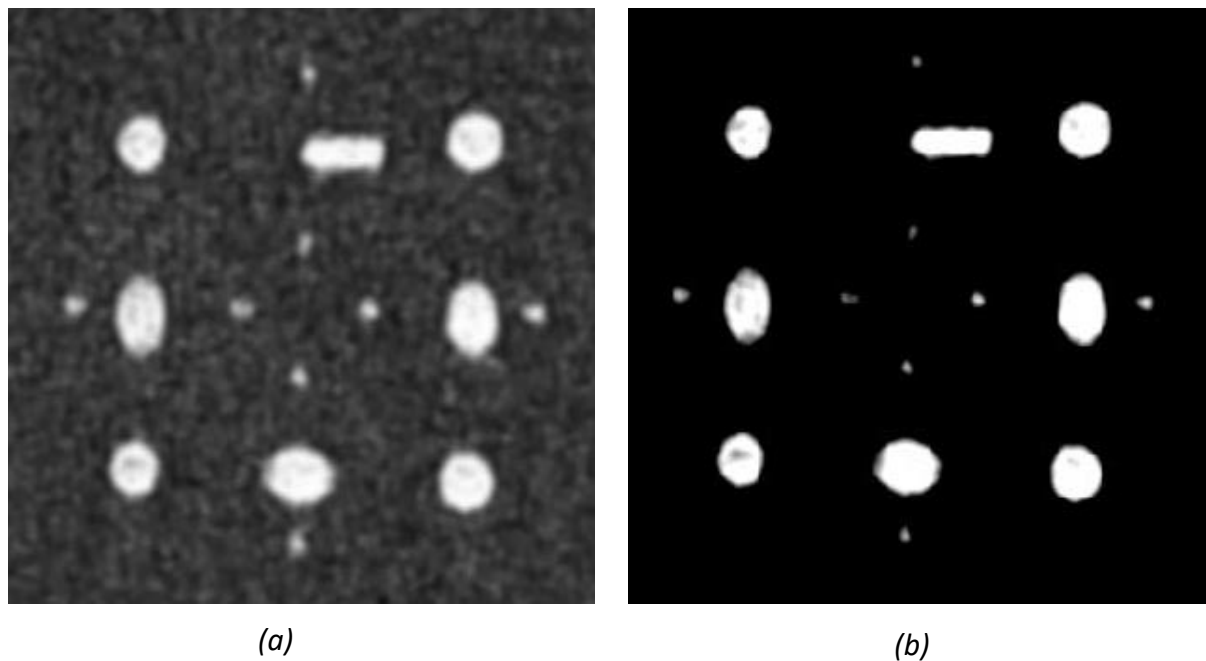


Figure 3.20: (a) The denoised captured-MR image using Gaussian smoothing filter. (b) The Image (a) after the contrast enhancement procedure.

### 3.2.2.5 Image binarization

Thresholding is a common image processing technique applied to the gray-scale images for the image binarization. In general, it makes a binary partition of the image data set by using the intensity values of the image pixels [49]. A single-threshold method separates the dataset into two classes based on a threshold, where pixels with the higher intensities than the threshold are categorized into one class and the other pixels are categorized in an another class. The mathematical formulation of this technique is presented in equation 3.16, where  $I$  and  $\lambda$  correspond to the analyzed intensity value and the threshold, respectively [50].

$$I = \begin{cases} 0 & \text{if } I \leq \lambda \\ 1 & \text{if } I > \lambda \end{cases} \quad (3.16)$$

The threshold value has to be determined in a way that can differentiate the regions of interest [50]. In this project, in order to distinguish between the cylindrical fiducials and the other structures in the image, the user can select a threshold based on the visual inspection of the image. Therefore, any pixel for which is bigger than a threshold labeled 1 and corresponds to the fiducial maker; otherwise, the pixel corresponds to the background and labeled 0. Figure 3.21 illustrates the captured-MR image after binarization.

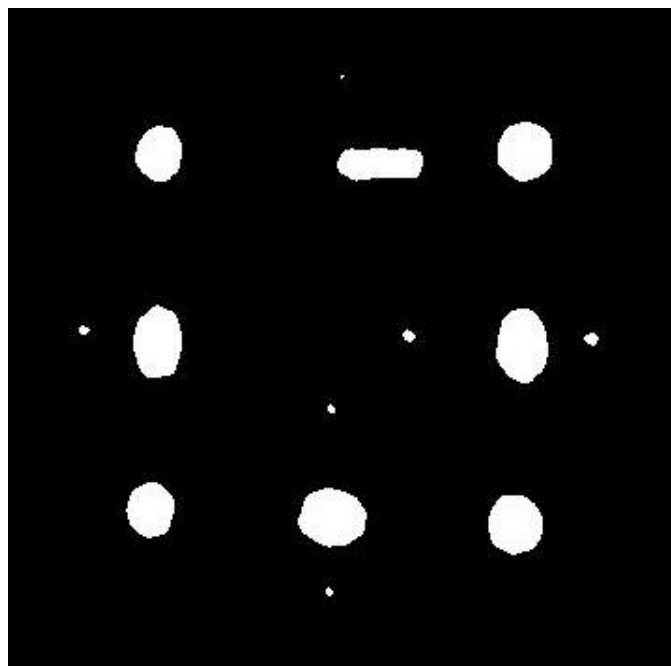


*Figure 3.21: The binarized image of the captured-MR image after denoising by the Gaussian filter and contrast enhancement.*

### 3.2.2.6 Binary image mask

At this stage, each segment which is detected as a fiducial marker, is examined based on its volume and dimension. If the volume in a given segment is lower than a pre-defined range, it does not belong to the Z-frame structures, and has to be removed from the image. Therefore,

function *bwareaopen* in Matlab is used to create a binary mask and remove small segments from the image as it is shown in the Figure 3.22 (a).

Furthermore, the Z-frame with the z-axis indication triangle (section 3.1) requires a filtering method to remove the triangle which has a size bigger than the 7 fiducial markers. For this purpose, a polygonal region of interest (ROI) mask is implemented which creates an interactive polygon tools for selecting a ROI. The mask sets the pixels' values inside the ROI to 0 and the value of the other pixels to 1. Figure 3.22 (b) illustrates the interactive tool for selecting and adjusting polygon vertices on the image.

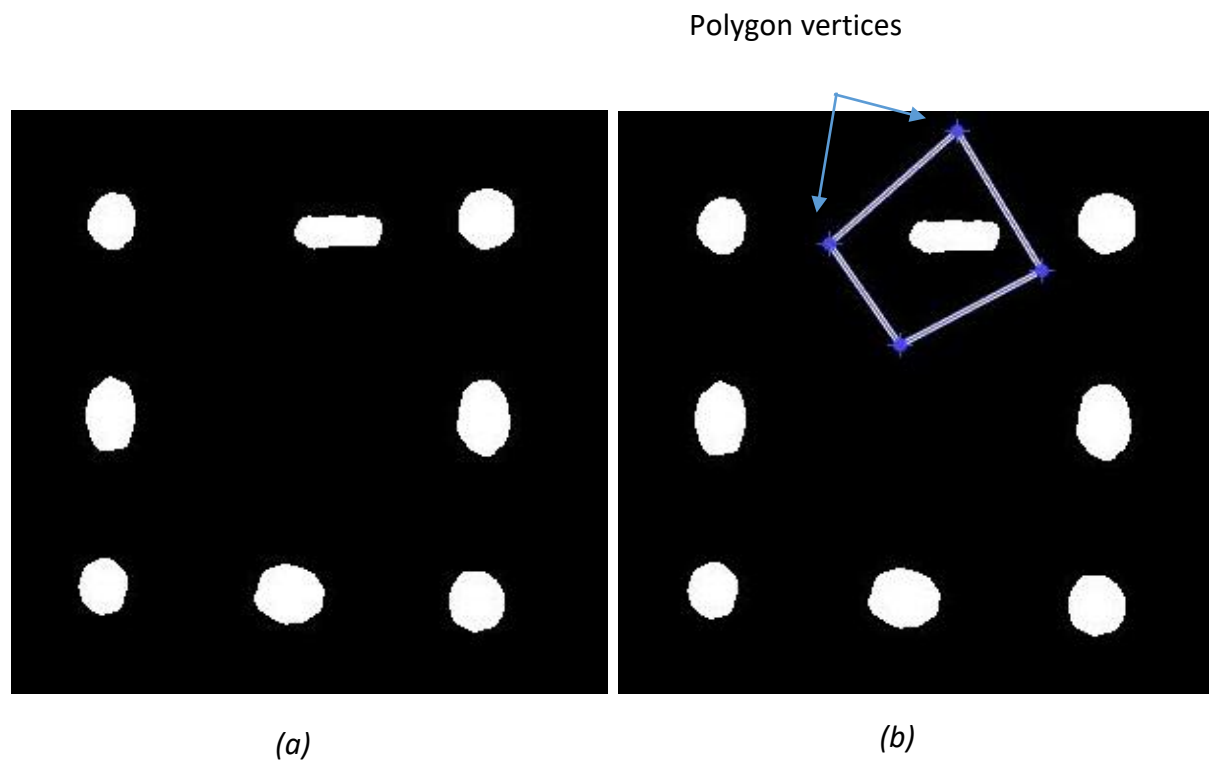


*Figure 3.22: (a) The image shows the result of the first masking method using a threshold to withdraw small objects from the background. (b) The image represents the polygonal masking technique to remove the triangle structure from the image.*

### 3.2.3 Localization and registration

#### 3.2.3.1 Center detection of the fiducial ellipses

Once all 7 ellipses with the size close to the physical size of the marker were detected, the function *regionprops* in Matlab is used to calculate the center point of each fiducial marker. The result is a  $7 \times 2$  matrix where the first column represents x coordinates and the second column corresponds to the y coordinates of the center of the fiducial mass region [51]. Hence, the resulting 7 centroids of the ellipses are sorted along the U-shape of the marker as illustrated in Figure 3.23. Depending on the attachment of the Z-frame on the robotic device, the frame can have a different position, scale, and orientation in the MR-images. Therefore, the centroids are not always detected in the same way. Accordingly, a robust technique is required to rotate the Z-frame around its axis on the image.

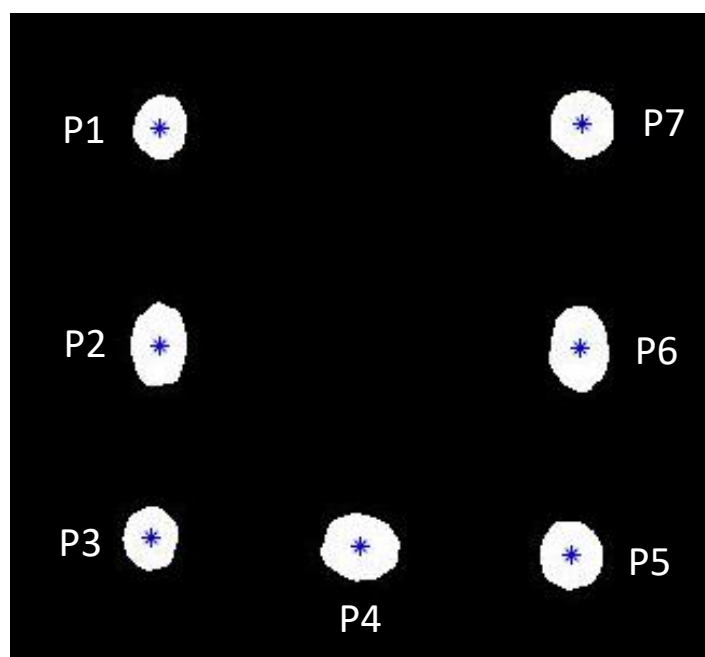


*Figure 3.23: This image illustrates the binary image of the Z-frame marker and its detected centroids of the seven fiducial markers. The accurate position of the centroids depends on the pre-processing stage for preserving more relevant signal and suppressing more noise.*

### 3.2.3.2 Image rotation estimation using automated feature matching

Feature matching method, automatically determines a geometric transformation between two images that are different by a rotation or a scale change. Importantly, the features in the both images must be detected with an optimal feature detection technique which is robust to rotation, scale, illumination, and noise of the images. Scale Invariant Feature Transform (SIFT) is a feature detector proposed by Lowe [52]. SIFT is an efficient detector in the object recognition applications that is invariant of the rotation, intensity and viewpoint changes in the image. However, the main drawback of SIFT is the time-consuming feature computation procedure. Alternatively, Speed up Robust Feature (SURF) technique, with the same principle of SIFT, has a higher computational speed without reducing the quality of the detected features. Once, the image features and descriptors are detected, the corresponding features in each image will be matched based on the feature similarities. Therefore, a transformation matrix based on the matching point pairs and using the statistically robust M-estimator SAmple Consensus (MSAC) algorithm is computed. Matching point pairs employed in the estimation of the transformation matrix for the Z-frame marker fiducials is displayed in the Figure 3.24 (c). Subsequently, the desired angle of the rotation is calculated using the geometric transform from the last step. The recovered image is shown in Figure 3.24 (d) [53].

This technique requires the detected features be highly distinctive to be correctly matched with high probability. In this project, both SIFT and SURF feature extraction methods are implemented. However, the different fiducial markers shape in different imaging slices, as well as, artifacts and noises in MRI unable the algorithm to find the match features properly. Figure 3.25 illustrates an unsuccessful matching model of the point pairs in two different cross-sectional images of the Z-frame.

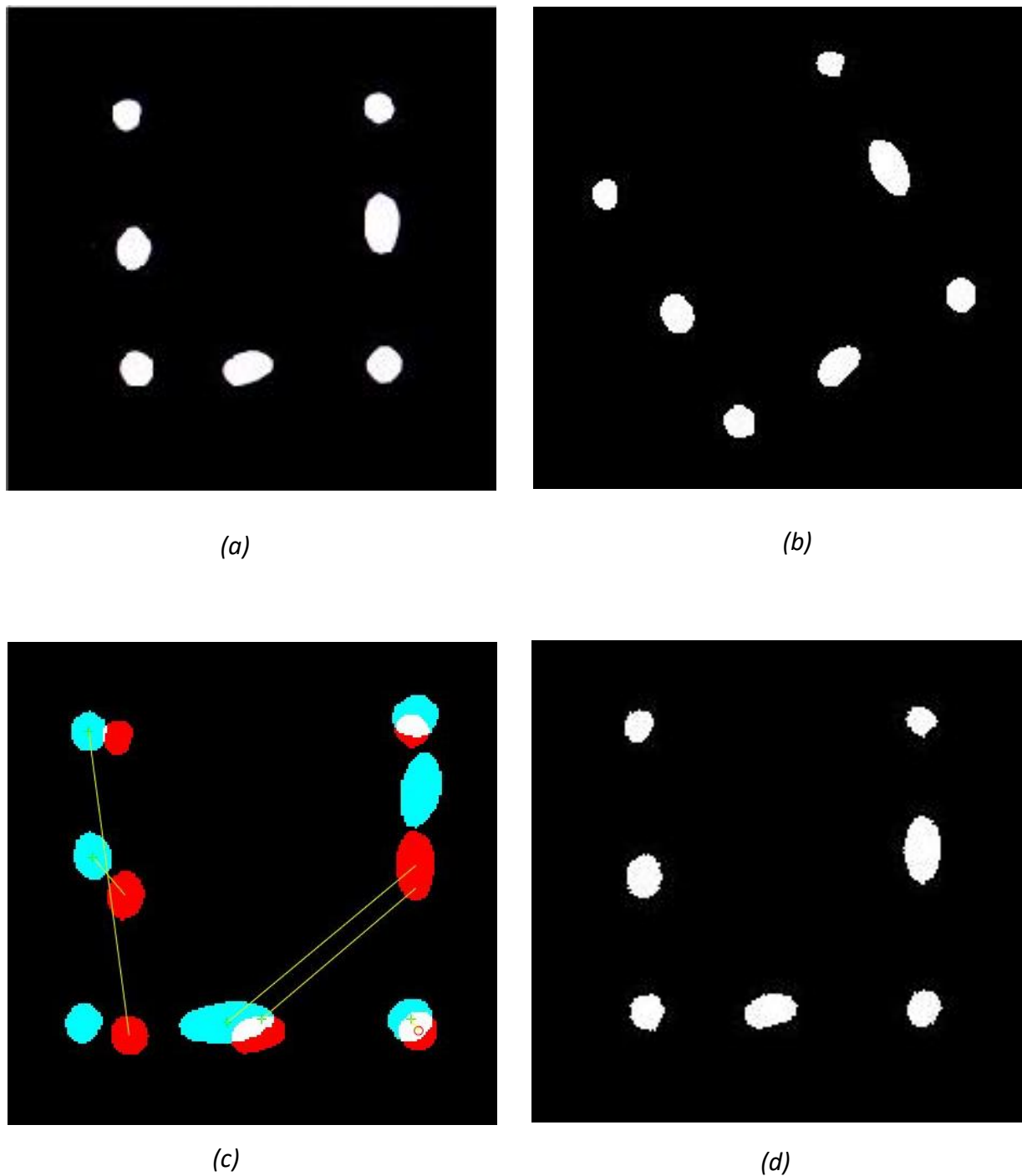
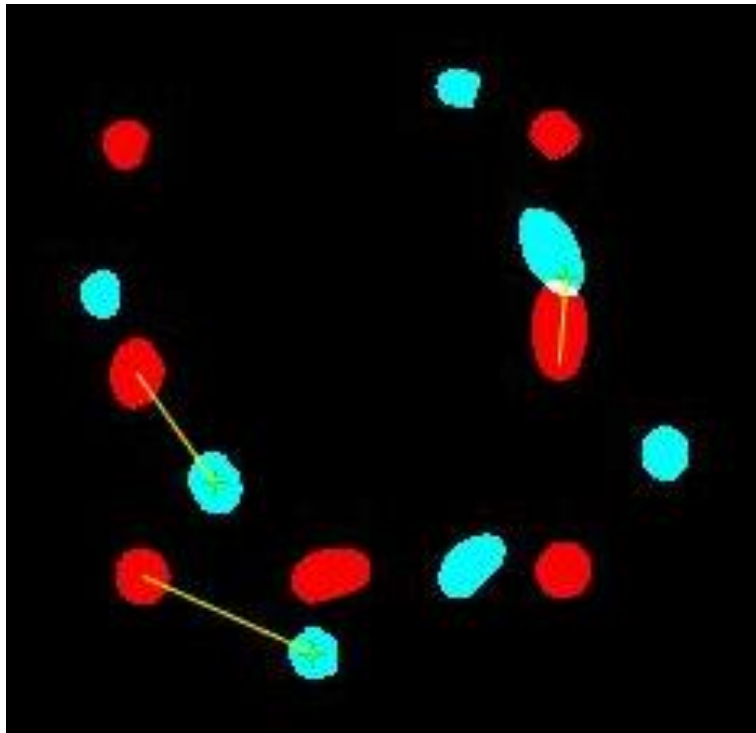


Figure 3.24: (a) Captured-MR image of the Z-frame marker (without rotation, this image is used as a reference). (b) A rotated Z-frame marker in the image, therefore the fiducials are not positioned along the U-shape of the marker. (c) Matching point pairs used in the estimation of the transformation matrix of the ellipses from the rotated image (blue ones) and the reference images (red ones). (d) The recovered image (b) after rotation.



*Figure 3.25: Unsuccessful matching model of the point pairs in two different cross-sectional images of the Z-frame. (The red ellipses belong to the reference image and the blue ones belong to the rotated image)*

### 3.2.3.3 Image rotation using centroids coordinate system

In this technique, the coordinates of the center points of the fiducial markers are employed to compute a rotation matrix that rotates the points in the image coordinate system. Since the four outer points of the Z-frame has a constant distance in relation to each other, the points with maxim Euclidean distances to its three neighbors are detected as the outer points. Once all four outer points are detected, the correct position of them has to be determined in the Z-frame. The point with the minimum x coordinate is detected as the P1 and the one with the maximum x coordinate is determined as P7, also the y coordinates of the detected points must be compared for an accurate estimation of the P1 and P7. Totally, four different rotation models of the Z-frame are possible, which the automated algorithm must select the correct

one and rotate the marker according to the points configuration. Figure 3.26 illustrates four possible rotation models of the Z-frame marker in the image.

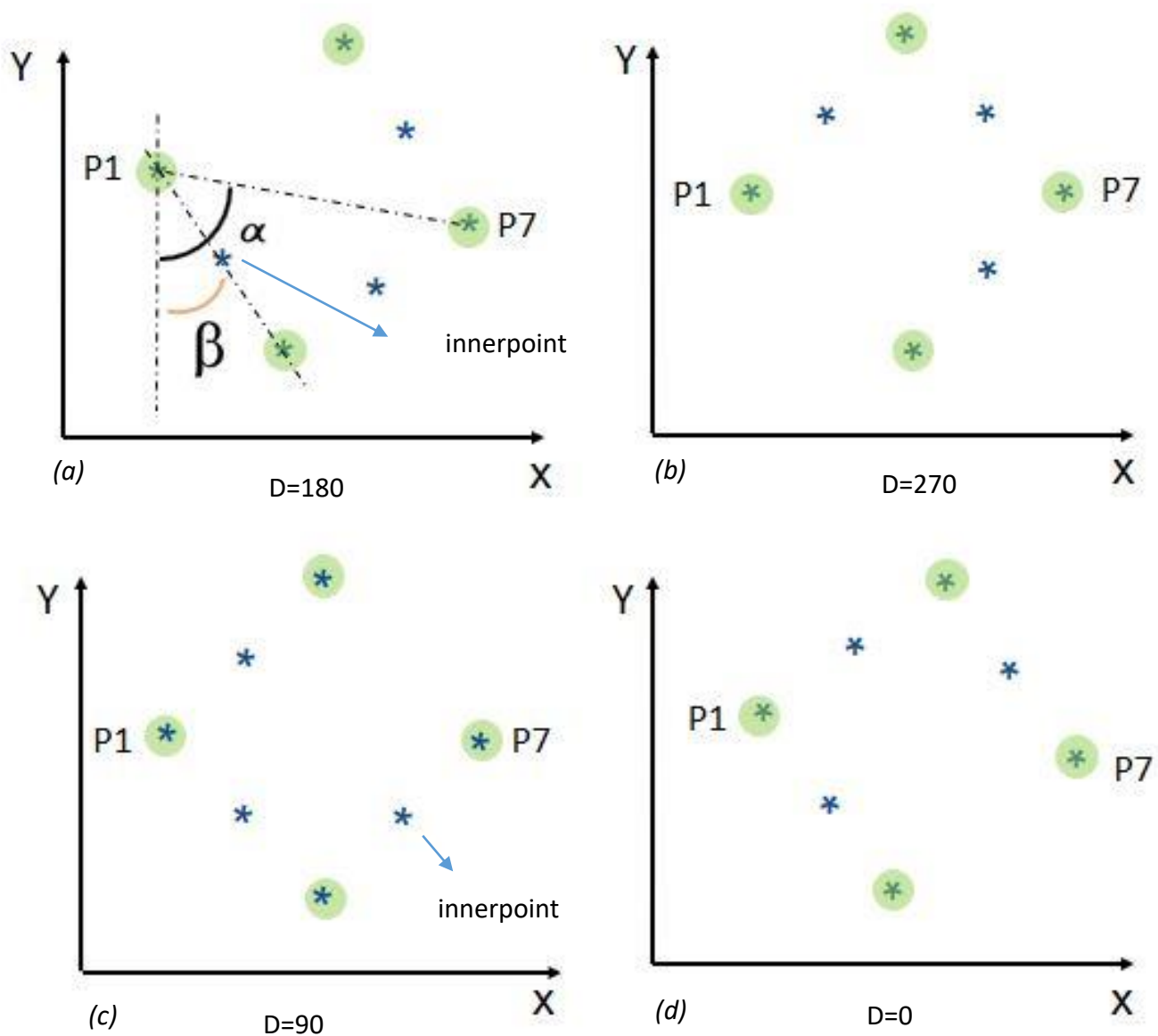


Figure 3.26: Four different possible rotation of the Z-frame marker. Each model has a different rotation equation.



In the next step, the algorithm detects the nearest neighbor points for the P1. If there is only one neighbor for the P1, the Z-frame has one of the shape model in the Figure 3.26 (a) and 3.26 (b), and if there are two neighbors the shape models in Figure 3.26 (c) and 3.26 (d) are possible. Then, the algorithm must detect a point called *innerpoint*, which is located between P1 (or P7) and the point with a minimum y coordinate, as it is shown in Figure 3.26 (a) and (c). The rotation angle  $\theta$  is defined in the equation 3.17.

$$\begin{aligned}\theta &= \beta + D , \\ \beta &= \alpha - 45^\circ\end{aligned}\tag{3.17}$$

Where  $\alpha$  is the angle between the line that passes through P1 and P7, and the y axis, D corresponds to the defined angle for each model. Therefore, a rotation matrix is calculated which must be multiplied with the centroids matrix. The ordered coordinates of the Z-frame fiducials are then applied to the next procedures.

### 3.2.3.4 Distance calculation and calibration

In the calibration part, a coefficient has to be calculated to transfer the points from the image coordinate system (pixel) to the frame coordinate system (millimeter). In DICOM images, pixel spacing is defined as the physical distance (mm) between the centers of each pixel. However, in the captured-images, the resolution of the MRI monitor and the capture device should be considered for the calculation of the pixel spacing of the images. Therefore, the pixel spacing consists of two coefficients: vertical spacing and horizontal spacing. These coefficients are defined in the equations 3.18 and 3.19, where,  $\mu_x$  is the row spacing or vertical spacing in mm that must be multiplied with the x coordinates of the fiducial markers,  $\mu_y$  is the column spacing or horizontal spacing in mm and must be multiplied with the y coordinates of the fiducial markers.  $P_i$  is the ordered set of center points of the fiducial markers, d is the

Euclidean distance between points and  $d'$  is the distance between points in physical space (e.g. 40 mm).

$$\mu x = (|d'/d (P5, P3)| + |d'/d (P1, P7)|)/2 \quad (3.18)$$

$$\mu y = (|d'/d (P3, P1)| + |d'/d (P5, P7)|)/2 \quad (3.19)$$

The next step of the calibration process is the transformation of the centroids coordinate systems to the center of the Z-frame as it is shown in Figure 3.27. The transferred set of points then are applied for the marker alignment calculation.

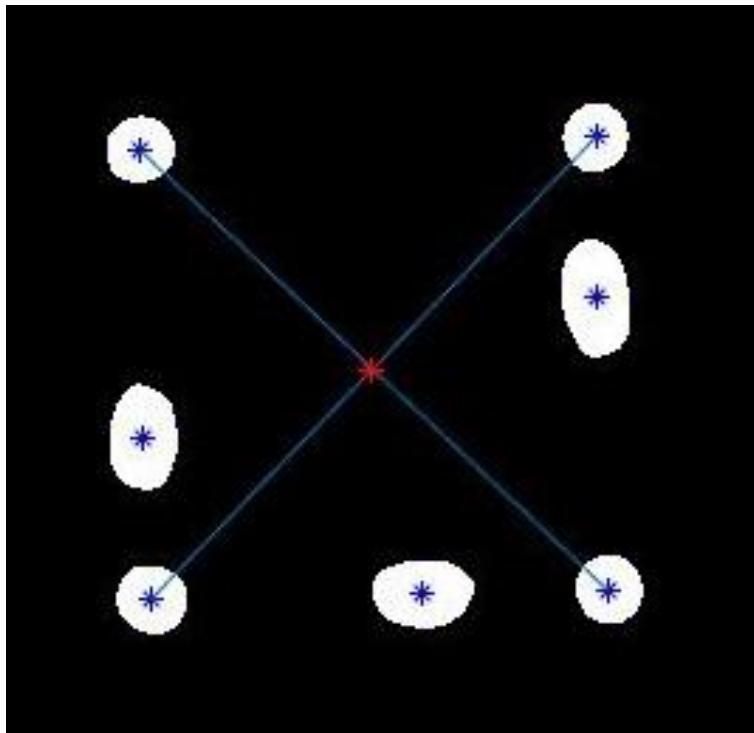


*Figure 3.27: The computed center of the Z-frame marker (red star). The coordinate systems of the detected centroids (blue stars) are then transferred to the center of the marker.*

### 3.2.3.5 Marker alignment calculation

Once the center of all 7 fiducials are calculated and calibrated within the MRI space, the position of the three corresponding points (P1, P4, P6) in the marker coordinate system is estimated according to the equations 3.20 and 3.21. Where  $f_i$  is a function that measures the fraction along the length of the frame at which each diagonal cylinder is imaged, and  $p_{iMR}$  is the centroid of the ellipse  $i$  identified in the MR image [3].

$$[p_{2f} \ p_{4f} \ p_{6f}] = \begin{bmatrix} l_x \left\{ -\frac{1}{2} & \frac{1}{2} - f_4 & \frac{1}{2} \right\} \\ l_y \left\{ \frac{1}{2} - f_2 & \frac{1}{2} & -\frac{1}{2} + f_6 \right\} \\ l_z \left\{ -\frac{1}{2} + f_2 & -\frac{1}{2} + f_4 & -\frac{1}{2} + f_6 \right\} \end{bmatrix} \quad (3.20)$$

$$f_i = \frac{|p_{(i+1)MR} - p_{iMR}|}{|p_{(i+1)MR} - p_{(i-1)MR}|} \quad (3.21)$$

### 3.2.3.6 Angle calculation of the MR-image plane and the Z-frame marker

In this stage, the angle between the MR-image plane and the Z-frame marker is calculated to identify the alignment of the marker which confirm the parallelization of the marker to the image plane. When the MRI plane and the Z-frame marker plane intersect, an angle between them is formed that can be calculated by the use of the normal vectors of the given planes according to the equation 3.22. The equations of two intersecting planes and their normal vectors are given in Equations 3.23 and 3.24 [54]:

$$\cos \alpha = \frac{|\vec{n}_1 \cdot \vec{n}_2|}{\vec{n}_1 \vec{n}_2} \quad (3.22)$$

$$\begin{aligned}\Pi_1: a_1x + b_1y + c_1z + d_1 &= 0 \\ \Pi_2: a_2x + b_2y + c_2z + d_2 &= 0\end{aligned}\quad (3.23)$$

$$\begin{aligned}\vec{n}_1 &= \text{normal vector to plane } \Pi_1 = (a_1, b_1, c_1) \\ \vec{n}_2 &= \text{normal vector to plane } \Pi_2 = (a_2, b_2, c_2)\end{aligned}\quad (3.24)$$

Therefore, the rotation angle of the Z-frame around the x- and y-axis are calculated using the normal vector of the plane containing three corresponding points P2, P4, and P6 in the Z-frame coordinate system as it is shown in Figure 3.28.

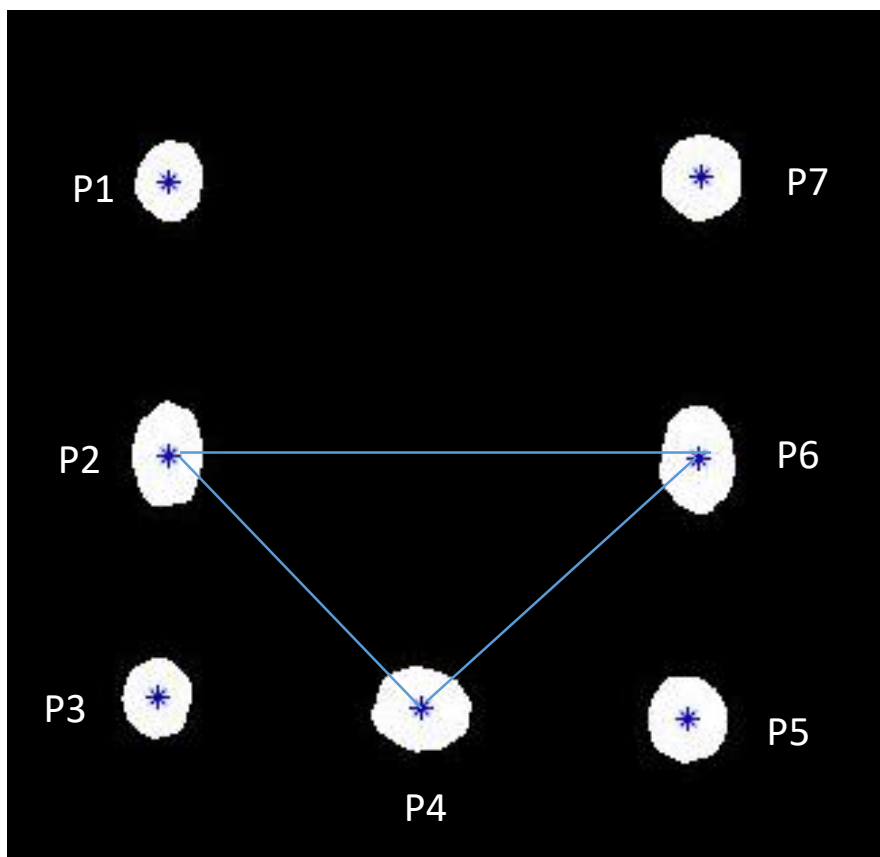
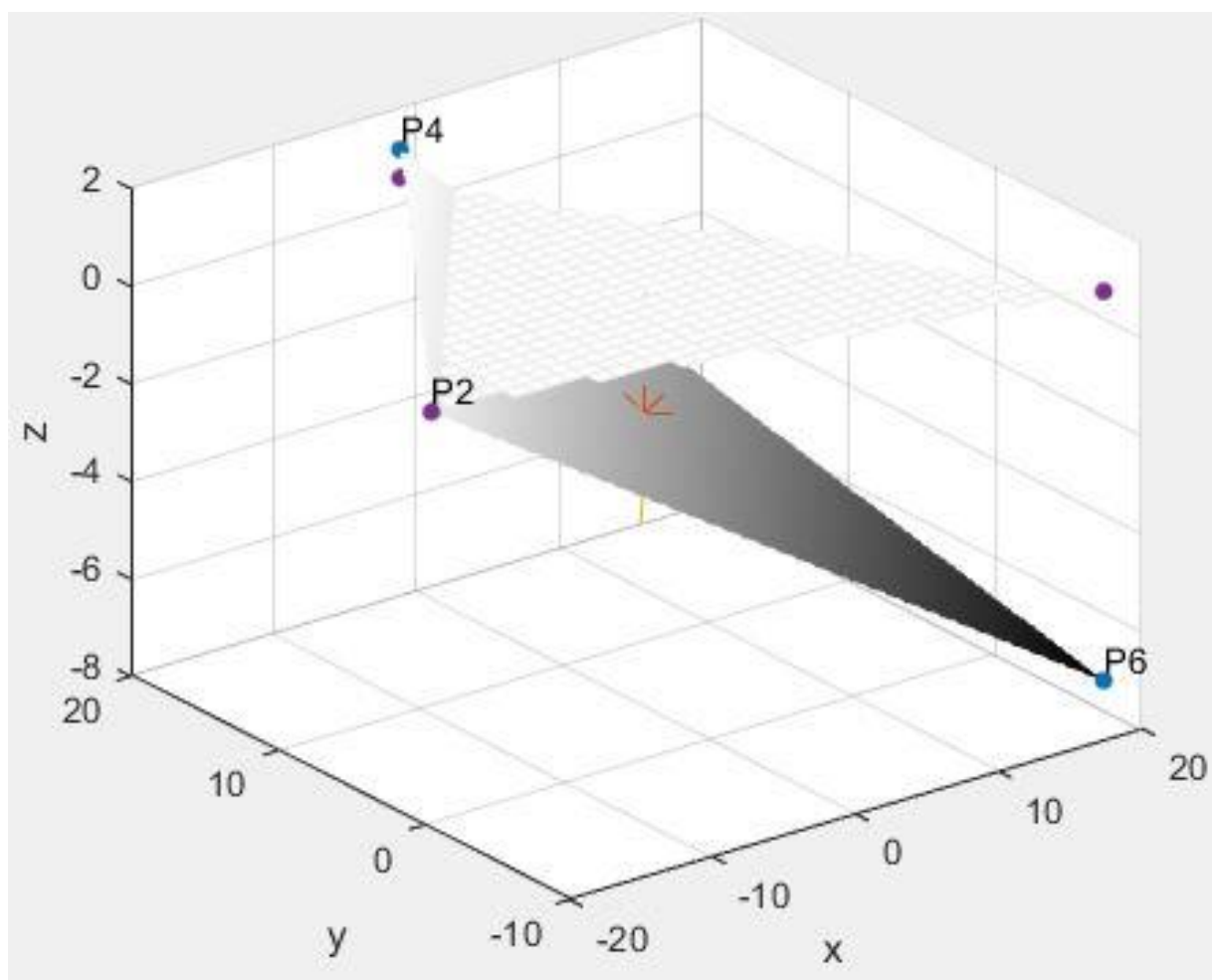


Figure 3.28: The three corresponding points (P2, P4, and P6) make a plane which is used to calculate the angle between the MR-plane and the Z-frame.

The angle between the Z-frame marker plane and yz-plane determines the rotation around x-axis, and the angle between the Z-frame marker plane and the xz-plane ascertains the rotation around y-axis. In the Figure 3.29, the gray plane is the Z-frame marker plane including P2, P4 and P6 coordinates which is rotated +10 degrees around both x- and y-axes. The white plane is the optimal plane that the Z-frame marker should reach after -10 degrees' rotation of the MRI plane or Z-frame around both x- and y-axes.



*Figure 3.29: The Z-frame plane including the coordinates of the P2, P4 and P6 fiducial points. The plane is plotted after processing of the captured MR-image and extracting and computing the centroids of the fiducial markers. The Z-frame is rotated -10 degrees around both the x and y-axes.*

In the 2D coronal view of the Z-frame in the MRI coordinate system (The cross-section view of the marker inside the MR-image depends on the initial orientation of the Z-frame in the setup), the sagittal plane represents the y-axis and the transversal plane indicates the x-axis. Accordingly, the clinician should rotate the MRI plane -10 degrees both around x -and y-axes to make the Z-marker parallel to the MRI plane. As it is shown in the Figure 3.30, the marker plane (gray plane) is close to the optimal plane (grid plane) after the MRI plane rotation.

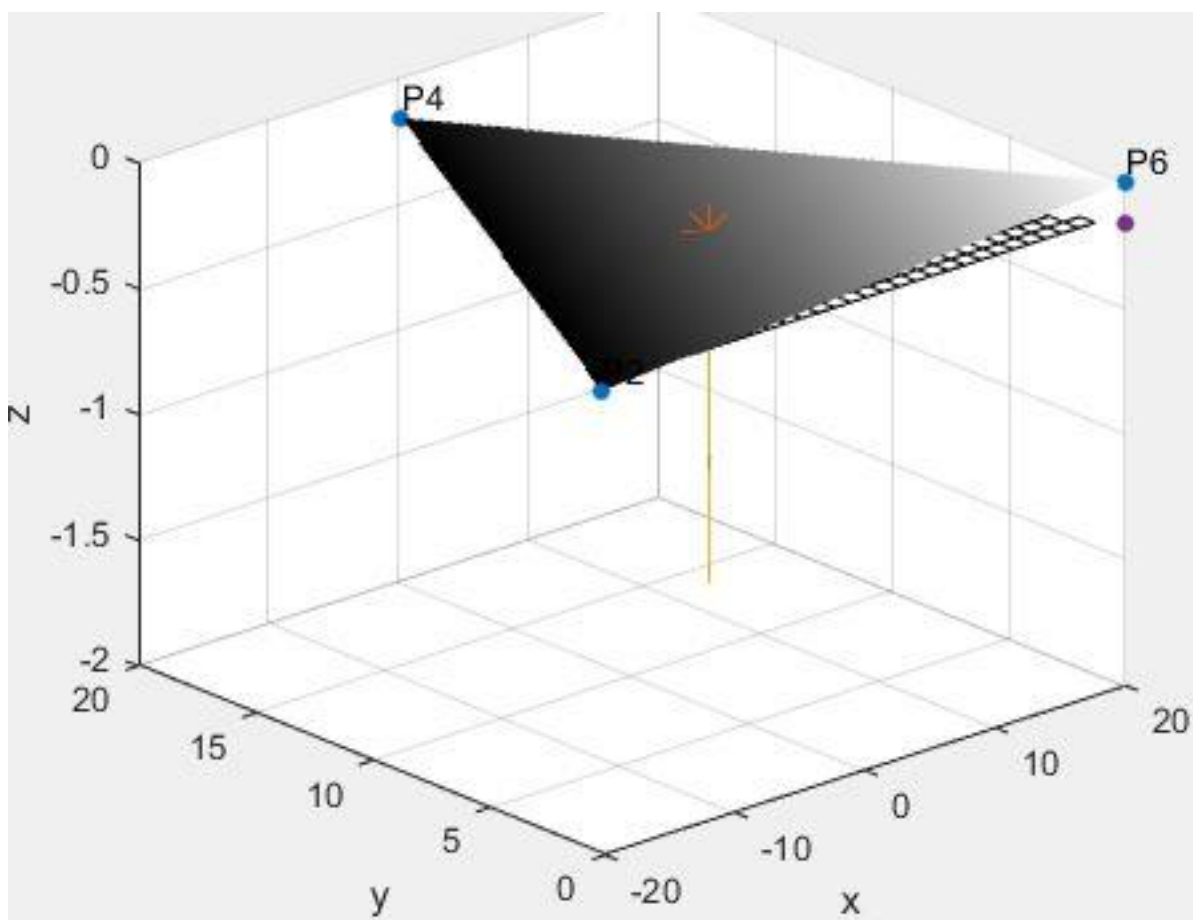


*Figure 3.30: The Z-frame plane including P2, P4 and P6 coordinate systems is parallel to the MR- image plane. The Z-frame is rotated +10 degrees around both the x and y-axes based on its first orientation in the Figure 3.29.*

Moreover, the rotation direction of the marker around the x and y-axes has to be estimated to find a correct rotation of the robotic device. Therefore, the Z-axis indication triangle feature, discussed in the section 3.1, is used to determine the correct rotation direction of the marker in the image coordinate system.

The rotation direction around the y-axis is estimated using the z-axis values of the centroids P2 and P6. If P2 has a higher z value than P6 and the triangle is in the left side of the marker (in the cross-section view), it shows that the rotation must be executed in the positive direction, and if P6 has a higher Z value, the rotation must be executed in the negative rotation. In the case that triangle is in the right side of the marker, the z axis has to be inverted. In addition, the rotation around the x-axis is indicated using the z-coordinates of the P4 and one of the P2 or P4 centroids.

### 3.3 Graphical user interface implementation

The automatic alignment detection algorithm of the Z-frame which utilizes the procedures in the section 3.2 has been implemented in a Graphical User Interface (GUI) which is designed in Matlab R2017a. The proposed GUI displays only the required information which enables the user to easily interact with the several processing stages (Figure 3.32).

The flowchart of the proposed algorithm for the alignment detection and the angle calculation of the Z-frame in the GUI is represented in the Figure 3.31.

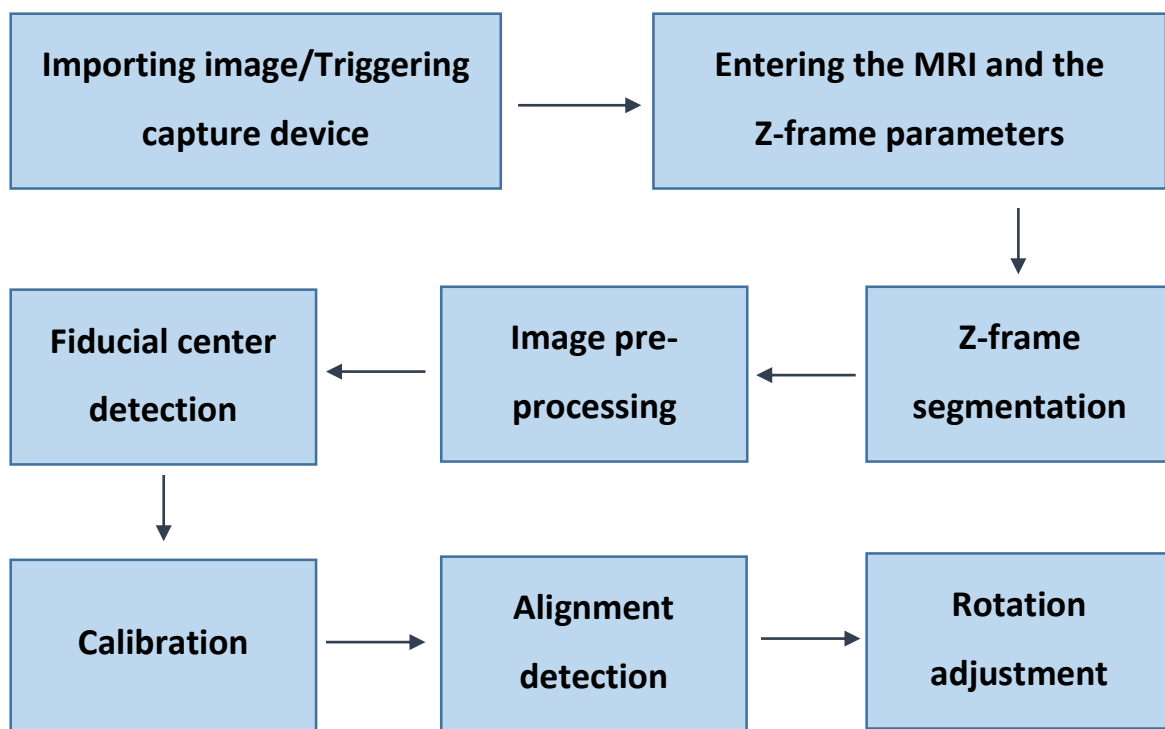


*Figure 3.31: The processing flowchart of the implemented algorithm in GUI. Once the the image is imported to the workstation by the user, several parameters from the Z-frame and the MR-sequences must be entered. Therefore, the image is processed in the five-stages which the marker alignment is calculated. At the last step the required rotation angles of the marker are calculated and displayed on the screen.*



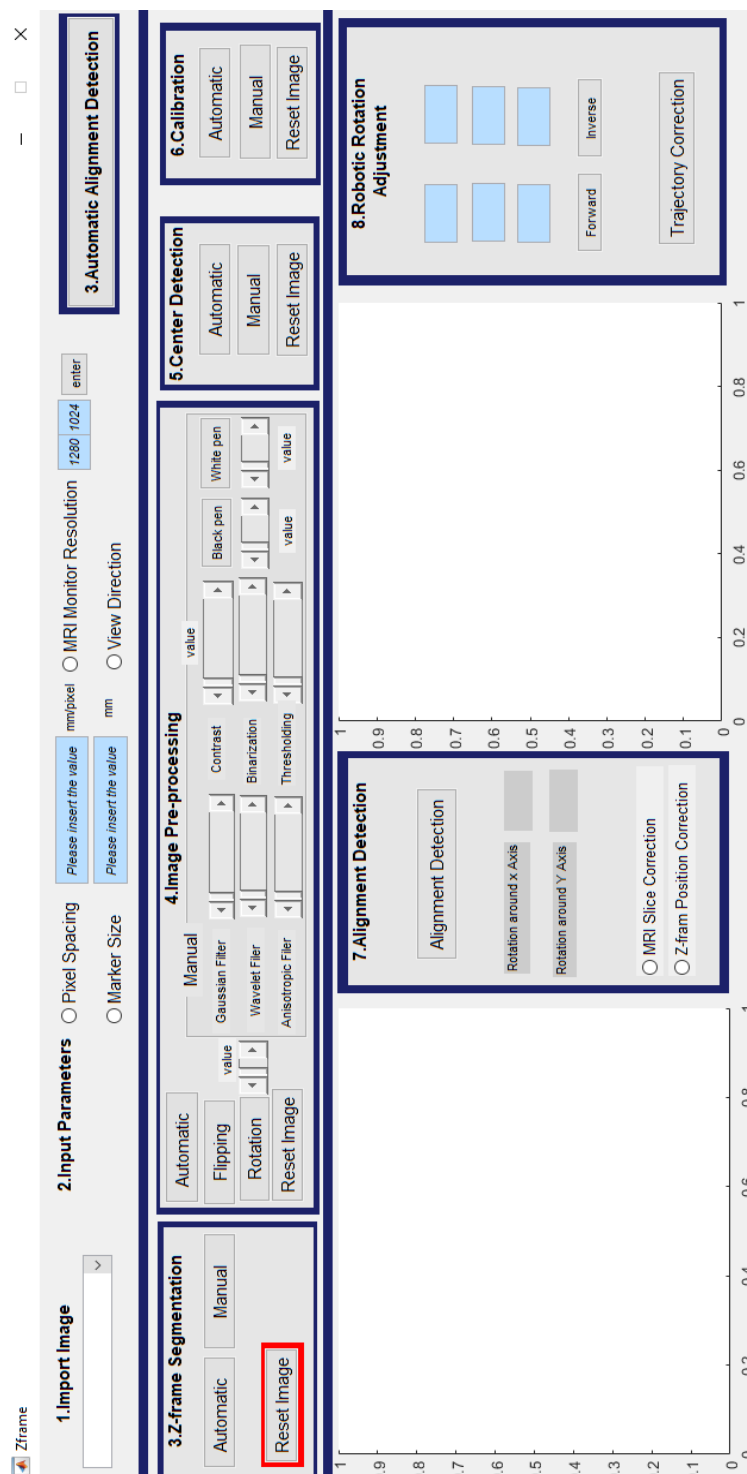


Figure 3.32: A view of the GUI for the alignment detection procedure. The first two steps include importing the image to the workspace and entering the required parameters for the processing steps. The segmentation, pre-processing, center detection and the calibration steps includes both automatic and manual options that user can select one of them for the processing of the image.

- *Import image* panel: It includes a popupmenu button for either selecting the path of the saved image or triggering a capture device or a camera for acquiring an image from the MRI monitor in a near real-time workflow. Figure 3.33 represents this button.

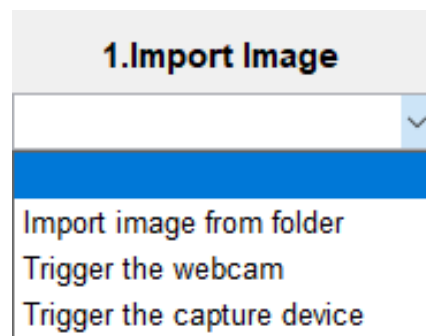


Figure 3.33: The popupmenu for importing the image to the workstation.

- *Input parameters* panel: In this step, the user has to enter several parameters of the imaging and physical setup properties. It includes pixel spacing from the MRI header, Z-frame marker size, MRI monitor resolution, and direction view of the marker. all this information is used further in the calibration stage. Figure 3.34 shows this panel.

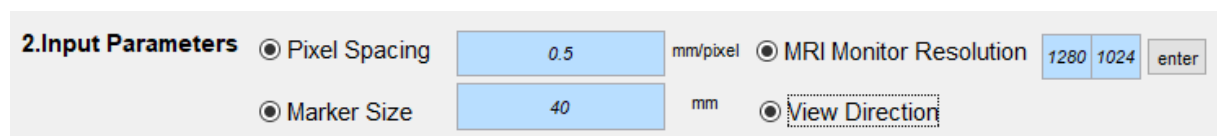
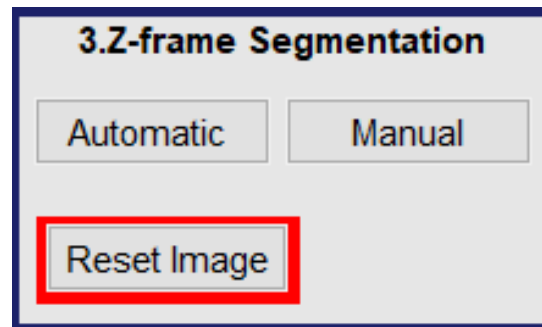


Figure 3.34: The panel of the input parameters.

- *Z-frame segmentation* panel: In the segmentation step, the user has two options to extract the Z-frame marker from the captured MRI image (Figure 3.35). The manual button implements the cropping method and the automatic one applies the neural network process discussed in the section 3.2.



*Figure 3.35: The Z-frame segmentation button panel. The Reset Image button enables resetting of the image after an undesired segmentation in order to repeat the segmentation process.*

- *Image pre-processing panel:* In the automatic part of the image pre-processing stage, the Anisotropic filter, contrast enhancement and binarization and masking methods with an average threshold are implemented. The manual part of this stage comprises several noise removal techniques (Gaussian filter, Wavelet filter, and Anisotropic filter), contrast enhancement, binarization and thresholding methods, which threshold of each of these steps can be controlled using the sliders. Moreover, there are two buttons as black and white pens in the manual section which the thickness of the tip of the pen can be controlled using a slider (Figure 3.37). The black pen can be used for removing the objects that do not belong to the 7 fiducial markers such as center pointing triangles, and the z-axis indication triangle. The white pen can be applied for adding pixels to the fiducials which are distorted by noise or artifacts in MRI. This process improves the accuracy of the center detection stage which depends on the volume of the pixels in each fiducial marker. The rotation button is implemented for manual rotation of the Z-frame within the image, which the rotation degree is selected using the slider. Furthermore, the flipping button is applied with the purpose of correcting the view of the marker. For example, if the triangle structure is in the right side of the marker, it must be transferred to the left side of the marker by flipping the image along the y-axis (Figure 3.37). This panel is shown in the Figure 3.36.

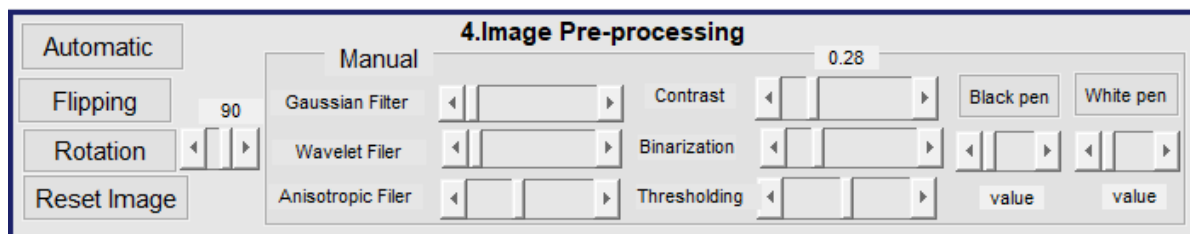


Figure 3.36: The image Pre-processing panel. It includes all the automatic and manual procedures for the processing of the imported image. A Reset Image button is applied to reset image after each undesired-procedure.

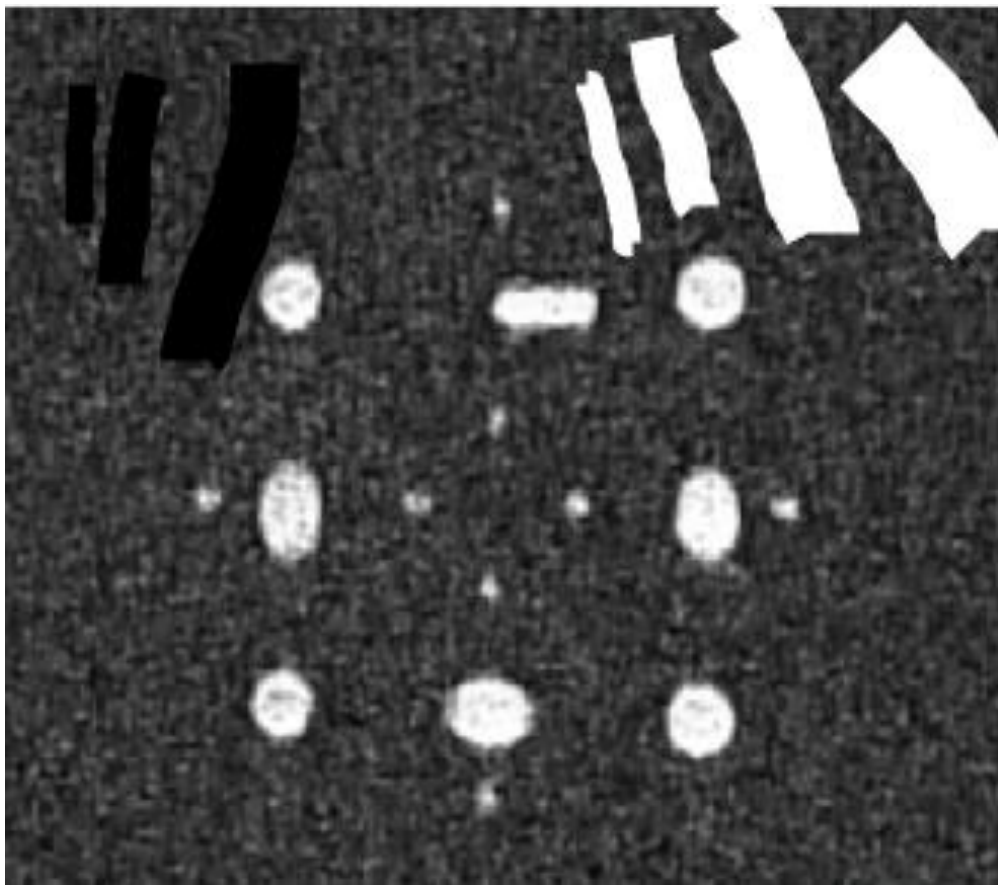
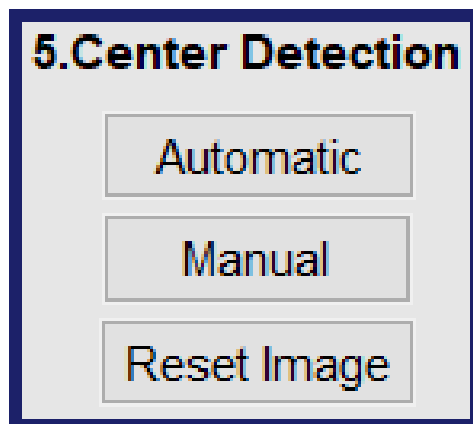


Figure 3.37: Visuallization of the the thickness of the black and white pens on a captured-MR image from the Z-frame. This image requires flipping along the y-axis to transfer the triangle structure to the left side of the marker, which correct the view of the marker. The pens enable painting on the image with different thickness to add or remove the pixels to the fiducials.

- *Center detection* panel: In this step, the center detection function (section 3.2), is applied to the binarized-image from the previous step. In the automatic part, the center of each volume is detected, and if there are more than 7 detected centroids, an error is displayed on the screen that the user has to repeat the image pre-processing stage. In the manual part, the user has to analyze each detected centroid to make sure that the centroid is located exactly in the center of each fiducial markers. Therefore, the user can drag and drop the detected centroids to the right position. The center detection panel is represented in the Figure 3.38 (a).
- *Calibration* panel: It implements the procedure explained in the section 3.2. The manual button enables the user to select the center of the marker for the transformation process (Figure 3.38 (b)).



(a)



(b)

Figure 3.38: (a) Center Detection panel. (b) Calibration panel. The Reset Image buttons are applied to reset image after each undesired-procedure.

- *Alignment detection* panel: in this step, alignment of the Z-frame is calculated based on the mathematical formulation in the section 3.2, and the required rotation around x- and y-axes are displayed on the screen. Therefore, user has two possibilities to make the Z-

frame parallel to the image plane for the alignment correction of the marker: MRI slice correction; or the Z-frame position correction using a mechanical or robotic device (Figure 3.39).

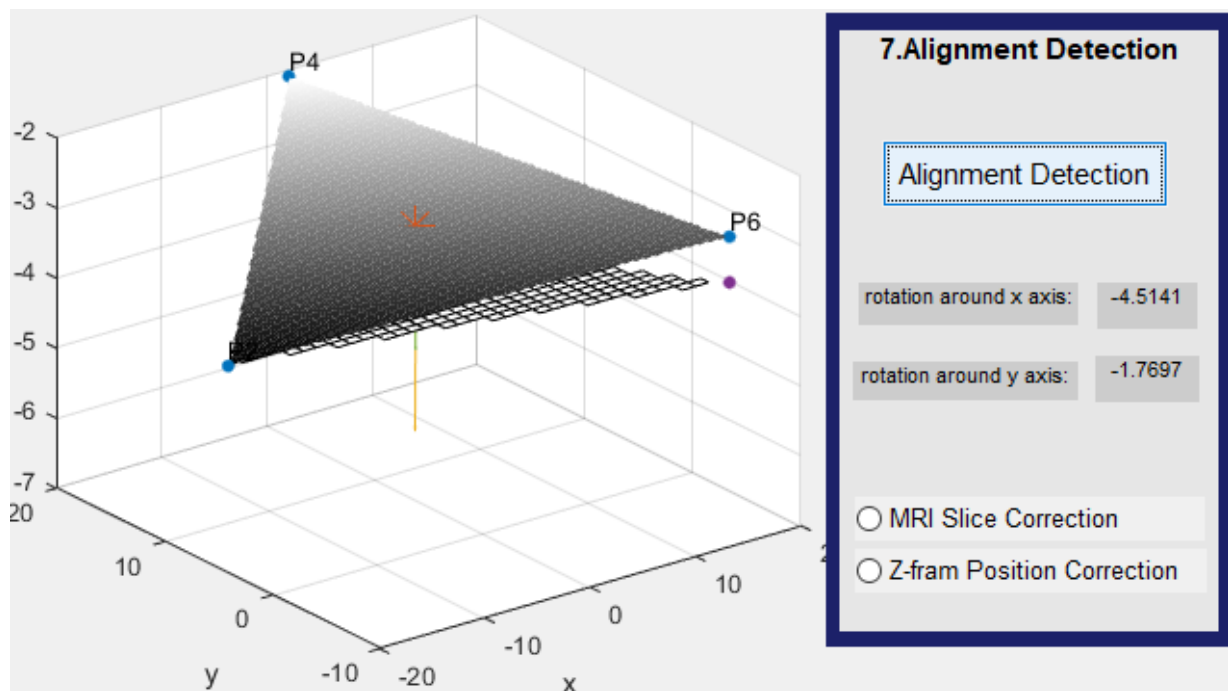


*Figure 3.39: The Alignment Detection panel. This diagram shows that the marker must be rotated +4.51 degrees around the x-axis, and positive +1.77 degrees around the y-axis. Therefore these values will be transferred to the positioning device.*

- *Robotic rotation adjustment panel:* In this stage, the computed rotation angles from the last step is transformed to the required rotation of the robotic or mechanical device to align the Z-frame according to the image plane. For the demonstration of implementing the angles to the robotic controllers, the skara robot function [48] is implemented to the GUI (Figure 3.40).

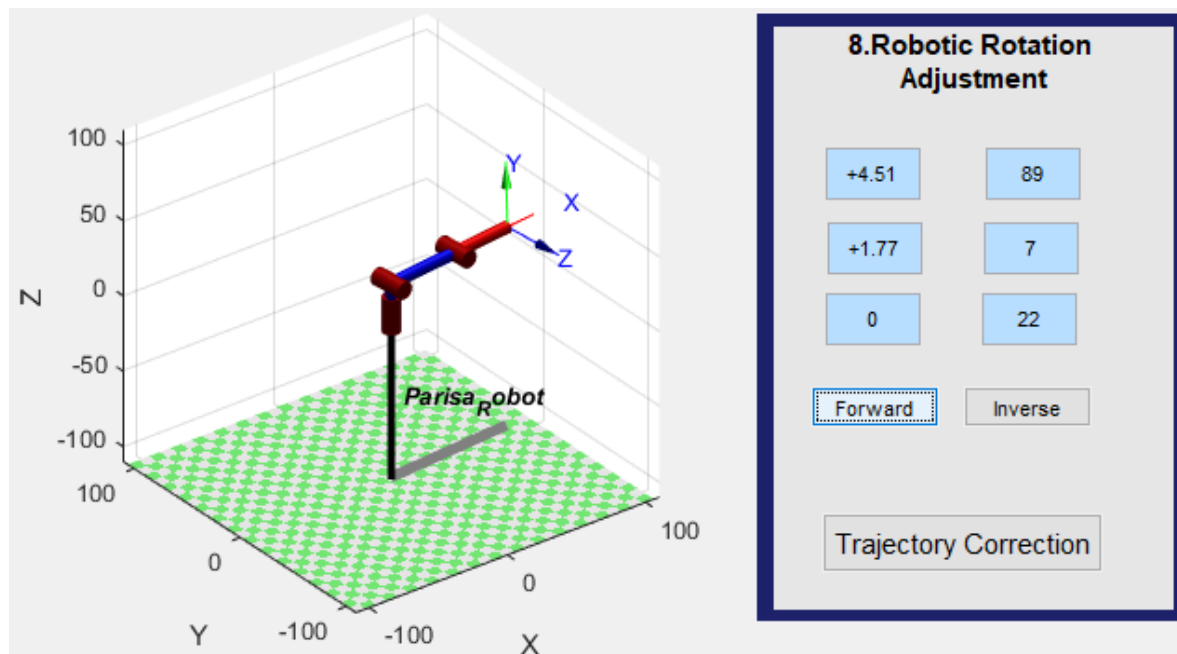


Figure 3.40: The Robotic Rotation Adjustment panel. In the case that the Z-frame Position Correction is selected in the last step, the computed angles will be transferred to the Robotic Rotation Adjustment panel for calculating the required rotation and translation of the robotic device.

## 4 Testing and result

### 4.1 Z-frame marker positioning using an MR-compatible rotary frame

In order to determine the accuracy of the proposed registration method, the Z-frame marker is manually rotated within the scanner around the two axes (x- and y-axes) by 3 degrees' increments.

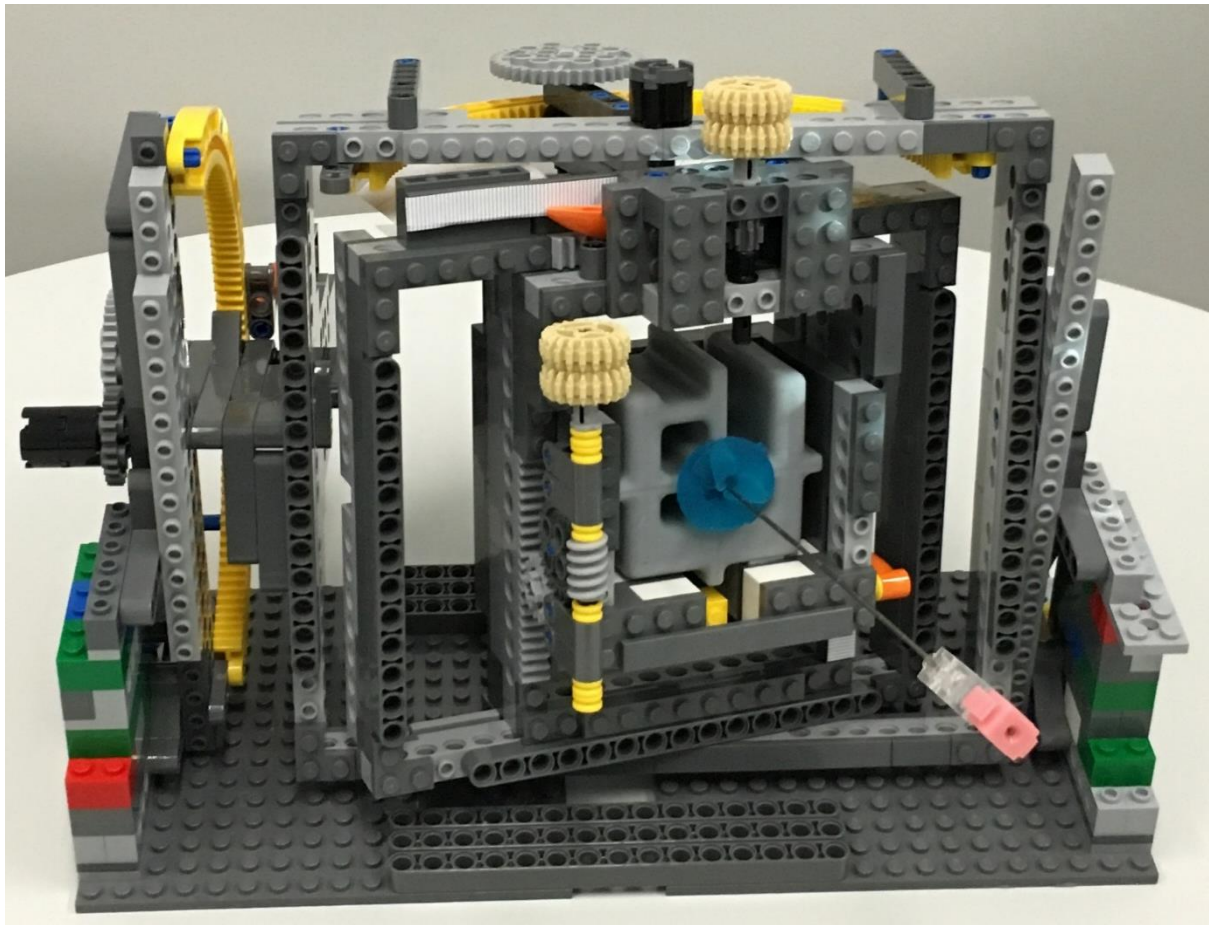
For the rotation of the marker inside the MRI, an MR-compatible rotary positioning frame is built (using Lego), which is shown in Figure 4.1. The rotary frame has four degrees of freedom which provides the rotation and translation of the marker around (and along) both the x- and y-axes. Therefore, the marker is fixed in the center of the rotary frame, and the relative orientations of marker to the image plane are calculated by acquiring a single slice MR-image of that.

The protocol of the testing includes four steps: the calibration of the rotary frame inside the MRI, rotation of the marker around the x-axis, rotation of the marker around the y-axis, and the rotation of the marker around both the x- and y-axes.

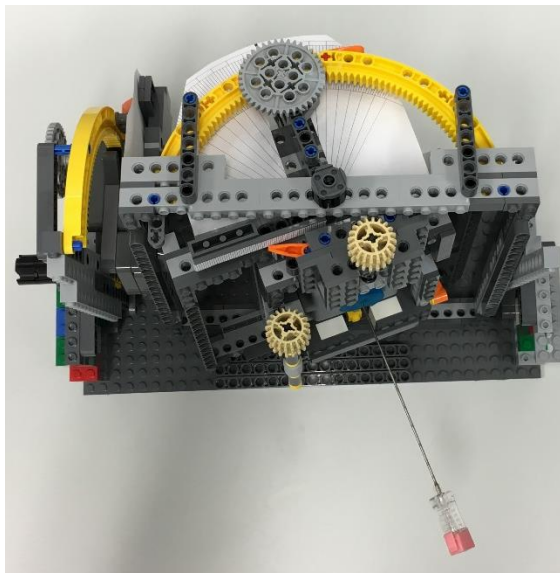
#### 4.1.1 Rotary frame calibration inside the MRI space

For the calibration of the frame inside the MRI, a 2D MR-image (spin echo) is acquired from the Z-frame marker using a head coil (SIEMENS head neck 20) in a 3T Skyra MRI system (Siemens Healthineers, Germany) (Figure 4.2). Therefore, the rotation of the Z-frame around the x- and y-axes are calculated using the implemented graphical user interface (section 3.3). The calculated orientation of the marker in this step, is considered as the starting point, such that all subsequent rotations are estimated with respect to this image.

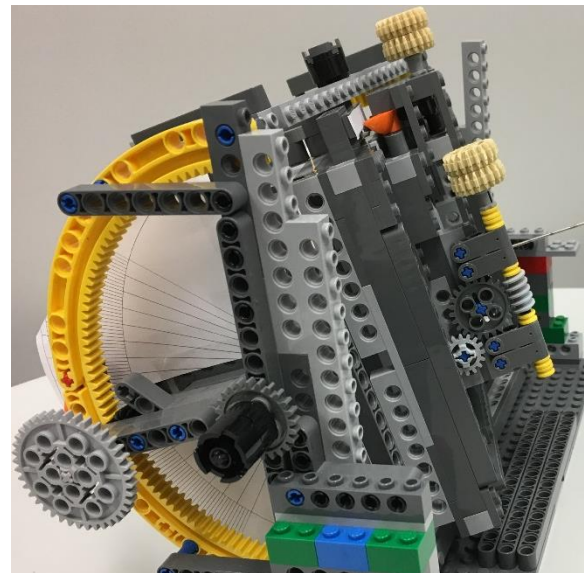




(a)



(b)



(c)

Figure 4.1: The MR-compatible rotary frame. (a) The Z-frame marker is attached to the center of the frame. An MR-compatible needle is placed in the center of the marker using a needle holder. (b),(c) The top and backside views of the frame. The scales allow rotating of the frame with the desired angles around both the x- and y-axes.

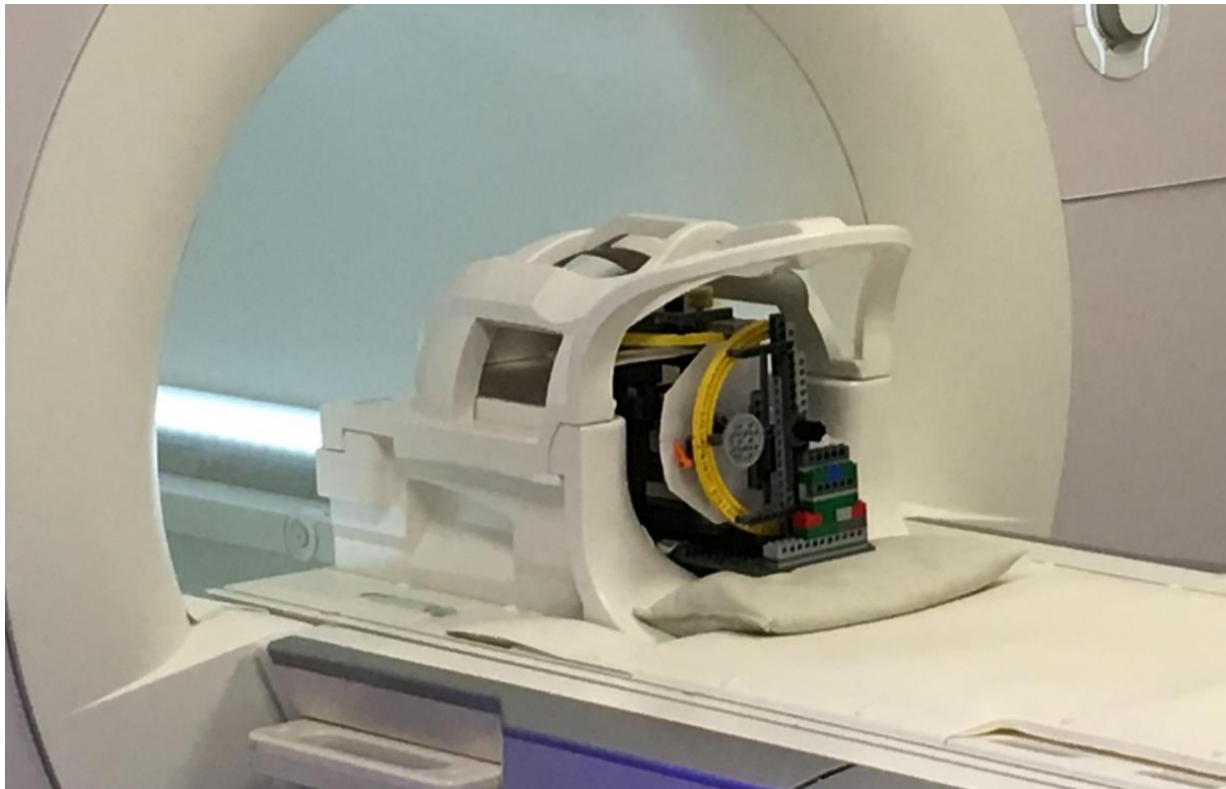


*Figure 4.2: The rotary frame is fixed on the patient table, and is placed inside a transmit–receive head coil of a 3T Skyra MRI system (Siemens Healthineers, Germany).*

#### 4.1.2 Rotation of the Z-frame around the x-axis

For the assessment of the accuracy of the algorithm for calculating the rotation of the marker around the x-axis, the rotary frame is rotated manually by 3 degrees' increments around the x-axis, while the rotation around the y-axis is constant. For each image, the known angle of the physical rotation and the computed angle (using the GUI) is compared.

However, the movements of the positioning frame during imaging, as well as the imaging artifacts and the quality of the image acquisition setup (section 3.2) affect the accuracy of the alignment detection algorithm negatively. Accordingly, the Gold-standard-CAD analysis is performed which permits the estimation of the error in the implemented algorithm. In this experiment, the CAD model of the Z-frame is rotated around its axes with the same rotation values in the MRI experiment. The cross-section images of the marker are transferred to the GUI for the marker alignment calculation. Therefore, a linear regression line is fitted to the

set of the data from MRI and CAD-model experiments, which model the dependency between the nominal values and the estimated values. Figure 4.3 shows the data and the regression lines for the both experiments.

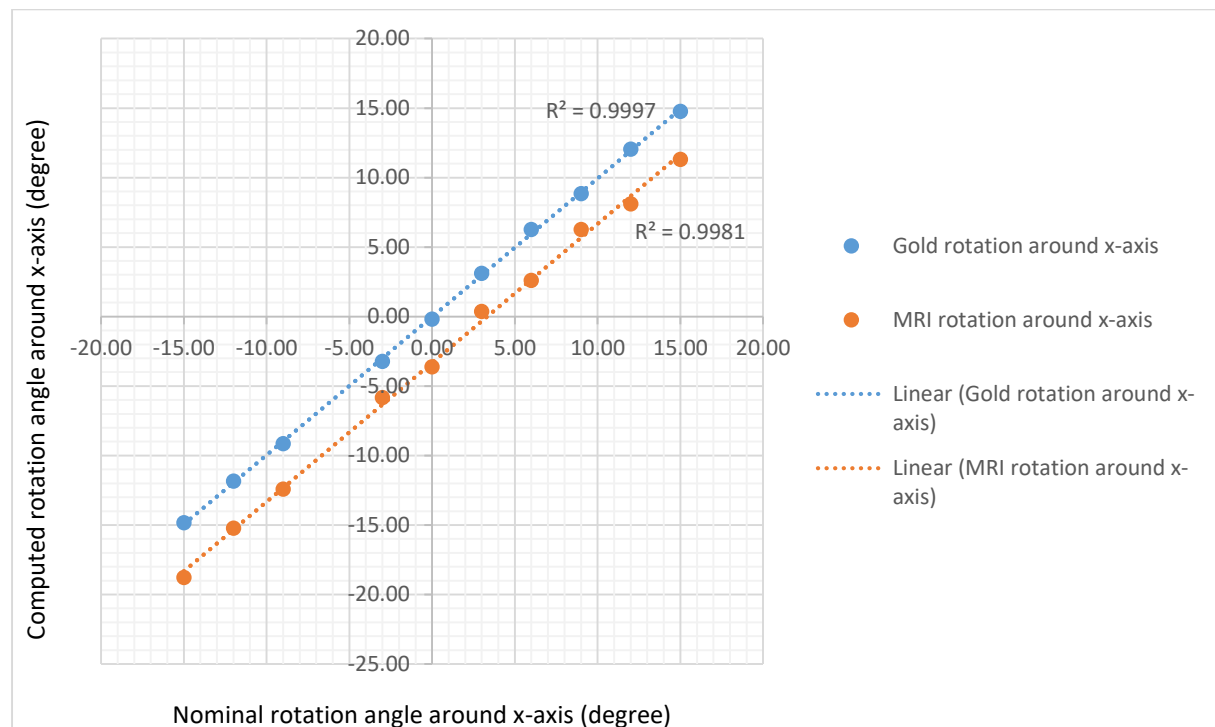


*Figure 4.3: The regression models of the computed rotation angles around the x-axis in the MR and the Gold-standard CAD images. The R-squared values indicate that the data points are close to the the fitted regression line.*

R-squared is a statistical value that estimates how the data are close to the regression line. It is always between 0 and 1. Generally, the higher R-squared determines that the regression model fits the data better and the response data are close to their mean [55].

### 4.1.3 Rotation of the Z- frame around the y-axis

The performance of the algorithm for computing the rotation angle around the y-axis is estimated using the same protocol in the last experiment while the rotation around the x-axis is constant. The Figure 4.4 represents the results of this experiment.

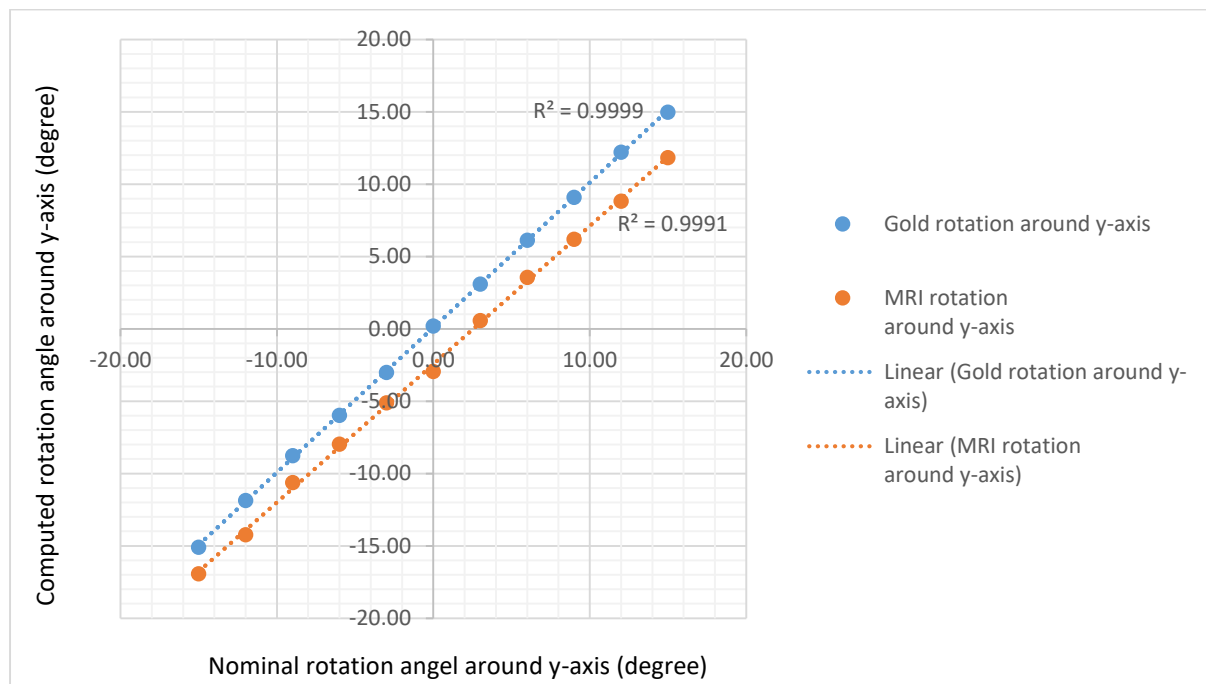


*Figure 4.4: The regression models of the computed rotation angles around the y-axis in the MR and the Gold-standard CAD images. The R-squared values indicate that the data points are close to the the fitted regression line.*

In the last two experiments, the mean value of the computed rotation points from the constant axis determines the rotation offset of the frame in the MRI space. In these tests, the mean value of the computed rotation around the y-axis (computed from the results in the first experiment where the y-axis is constant), is equal to -2.51 degrees, and the mean value around the x-axis (computed from the results in the second experiment where the x-axis is constant), is equal to -3.1 degrees. By applying these mean values, the rotary frame can be registered in the MRI coordinate system accurately.

#### 4.1.4 Rotation of the Z-frame around both the x-and y-axes

In this experiment, the accuracy of the algorithm for calculating of the rotation around both the x- and y-axes, is estimated by turning the rotary frame around both the x- and y-axes simultaneously. For the objective to evaluate the ability of the algorithm for calculating the rotation angles in different conditions, two rotation scenarios are considered:

- **Rotation around both the x- and y-axes with the same orientation**

In this test, the frame is rotated inside the MRI scanner, around both the x- and y-axes with the same 3 degrees' increments and the rotation direction. The computed angles are compared with the computed angles from the CAD standard images. Figure 4.5 represent the fitted regression lines for the computed angles around the x- and y-axes, respectively.

- **Rotation around both the x- and y-axes with the opposite orientation**

In this scenario, the frame is rotated around both the x- and y-axes with the same 3 degrees' increments but the opposite rotation direction within the MRI scanner. Therefore, the computed angles are compared with the computed angles from the CAD standards images. Figure 4.6 represent the fitted regression lines for the computed angles around the x- and y-axes, respectively.

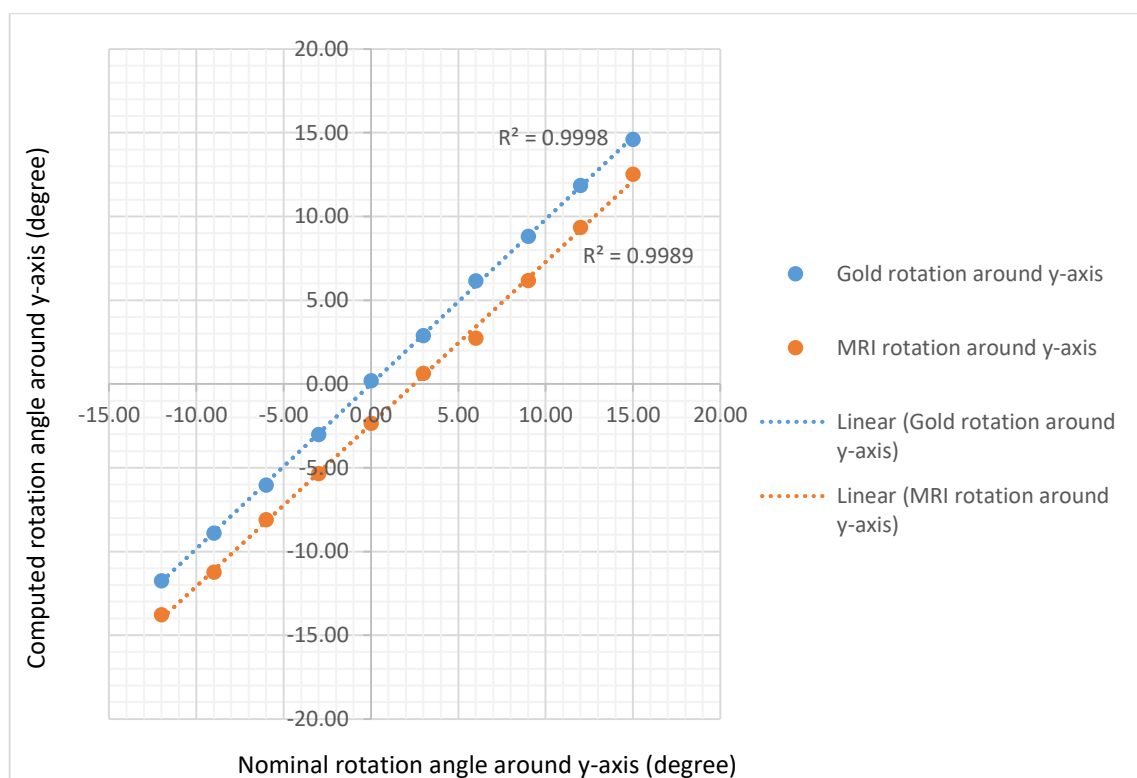
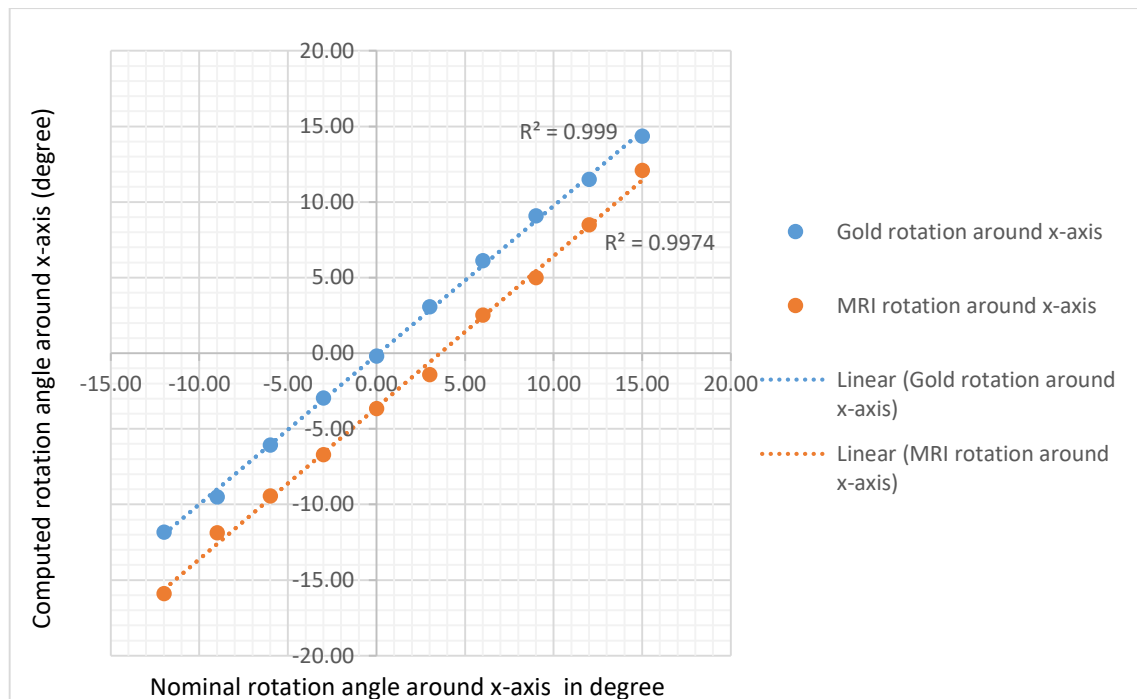


Figure 4.5: The regression models of the computed rotation around the x- and y-axes, when the frame is rotated around both the x- and y-axes with the same angle value and direction in the MR- and the Gold-standard CAD images. The R-squared values indicate that the data points are close to the the fitted regression line.

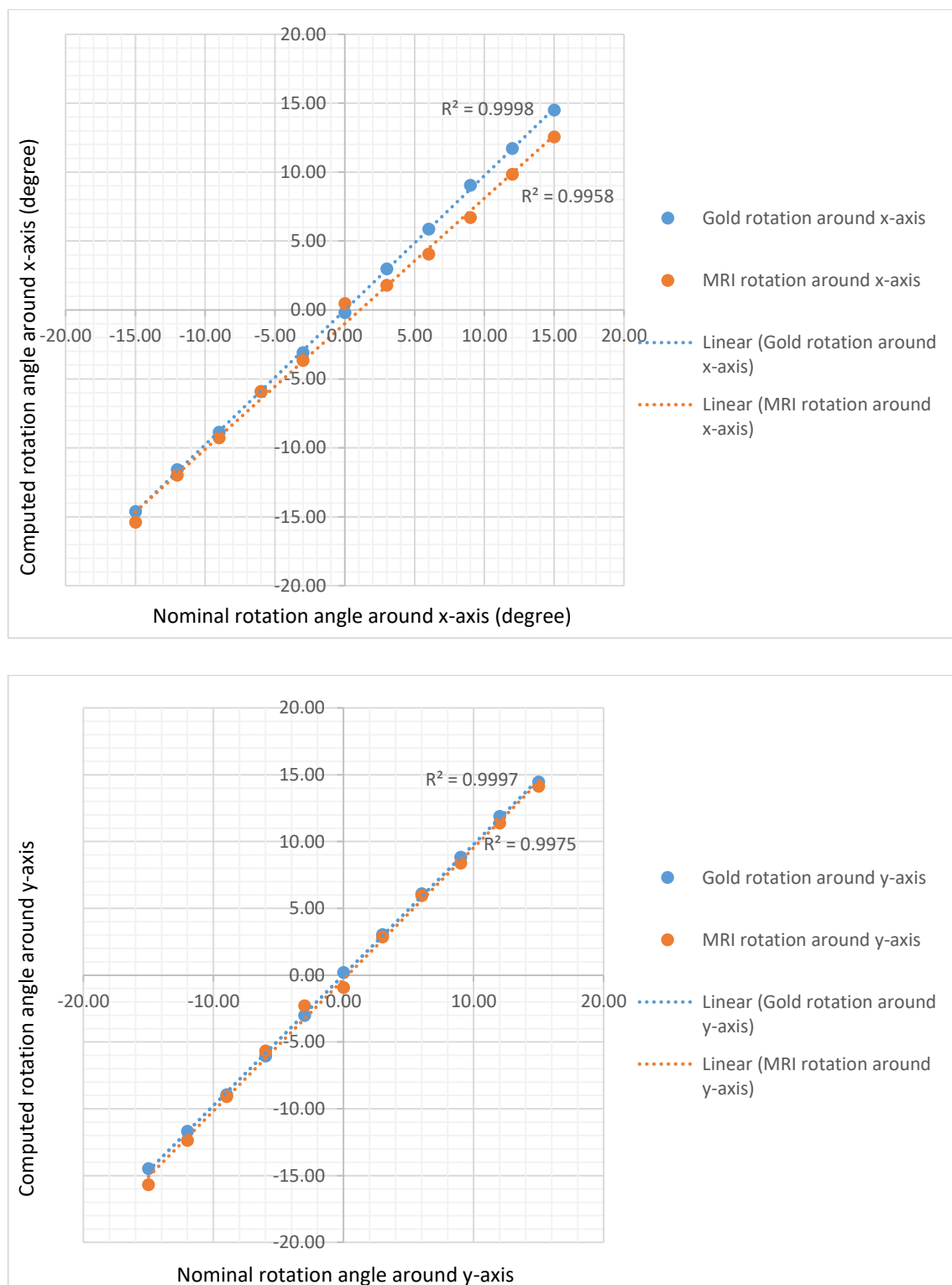


Figure 4.6: The regression models of the computed rotation around the x- and y-axes when the frame is rotated around both the x- and y-axes with the same angle value and opposite direction in the MR- and the Gold-standard CAD images. The R-squared values lines indicate that the data points are close to the fitted regression line.

Furthermore, the Root Mean Square Error (RMSE) of the computed rotation angles from the MR- and the Gold-standard-CAD images are estimated according to the equation 4.1 [56]. The RMSE determines how the data points (computed angles) far from the regression line are, which indicates the concentration of the data around the regression lines.

$$RMSE = \sqrt{(f - o)^2} \quad (4.1)$$

Where,  $f$  is the nominal rotation angles, and  $o$  is the computed angles using the software [56]. Table 4.1 shows the calculated RMSE for all the experiments.

| Rotation of the Z-frame around (degree) | RMSE for the gold standard rotation around the x-axis | RMSE for the gold standard rotation around the y-axis | RMSE for the MRI rotation around the x-axis | RMSE for the MRI rotation around y-axis |
|---|---|---|---|---|
| X-axis                                  | 0.18  | -   | 0.49  | -                                       |
| Y-axis                                  | -   | 0.13  | -   | 0.51                                    |
| X- and Y-axes (same direction)          | 0.32  | 0.66  | 0.18  | 0.38                                    |
| X- and Y-axes (opposite direction)      | 0.26  | 0.21  | 1.0   | 0.47                                    |
| Average RMSE                            | <b>0.25</b>   | <b>0.33</b>   | <b>0.56</b>                                 | <b>0.45</b>                             |
| Total RMSE                              | <b>0.29</b>   |   | <b>0.50</b>                                 |   |

*Table 4.1: The calculated RMSE values for each experiment.*



The average RMSE from the rotations in the Gold-standard-CAD images is considered as the registration error which emanates from the accuracy of the proposed algorithm (section 3.2). Moreover, the error of the registration system (including the resolution of the capture device, the MR-imaging artifacts, the Z-frame printing artifacts; such as air bubbles, and the positioning frame) is calculated by subtraction the average RMSE of the calculated rotation of the MR-images from the RMSE of the CAD-images. In conclusion, the error of the alignment detection algorithm is equal to 0.25 degrees for the rotation around the x-axis, and 0.33 degrees for the rotation around the y-axis. The error of the registration approach without considering the error of the algorithm is equal to 0.31 degrees for the rotation around the x-axis, and 0.12 degrees around the y-axis.

It can be concluded that the total registration error of the algorithm is 0.29 degrees in the Gold-standard-CAD test, and 0.50 degrees in the MRI test.

## 4.2 Phantom-targeting test

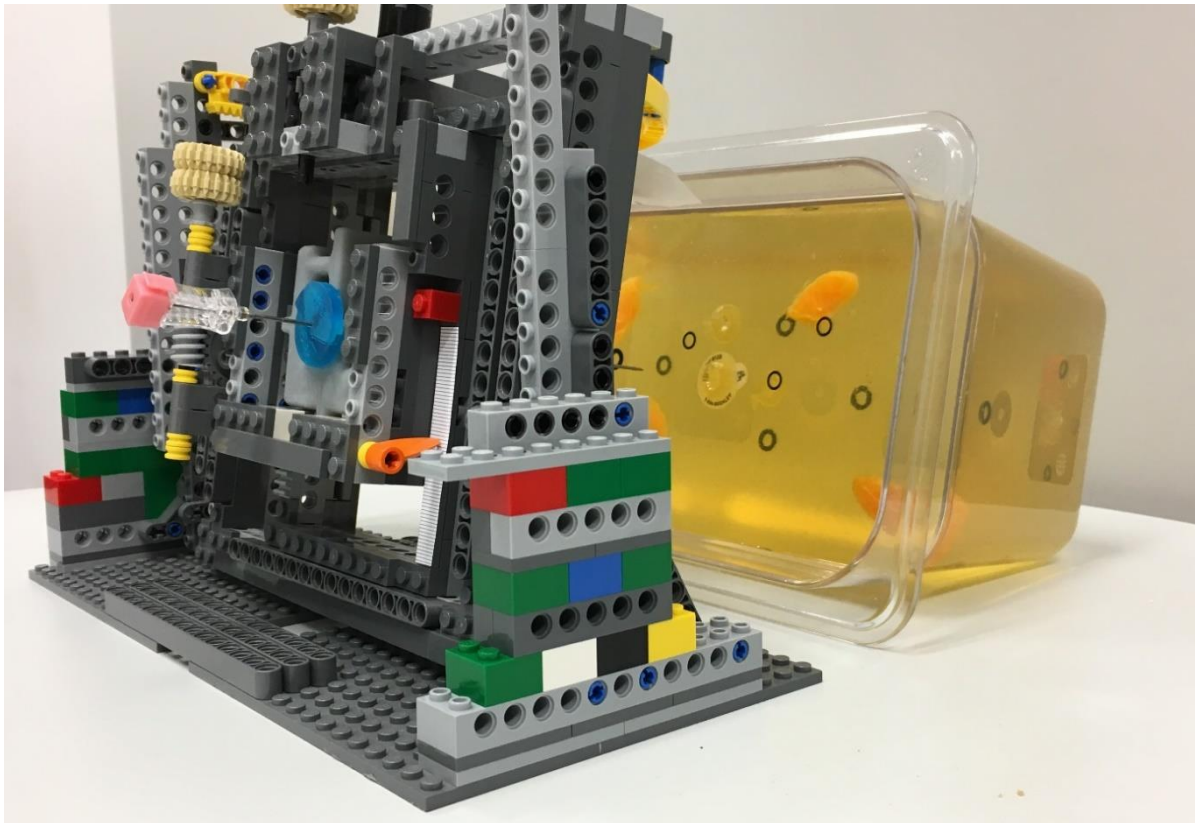
To evaluate the ability of the proposed registration method for the alignment of a needle to the identified target, a phantom study is conducted. The phantom is prepared with the mixture of the gelatin powder (gelatine, 240 Bloom, Carl Roth GmbH) and water, which two Beekley markers (PinPoint) are located approximately at 10 and 4.5 cm from the box opening as the target and the insertion points. The custom-made gelatin phantom is placed in front of the positioning frame (with the attached Z-frame marker) on the MRI table. A body coil (Siemens Healthcare, Germany) is used to cover both the phantom and the positioning frame. Figure 4.7 (a) and (b) show the setup of the phantom-targeting test.

The MR-image is obtained from the marker and the phantom using the Spin Echo imaging sequence (TR/TE: 600ms/11 ms; acquisition matrix: 512\*384; flip angle: 130; field of view: 200 x 200 mm; slice thickness: 3 mm; number of averages: 2; TA: 25.98).

From the coronal image, a trajectory for the needle pathway relative to the target position is identified. Therefore, the axial image of the Z-frame is transferred to the navigation

workstation (using the imaging setup explained in the section 3.2), and the rotation angles of the marker relative to the MRI plane is determined (Figure 4.8 (a)) . Accordingly, the marker is rotated manually using the rotary frame according to the computed angles around both the x- and y-axes to make it parallel to the MR-plane. Then, the second image is obtained to confirm the parallelization of the marker to the image plane. The confirmation image shows that the rotation angles around both the axes are close to zero (Figure 4.8 (b)). Therefore, from the coronal images, the distance between the trajectory line (center of the marker) and a fiducial marker is compared against their physical distance, to calculate the required translational movement of the marker (Figure 4.9 (a)). According to this calculation, the marker is moved +4 mm along the x-axis.

Subsequently, an 18-gauge-MRI-safe biopsy needle (KIM-18/15, length: 150 mm, INNOVATIVE TOMOGRAPHY PRODUCTS GMBH, Bochum, Germany) is inserted into the phantom through the needle holder which is located in the center of the marker. After insertion of the needle, the third image is obtained to localize the needle within the phantom. Figure 4.9 (b) shows that the needle successfully reached the target with 1mm offset.



(a)



(b)

Figure 4.7: The setup of the phantom targeting test in a 3T Skyra MRI system (Siemens Healthineers, Germany). The rotary frame and the phantom are positioned on the patient table, and a body coil covers them.

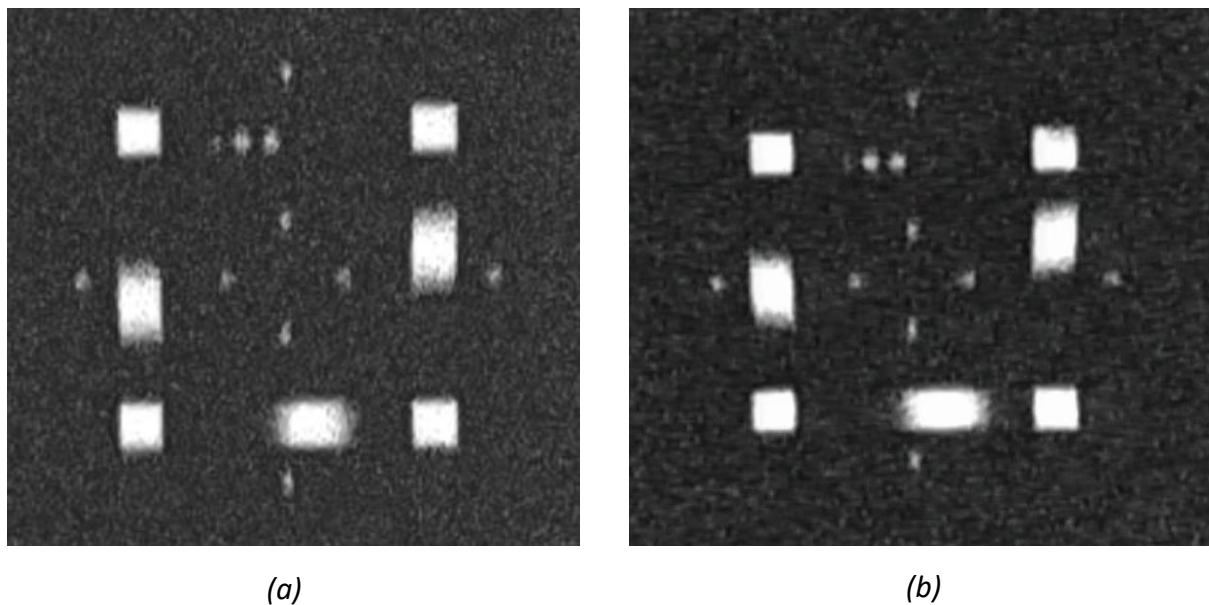


Figure 4.8: 2-D image of the Z-frame marker. (a) This image is applied to calculate the required rotation of the marker around both the x- and y-axes. According to this image, the marker has to rotate  $+6.04$  degrees around the x-axis and  $+3.8$  degrees around the y-axis to be parallel to the MR-plane. (b) The confirmation image after the rotation shows the angle between the marker and the image plane:  $-0.52$  degrees around x-axis, and  $-0.62$  degrees around the y-axis, which are the offset of the rotary frame.

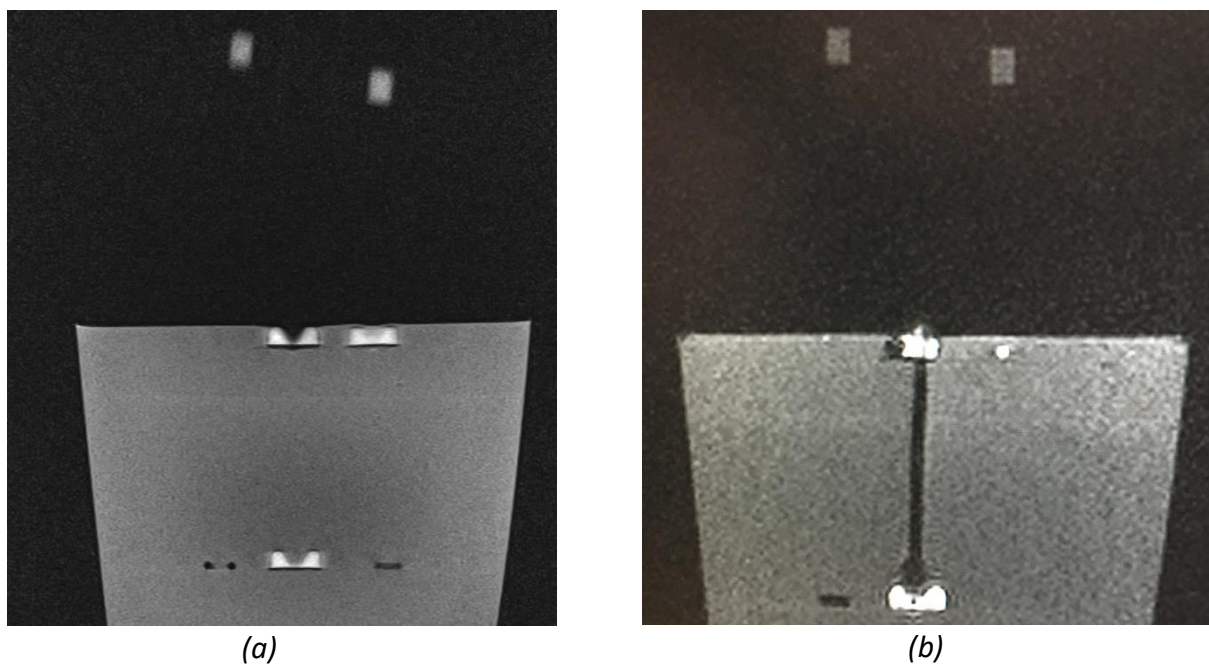


Figure 4.9: The coronal view of the phantom and the Z-frame. (a) This image is used to calculate the required translational movements of the marker. (b) This image shows the needle pathway through the target after inserting the needle.

## 5 Conclusion and outlook

In this thesis a new instrument and robotic device registration and tracking method using an additively manufactured Z-frame marker is developed for the faster handling of the interventional procedures in MRI.

A comprehensive analysis of the material selection for manufacturing of the Z-frame marker was conducted. T1 and T2 relaxation time for different resin materials using MRI spectroscopy were estimated (section 3.1.2). The new features for the Z-frame marker were designed to improve the accuracy and the speed of the alignment procedure (section 3.1.1). Moreover, the new image acquisition setup was introduced which enabled a nearly real-time registration approach (section 3.2.1).

An automated and standalone application, which interacts with the user (section 3.3), for an accurate detection, tracking and registration was accomplished. The designed algorithm takes into account the limitations which might be encountered during the image processing (such as imaging artifacts) for the calculation of the instrument alignment according to the identified-target position. In order to find the appropriate methods in each stage of the processing, an investigation on the common filtering methods was conducted. For example, Gaussian filter was compared with Wavelet-based denoising and anisotropic filtering, and the last one was selected for denoising of the captured MR-images due to its efficiency in suppressing the noise and preserving the features of interest. Subsequently, the centers of each fiducial was calculated based on the connected components in the image.

For the automatic segmentation of the Z-frame structures in the images, a Faster-RCNN algorithm was tested, considering that the Z-frame might have a different scale, rotation and position in the images. In order to estimate the image rotation, the automated feature matching technique using SIFT and SURF feature extraction methods, and a mathematical technique based on the fiducials coordinate system were tested, while the latter method was implemented, as it was the most accurate one in the determination of the rotation angle from the distorted images by noise. The approach also takes into consideration the change of the

inner fiducial shapes in different slices. A series of mathematical formulations were applied to calculate the alignment of the marker in MRI coordinate system and estimate the required rotation angle of the Z-frame to align the interventional tools inside the desired trajectory. It includes the rotation angle and direction of the Z-frame around both the x- and y-axes.

For the assessment of the accuracy of the registration method, an MR-compatible rotary frame was designed, which was able to rotate the marker around two axes during the inside MRI-tunnel experiments. Therefore, the detection alignment algorithm and the registration method were tested in several different experiments, and the results were applied for the calculation of the error.

However, for the improvement of this approach in the future, several aspects shall be considered:

- Automatic computation of the translational alignment of the Z-frame marker regarding to the target position. The translation of the marker can be calculated based on the MR-image which visualize the target and at least two of the seven fiducials. Therefore, a translation vector can be calculated by applying the estimated coordinates of the fiducials from the alignment matrix in section 3.2.
- Improvement in the automatic segmentation of the Z-frame form the full screen images using a machine learning technique.
- For the image acquisition setup (section 3.2.1), a new capture device with a higher quality has to be implemented, in order to improve the resolution of the captured-MR images.
- A study has to be conducted on the localization accuracy of the fiducial markers when the Z-frame is placed far from the iso-center of the magnet.
- An analysis on the accuracy of the algorithm has to be conducted which takes into account the tissue motion during the registration procedure which leads to the displacement of the identified target.

The result from the phantom-targeting test indicates that the proposed registration method is a reliable and an accurate method to align the needle to an MR-identified target successfully, with registration error equals to 1.5 mm and the processing time between 15 to

20 seconds. Moreover, this technique removes the need for an additional interface for connecting the MRI scanner and the navigation software with each other. This method does not require a direct line-of-sight clearance, so that the presence of the clinician inside the MRI-tunnel will not affect the registration accuracy. Therefore, this technique can contribute to a faster and more precise guiding of the MRI-based interventions.

## 6 Appendix

All the codes and the functions of the implemented automated alignment detection application are enclosed in a DVD. In this chapter only the most important functions are presented.

### Anisotropic Diffusion filtering:

```
%      niter - number of iterations.
%      kappa - conduction coefficient.
%      lambda - max value of .2 for stability
%      option - 1 Perona Malik diffusion equation No 1
%              2 Perona Malik diffusion equation No 2

niter=3;
kappa=80
lambda=0.20
option=2

diff = y;
diff= im2bw(diff,0.5);
diff=double(diff);
[rows,cols] = size(diff);
for i = 1: niter;

% Construct diff1 which is the same as diff but has an extra padding of zeros around it.

diff1 = zeros (rows+2, cols+2);
diff1 (2: rows+1, 2: cols+1) = diff;

% North, South, East and West differences

deltaN = diff1(1: rows,2:cols+1) - diff;
deltaS = diff1(3: rows+2,2:cols+1) - diff;
deltaE = diff1(2: rows+1,3:cols+2) - diff;
deltaW = diff1(2: rows+1,1:cols) - diff;

% Conduction

if option == 1
    cN = exp(-(deltaN/kappa). ^2);
    cS = exp(-(deltaS/kappa). ^2);
    cE = exp(-(deltaE/kappa). ^2);
    cW = exp(-(deltaW/kappa). ^2);
elseif option == 2
    cN = 1./(1 + (deltaN/kappa).^2);
    cS = 1./(1 + (deltaS/kappa).^2);
    cE = 1./(1 + (deltaE/kappa).^2);
    cW = 1./(1 + (deltaW/kappa).^2);
end

diff = diff + lambda*(cN.*deltaN + cS.*deltaS + cE.*deltaE + cW.*deltaW);

subplot(ceil(sqrt(niter), ceil(sqrt(niter))), i)
imagesc(diff), colormap(gray), axis image
end
```



## Centroids detection and ordering them along the U-shape of the marker

```

s = regionprops(Image, 'Centroid');
centroids = cat(1, s. Centroid);
centroids = round(centroids);
figure
imshow(Image)
hold on
plot(centroids(:,1),centroids(:,2), 'b*');

[m n]=size(centroids)
if m~=7
    n=0
end

%% ordering the 7 points
% calculating the euclidean distance

for i=1:7
    for j=1:7
        d=centroids(i,:)-centroids(j,:)
        c(i,j)=norm(d)
    end
end
n=max(c)
[row,col]=find(c==max(c))

% Finding the points with the maximum distance

m=sort(n, 'descend') % sorted from max to min
m= unique(m) % removal of duplicate value
m=sort(m, 'descend') % sorted from max to min

[H1,O1] = find(c==m(1))
[H2,O2] = find(c==m(2))
H=[H1(1);H1(2);H2(1);H2(2)]
H=sort(H, 'ascend')

U1=centroids(H(1),:)
U3=centroids(H(2),:)
U5=centroids(H(3),:)
U7=centroids(H(4),:)

if abs(U5(1)-U7(1))<7 & U5(2)>U7(2)
    U7=centroids(H(3),:)
    U5=centroids(H(4),:)
end
if abs(U1(1)-U3(1))<6 & U1(2)>U3(2)
    U3=centroids(H(1),:)
    U1=centroids(H(2),:)
end

u=[U1;U3;U5;U7]

% determination if U1 has two neighbors, then two shapes for the z-frame are possible

i=1
y=[0 0;0 0]
while y(1,:)==0 & i<7

if centroids(i,1)>U1(1,1) & centroids(i,1)<U5(1,1) & centroids(i,2)>=U1(1,2) &
centroids(i,2)<=U5(1,2)
    y(1,:)=centroids(i,:)
elseif centroids(i,1)>U1(1,1) & centroids(i,1)<U5(1,1) & centroids(i,2)>=U5(1,2) &
centroids(i,2)<=U1(1,2)
    y(1,:)=centroids(i,:)
elseif centroids(i,1)<U1(1,1) & centroids(i,1)>U5(1,1) & centroids(i,2)>=U1(1,2) &
centroids(i,2)<=U5(1,2)
    y(1,:)=centroids(i,:)
elseif centroids(i,1)<U1(1,1) & centroids(i,1)>U5(1,1) & centroids(i,2)>=U5(1,2) &
centroids(i,2)<=U1(1,2)

```

```

        y(1,:)=centroids(i,:)
    else
        y(1,:)=[0 0]
    end
    i=i+1
end

i=1

while y(2,:)==0 & i<7

    if centroids(i,1)>=U1(1,1) & centroids(i,1)<=U3(1,1) & centroids(i,2)>U1(1,2) &
    centroids(i,2)<U3(1,2)
        y(2,:)=centroids(i,:)
    elseif centroids(i,1)>=U1(1,1) && centroids(i,1)<=U3(1,1) & centroids(i,2)>U3(1,2) &
    centroids(i,2)<U1(1,2)
        y(2,:)=centroids(i,:)
    elseif centroids(i,1)<=U1(1,1) & centroids(i,1)>=U3(1,1) & centroids(i,2)>U1(1,2) &
    centroids(i,2)<U3(1,2)
        y(2,:)=centroids(i,:)
    elseif centroids(i,1)<=U1(1,1) & centroids(i,1)>=U3(1,1) & centroids(i,2)>U3(1,2) &
    centroids(i,2)<U1(1,2)
        y(2,:)=centroids(i,:)
    else
        y(2,:)=[0 0]
    end
    i=i+1
end

if (y(1,:)~=0 & y(2,:)~=0)
    t=1
else
    t=0
end

% find the rotation direction (clockwise or not)

d35=U3-U5;
normd35=norm(d35);
if normd35(2)<0

    % U3 is down and U5 is up

    downpoint=U3;
    if t==1
        innerpoint=centroids(find(centroids(:,1)>=U3(1) & centroids(:,1)<=U7(1) &
        centroids(:,2)>U3(2) & centroids(:,2)<U7(2)))
        if isempty(innerpoint)
            innerpoint=centroids(find(centroids(:,1)<=U3(1) & centroids(:,1)>=U7(1) &
            centroids(:,2)>U3(2) & centroids(:,2)<U7(2)))
        end
        elseif t==0
            innerpoint=centroids(find(centroids(:,1)>U1(1) & centroids(:,1)<U3(1) &
            centroids(:,2)>=U3(2) & centroids(:,2)<=U1(2)))
            if isempty(innerpoint)
                innerpoint=centroids(find(centroids(:,1)>U1(1) & centroids(:,1)<U3(1) &
                centroids(:,2)<=U3(2) & centroids(:,2)>=U1(2)))
            end
        end
    end
else

    % U5 is down

    downpoint=U5;
    if t==1

        innerpoint=centroids(centroids(:,1)>=U5(1) & centroids(:,1)<=U7(1) &
        centroids(:,2)>U5(2) & centroids(:,2)<U7(2))
        if isempty(innerpoint)
            innerpoint=centroids(find(centroids(:,1)<=U5(1) & centroids(:,1)>=U7(1) &
            centroids(:,2)>U5(2) & centroids(:,2)<U7(2)))
        end
        elseif t==0

```

```

        innerpoint=centroids(find(centroids(:,1)>U1(1) & centroids(:,1)<U5(1) &
centroids(:,2)>U5(2) & centroids(:,2)<U1(2)))
        if isempty(innerpoint)
            innerpoint=centroids(find(centroids(:,1)>U1(1) & centroids(:,1)<U5(1) &
centroids(:,2)<=U5(2) & centroids(:,2)>=U1(2)))
        end
    end
end

%% angle calculation

j=2.9
center=U1
U7_orientated=U7

% It calculates the angle between the lines U1 and the diagonal of the square (the line
between U1 and U7.

if t==1
    theta=abs(atan((downpoint(1)-U1(1))/(downpoint(2)-U1(2))))
    if innerpoint~=0
        theta=theta+1.5708
    end
end

if t== 0
    theta=abs(atan((downpoint(1)-U1(1))/(downpoint(2)-U1(2))))
    if innerpoint~=0
        theta=theta+3.14159
    end
    if isempty(innerpoint)
        theta=theta+4.71239
    end
end

% Calculation of the rotation matrix

orientated_centroids=centroids-center
R = [cos(theta) -sin(theta); sin(theta) cos(theta)];
orientated_centroids =orientated_centroids* R % apply the rotation about the origin
orientated_centroids=orientated_centroids+center

labels = {'P1','P2','P3','P4','P5','P6','P7'};
plot(orientated_centroids(:,1),orientated_centroids(:,2), 'b*')
axis([-100 80 100 350])

text(orientated_centroids(:,1),orientated_centroids(:,2),labels,'VerticalAlignment','bottom','Hori
zontalAlignment','left')

%% Alignment matrix calculation

P(1:7,1:2) = 0;
centsort = sortrows(orientated_centroids) %Sort by the first row (x-position)
P(1:3,1:2) = sortrows(centsort(1:3,1:2),2); %First three points are most left
P(4,1:2) = centsort(4,1:2); %Fourth point is in the middle (along the x-axis)
P(5:7,1:2) = flipud(sortrows(centsort(5:7,1:2),2)); %First three points are most right

f(1:6)=0;
for i=[2,4,6]
    f_i= norm(P(i+1,:)-P(i,:))/ norm(P(i+1,:)-P(i-1,:))
    f(i)=f_i;
end

% estimation of The three corresponding points in the frame coordinate system

lx=40;
ly=40;
lz=40;
a=lx * [-1/2 1/2-f(4) 1/2];
b=ly * [1/2-f(2) 1/2 -1/2+f(6)];
c=lz * [-1/2+f(2) -1/2+f(4) -1/2+f(6)];
pf=[a;b;c];

```

## 7 References

- [1] J. Cepek *et al.*, “A system for MRI-guided transperineal delivery of needles to the prostate for focal therapy,” (eng), *Medical physics*, vol. 40, no. 1, p. 12304, 2013.
- [2] H. Su, G. Li, D. C. Rucker, R. J. Webster Iii, and G. S. Fischer, “A Concentric Tube Continuum Robot with Piezoelectric Actuation for MRI-Guided Closed-Loop Targeting,” (eng), *Annals of biomedical engineering*, vol. 44, no. 10, pp. 2863–2873, 2016.
- [3] J. Cepek, B. A. Chronik, and A. Fenster, “The effects of magnetic field distortion on the accuracy of passive device localization frames in MR imaging,” (eng), *Medical physics*, vol. 41, no. 5, p. 52301, 2014.
- [4] J. Cepek, B. A. Chronik, and A. Fenster, “Errors in Device Localization in MRI Using Z-Frames,” in *Lecture Notes in Computer Science, Medical Image Computing and Computer-Assisted Intervention – MICCAI 2013*, D. Hutchison *et al.*, Eds., Berlin, Heidelberg: Springer Berlin Heidelberg, 2013, pp. 348–355.
- [5] M. Bock *et al.*, “Active catheter tracking using parallel MRI and real-time image reconstruction,” (eng), *Magnetic resonance in medicine*, vol. 55, no. 6, pp. 1454–1459, 2006.
- [6] M. Bock *et al.*, “Active catheter tracking using parallel MRI and real-time image reconstruction,” (eng), *Magnetic resonance in medicine*, vol. 55, no. 6, pp. 1454–1459, 2006.
- [7] S.-E. Song *et al.*, “Development and preliminary evaluation of a motorized needle guide template for MRI-guided targeted prostate biopsy,” (eng), *IEEE transactions on bio-medical engineering*, vol. 60, no. 11, pp. 3019–3027, 2013.
- [8] J. M. Fitzpatrick, “Fiducial registration error and target registration error are uncorrelated,” in Lake Buena Vista, FL, 2009, p. 726102.
- [9] Dale, Brian M and Brown, Mark A and Semelka, Richard C, *MRI: basic principles and applications*: John Wiley & Sons, 2015.

- [10] S. Aja-Fernández, A. Tristán-Vega, and C. Alberola-López, "Noise estimation in single- and multiple-coil magnetic resonance data based on statistical models," (eng), *Magnetic resonance imaging*, vol. 27, no. 10, pp. 1397–1409, 2009.
- [11] S. D and D. D, "Wavelet Based Image Denoising Technique," *IJACSA*, vol. 2, no. 3, 2011.
- [12] M. E. Soto, J. E. Pezoa, and S. N. Torres, "Thermal Noise Estimation and Removal in MRI: A Noise Cancellation Approach," in *Lecture Notes in Computer Science, Progress in Pattern Recognition, Image Analysis, Computer Vision, and Applications*, C. San Martin and S.-W. Kim, Eds., Berlin, Heidelberg: Springer Berlin Heidelberg, 2011, pp. 47–54.
- [13] H. a. o. Sheshadri, "Denoising of Rician noise in Magnitude MRI Images using wavelet shrinkage and fusion method," 2016.
- [14] J. Tokuda *et al.*, "In-bore setup and software for 3T MRI-guided transperineal prostate biopsy," (eng), *Physics in medicine and biology*, vol. 57, no. 18, pp. 5823–5840, 2012.
- [15] S.P. DiMaio, E. Samset, G. Fischer, I. Iordachita, G. Fichtinger, F. Jolesz, and C.M. Tempany, "LNCS 4792 - Dynamic MRI Scan Plane Control for Passive Tracking of Instruments and Devices,"
- [16] Samuel Patz, Samuel Zhong, and Ronald Sahatjian, "A Novel Approach to MRI Visibility of Catheters in Real-Time Studies,"
- [17] F. Fischbach *et al.*, "MR-guided freehand biopsy of breast lesions in a 1.0-T open MR imager with a near-real-time interactive platform: Preliminary experience," (eng), *Radiology*, vol. 265, no. 2, pp. 359–370, 2012.
- [18] M. Fatahi, L. R. Demenescu, and O. Speck, "Subjective perception of safety in healthy individuals working with 7 T MRI scanners: A retrospective multicenter survey," (eng), *Magma (New York, N.Y.)*, vol. 29, no. 3, pp. 379–387, 2016.
- [19] F. Fischbach *et al.*, "MR-guided freehand biopsy of liver lesions with fast continuous imaging using a 1.0-T open MRI scanner: Experience in 50 patients," (eng), *Cardiovascular and interventional radiology*, vol. 34, no. 1, pp. 188–192, 2011.
- [20] A. Krieger *et al.*, "An MRI-compatible robotic system with hybrid tracking for MRI-guided prostate intervention," (eng), *IEEE transactions on bio-medical engineering*, vol. 58, no. 11, pp. 3049–3060, 2011.
- [21] *Robotics: Science and Systems X*: Robotics: Science and Systems Foundation, 2014.

- [22] S. P. DiMaio *et al.*, “Robot-assisted needle placement in open MRI: System architecture, integration and validation,” (eng), *Computer aided surgery : official journal of the International Society for Computer Aided Surgery*, vol. 12, no. 1, pp. 15–24, 2007.
- [23] M. Rea *et al.*, “Sub-pixel localisation of passive micro-coil fiducial markers in interventional MRI,” (eng), *Magma (New York, N.Y.)*, vol. 22, no. 2, pp. 71–76, 2009.
- [24] Dumoulin, Charles L and Souza, SP and Darrow, RD, “Real-time position monitoring of invasive devices using magnetic resonance,” vol. 29, 411–415, 1993.
- [25] H. Busse, R. Trampel, W. Gründer, M. Moche, and T. Kahn, “Method for automatic localization of MR-visible markers using morphological image processing and conventional pulse sequences: Feasibility for image-guided procedures,” (eng), *Journal of magnetic resonance imaging : JMRI*, vol. 26, no. 4, pp. 1087–1096, 2007.
- [26] M. Kaiser *et al.*, “Resonant marker design and fabrication techniques for device visualization during interventional magnetic resonance imaging,” (eng), *Biomedizinische Technik. Biomedical engineering*, vol. 60, no. 2, pp. 89–103, 2015.
- [27] A. D. Squires, Y. Gao, S. F. Taylor, M. Kent, and Z. T. H. Tse, “A Simple and Inexpensive Stereotactic Guidance Frame for MRI-Guided Brain Biopsy in Canines,” (eng), *Journal of medical engineering*, vol. 2014, p. 139535, 2014.
- [28] Tokuda, Junichi and Song, Sang-Eun and Tuncali, Kemal and Tempany, Clare and Hata, Nobuhiko, “Configurable Automatic Detection and Registration of Fiducial Frames for Device-to-Image Registration in MRI-guided Prostate Interventions,” 355–362, 2013.
- [29] O. Unal, J. Li, W. Cheng, H. Yu, and C. M. Strother, “MR-visible coatings for endovascular device visualization,” (eng), *Journal of magnetic resonance imaging : JMRI*, vol. 23, no. 5, pp. 763–769, 2006.
- [30] Robert Odenbach, “3D-printed Z-frame marker for MRI-guided interventions,” 2017.
- [31] F. Bloch, “Nuclear Induction,” vol. 70, pp. 7–8, 1946.
- [32] P. S. Tofts, *Methods for quantitative relaxation parameter mapping: measuring T1 and T2*, 2009.
- [33] C. M. J. de Bazelaire, G. D. Duhamel, N. M. Rofsky, and D. C. Alsop, “MR imaging relaxation times of abdominal and pelvic tissues measured in vivo at 3.0 T: preliminary results,” (eng), *Radiology*, vol. 230, no. 3, pp. 652–659, 2004.

- [34] P. Ding, Y. Zhang, W.-J. Deng, P. Jia, and A. Kuijper, "A light and faster regional convolutional neural network for object detection in optical remote sensing images," *ISPRS Journal of Photogrammetry and Remote Sensing*, vol. 141, pp. 208–218, 2018.
- [35] R. Girshick, J. Donahue, T. Darrell, and J. Malik, "Rich feature hierarchies for accurate object detection and semantic segmentation," [Online] Available: <http://arxiv.org/pdf/1311.2524v5>.
- [36] D. Scherer, A. Müller, and S. Behnke, "Evaluation of Pooling Operations in Convolutional Architectures for Object Recognition," in *Lecture Notes in Computer Science, Artificial Neural Networks – ICANN 2010*, D. Hutchison et al., Eds., Berlin, Heidelberg: Springer Berlin Heidelberg, 2010, pp. 92–101.
- [37] S. Ren, K. He, R. Girshick, and J. Sun, "Faster R-CNN: Towards Real-Time Object Detection with Region Proposal Networks," [Online] Available: <http://arxiv.org/pdf/1506.01497v3>.
- [38] B. Adam, F.H.K. Zaman, I. M. Yassin, H. Z. Abidin, and Z. I. Rizman, "Performance evaluation of faster R-CNN on GPU for object detection," *J. Fundam and Appl Sci.*, vol. 9, no. 3S, p. 909, 2018.
- [39] S. Aja-Fernandez, C. Alberola-Lopez, and C.-F. Westin, "Noise and signal estimation in magnitude MRI and Rician distributed images: A LMMSE approach," (eng), *IEEE transactions on image processing : a publication of the IEEE Signal Processing Society*, vol. 17, no. 8, pp. 1383–1398, 2008.
- [40] E. Elboher and M. Werman, "Efficient and accurate Gaussian image filtering using running sums," in *2012 12th International Conference on Intelligent Systems Design and Applications (ISDA)*, Kochi, India, Nov. 2012 - Nov. 2012, pp. 897–902.
- [41] R. D. Nowak, "Wavelet-based Rician noise removal for magnetic resonance imaging," (eng), *IEEE transactions on image processing : a publication of the IEEE Signal Processing Society*, vol. 8, no. 10, pp. 1408–1419, 1999.
- [42] F. Xiao and Y. Zhang, "A Comparative Study on Thresholding Methods in Wavelet-based Image Denoising," *Procedia Engineering*, vol. 15, pp. 3998–4003, 2011.
- [43] A. Pizurica, W. Philips, I. Lemahieu, and M. Acheroy, "A versatile wavelet domain noise filtration technique for medical imaging," (eng), *IEEE transactions on medical imaging*, vol. 22, no. 3, pp. 323–331, 2003.

- [44] D. L. Donoho, "De-noising by soft-thresholding," *IEEE Trans. Inform. Theory*, vol. 41, no. 3, pp. 613–627, 1995.
- [45] Keeling, Stephen L and Stollberger, Rudolf, "Nonlinear anisotropic diffusion filtering for multiscale edge enhancement," vol. 18, 2002.
- [46] P. Perona and J. Malik, "Scale-space and edge detection using anisotropic diffusion," *IEEE Trans. Pattern Anal. Machine Intell.*, vol. 12, no. 7, pp. 629–639, 1990.
- [47] Keeling, Stephen L and Stollberger, Rudolf, "Nonlinear anisotropic diffusion filtering for multiscale edge enhancement," vol. 18, 2002.
- [48] [Online] Available: <https://de.mathworks.com>. Accessed on: May 18 2018.
- [49] L. O’Gorman, "Binarization and multithresholding of document images using connectivity," vol. 56, 1994.
- [50] N. Garg, "Binarization Techniques used for Grey Scale Images," vol. 71, 2013.
- [51] N. B. A. Mustafa *et al.*, "Image processing of an agriculture produce: Determination of size and ripeness of a banana," in *2008 International Symposium on Information Technology*, Kuala Lumpur, 2008, pp. 1–7.
- [52] D. G. Lowe, "Distinctive Image Features from Scale-Invariant Keypoints," *International Journal of Computer Vision*, vol. 60, no. 2, pp. 91–110, 2004.
- [53] Meierhold, N and Spehr, M and Schilling, A and Gumhold, S and Maas, HG, "Automatic feature matching between digital images and 2D representations of a 3D laser scanner point cloud," vol. 38, 446--451, 2010.
- [54] C.-C. Hsiung, "Theory of intersection of two plane curves," *Bull. Amer. Math. Soc.*, vol. 49, no. 10, pp. 786–793, 1943.
- [55] [Online] Available: <http://blog.minitab.com>. Accessed on: Sep. 27 2018.
- [56] [Online] Available: <http://www.statisticshowto.com/rmse/>.